STRUCTURAL ELUCIDATION OF INTERSTITIAL AND SUBSTITUTIONAL POSITIONS OF VO(II), Mn(II) AND Cu(II) IONS DOPED IN ZINC AND NICKEL MALONATE COMPLEXES USING SINGLE CRYSTAL EPR TECHNIQUE

Thesis

submitted to the Pondicherry University

for the award of the degree of

DOCTOR OF PHILOSOPHY

in Chemistry

by

S. Boobalan M. Sc., M. Phil.

Research Supervisor

Prof. P. Sambasiva Rao

Department of Chemistry

Pondicherry University

Pondicherry – 605 014

India

April 2010

TO MY BELOVED FAMILY

Department of Chemistry
Pondicherry University
R. Venkatraman Nagar, Kalapet
Pondicherry - 605 014, India
Tel: 091-413 – 2654410
Fax: 091-413-2655987
Email: psr52in@yahoo.co.in

Dr. P. Sambasiva Rao
Professor and Head

Certificate

This is to certify that the thesis entitled **"Structural Elucidation of Interstitial and Substitutional Positions of VO(II), Mn(II) AND Cu(II) ions Doped in Zinc and Nickel Malonate Complexes using Single Crystal EPR Technique"** submitted to Pondicherry university, for the award of the degree of Doctor of Philosophy is a bonafide record of research work carried out by **Mr. S. Boobalan**, in the Department of Chemistry, Pondicherry University, Pondicherry – 605 014, India, under my guidance and supervision. This is to certify that the thesis represents his independent, original work without forming previously any part of the material for the award of any degree, diploma or any other similar title in any university.

(P. Sambasiva Rao)

Place : Pondicherry

Date :

Declaration

I hereby declare that the thesis entitled "Structural Elucidation of Interstitial and Substitutional Positions of VO(II), Mn(II) and Cu(II) ions Doped in Zinc and Nickel Malonate Complexes using Single Crystal EPR Technique" submitted to the Pondicherry university, Pondicherry, India, in partially fulfillment of the requirements for the award of the degree of Doctor of Philosophy is the original and independent work carried out by me, in the Department of Chemistry, Pondicherry University, Pondicherry, India under the supervision of Dr. P. Sambasiva Rao, Professor, Department of Chemistry, Pondicherry University, Pondicherry. This thesis has not been formed the basis for the award of any degree, diploma, or any other similar titles.

(S. Boobalan)

Place : Pondicherry

Date :

Acknowledgement

I have an immense pleasure in expressing my deep sense of gratitude to my guide and supervisor Dr. P. Sambasiva Rao, Professor and Head, Department of Chemistry, Pondicherry University, Pondicherry, for introducing me to this exciting field of single crystal EPR studies and suggesting me this interesting research problem. I am greatly indebted to him for his outstanding guidance, valuable ideas, and enthusiastic encouragement with patient and parental affection and for his involvement with the research work. I am delighted to express my gratitude to him in this opportunity.

My sincere thanks to the doctoral committee members Dr. R. Venkatesan, Reader, Department of Chemistry and Prof. M. S. Pandian, Head, Department of Earth Sciences, Pondicherry University, for their valuable evolving suggestions, fruitful ideas, constructive criticisms and kind encouragement throughout my research career.

I thank Prof. H. Suryaprakash Rao, Prof. K. Anbalagan, Prof. Bidhu Bhusan Das, Dr. R. Venkatesan, Dr. Bala. Manimaran, Dr. G. Vasuki, Dr. N. Dastagiri Reddy, Dr. M. Bala Krishnarajan, Dr. C. R. Ramanathan and Dr. Binoy Krishna Saha, Department of Chemistry, Pondicherry University, for their inclusive encouragement.

My thanks are due to Dr. R. V. S. S. N. Ravikumar, Asst. Prof., Department of Physics, Acharya Nagarjuna University, for his valuable suggestions and the interest he showed in this work.

I am very grateful to my seniors Dr. K. Velavan, Dr. S. Deepa, especially Dr. B. Natarajan and Dr. S. Mithira. I express my thanks to my research colleagues Mr. K. Parthipan, Mr. B. Bhagya Raju, Ms. P. Sathiya, Ms. P. Mano chitra, and Ms. P. Rama chitra, Ms. P. Saranya, Ms. R. Manju and Mrs. M. Rajeswari

I thank all Research Scholars, Department of Chemistry, Pondicherry University, and my friends for their prolonged moral support.

I remit my thanks to all office staffs, Department of Chemistry, Pondicherry University, for their appropriate help.

I would like to acknowledge the help rendered by the office staffs, Central Instrumentation Facility (CIF), Pondicherry University, for their assistance at any moment.

I thank Mr. N. Venkata Ramaiah, Department of Chemistry, Mr. S. Vijay Anand and S. Balamurugan, Department of Earth Sciences, for their timing help in UV-Visible and powder XRD studies.

I owe my existence to the meticulous care and love of my mother, father, brother, sister, and other family members.

I pay my thanks to Council of Scientific and Industrial Research, New Delhi for the financial assistance.

Finally I would like to acknowledge the benevolent GOD, without God's grace none of this would have been possible but a mere dream.

S. Boobalan

Preface

Electron Paramagnetic Resonance (EPR) spectroscopy has been developed over the past numerous decades as an experimental method to study the electronic structure of inorganic, organic, biological, solid state and surface molecular species. EPR technique detects unpaired electrons, which in turn envisages molecular structure and environment of the paramagnetic ion. This technique is also used to identify the location of first row transition metal ions doped in dia and paramagnetic complexes. Structural studies of paramagnetic ions such as VO(II), Mn(II) and Cu(II), doped in selected zinc and nickelmalonate complexes form the basis for the present thesis.

One can understand the structure of transition metal complexes, phase transitions, orientation property, oxidation state, covalency of metal ligand bond, defects, position of doped ions etc., by single crystal EPR studies of paramagnetic ions doped in paramagnetic and diamagnetic host lattices. With this aim, the differential behavior of a particular metal ion in different host lattices and different metal ions in a particular host lattice has been carried over. The first row transition metal ions like VO(II), Mn(II) and Cu(II) doped in different host lattices are studied by single crystal EPR studies. The metal ions studied in the present thesis have entered both interstitially and substitutionally in to the selected zinc and nickelmalonate complex lattices. A systematic study is carried out mainly with EPR spectroscopy. Other spectroscopic techniques such as UV-Visible spectroscopy, Fourier Transform Infrared spectroscopy and powder X-ray diffraction have also been used.

Recently, significant research efforts have been concentrated on carboxylate ligands, due to the fact that they are good candidates for the investigation of exchange coupling interactions between adjacent metal ions. Dicarboxylic ligands are frequently-used bridging ligands in the design of polynuclear complexes with interesting magnetic properties. Malonate (the dianion of 1,3-propanedioic acid) is a dicarboxylic ligand with a singular behaviour different from the other dicarboxylic ligands. It can exhibit different

coordination modes such as (a) bidentate [η^5-chelation], (b) bidentate [η^5-chelation] + unidentate, (c) bidentate [η^5-chelation] + bis(unidentate) and (d) bidentate [η^5-chelation] + bis(unidentate) + μ-oxo, in which in addition to the bidentate and bis(unidentate) coordination one of the oxygens acts as a μ-oxo bridge between two metal centres. These complementary ligands can act as bridging or blocking ligands contributing to the interconnection or isolation of the spin carriers. A comparison of other metal complexes with those of zinc complexes suggests that the reduced size of the Zn(II) coordination sphere plays an vital role in deciding the linkage of metals. Hence, three host lattices Aquomethylmelonatozinc(II), Hexaaquazincdiaquabis(malonato)zincate, Alkaline salt of the bis(malonate) metal(II) anions $\{[A(H_2O)_n]_2\ [M(mal)_2(H_2O)_m]\}$, A = Li, K and M = Ni, Zn are used. The thesis is built in eight chapters. A brief description of each chapter is given below.

Chapter 1 shows an introduction to the theoretical and basic principles of EPR spectroscopy, since EPR is the major technique employed in this thesis. The spin-Hamiltonian formalism has been introduced and the various tensors and its properties have been mentioned. The basic theorems of EPR viz., Jahn-Teller and Kramers' have also been explained in this chapter. The chapter ends with the list of references given in the text.

Chapter 2 mainly deals with experimental techniques, which includes EPR, UV-VIS, FT-IR, Powder XRD instrumentation, crystal growth methods, crystal structure of different host lattices, evaluation of the g and A tensors from EPR spectra, evaluation of the direction cosines of the various metal-ligand bonds in the host lattices, elucidation of the interstitial and substitutional position of doped metal ions in the host lattices and finally a brief discussion about the computer programs like EPR-NMR (to calculate the spin Hamiltonian parameters and to simulate the isofrequency plots) and Bruker's SimFonia program (used mainly for the simulation of powder spectra).

Chapter 3 contains the results of single crystal EPR spectroscopic investigation of VO(II) doped aqualithiumaquabismalonatozincate (here after abbreviated as ALMZ) in

room temperature at X-band frequencies. $[Li(H_2O)]_2[Zn(mal)_2(H_2O)]$ is isomorphous with $[Li(H_2O)]_2[Cu(mal)_2(H_2O)]$ (abbreviated as ALMC). It belongs to Triclinic crystal system with space group *P*1, having unit cell parameters a = 0.6851 nm, b = 0.8852 nm, c = 1.0529 nm, α = 80.65°, β = 75.04°, γ = 70.36° and Z = 2. Copper atom is five coordinated with a distorted square pyramidal environment. Four caboxylate-oxygen atoms from two crystallographically independent malonate groups build the equatorial plane around the copper atom. A water molecule occupies the apical position. Single crystal rotations in each of the three mutually orthogonal crystallographic planes namely a*b, a*c* and bc* indicate three chemically inequivalent sites, with differing intensities. We followed only one site which has high intensity. The calculated spin Hamiltonian parameters are: g_{xx} = 1.976, g_{yy} = 1.973, g_{zz} = 1.933 and A_{xx} = 7.01 mT, A_{yy} = 6.77 mT, A_{zz} = 18.01 mT. The powder spectrum also reveals the presence of only one site. Among the direction cosines of the Zn – O bonds and Li – O bonds calculated from crystallographic data of ALMZ, none of the direction cosines matches with any one of the direction cosines of principle value of g matrix. This confirms that the impurity has entered into the lattice in an interstitial position. The isofrequency plot and powder EPR spectrum have been simulated. The admixture coefficients and bonding parameters have also been calculated by using EPR and optical data. The FT-IR spectra of ALMZ and VO(II) doped ALMZ show the characteristic band frequencies. The lattice parameters calculated from powder XRD for ALMZ and VO(II) doped ALMZ matched with the lattice parameters reported from single crystal XRD of ALMC which confirms that ALMZ is isomorphous with ALMC.

Chapter 4 describes the EPR spectroscopic investigation of VO(II) ion doped in a paramagnetic host lattice, triaquapotassiumbis(malonato)nickelate $\{[K(H_2O)_{3/2}]_2[Ni(mal)_2]\}$ (abbreviated as PBMN) carried out at room temperature and low temperatures using X-band spectrometer to gain information about relaxation times. PBMN, $[K(H_2O)_{3/2}]_2[Ni(mal)_2]$ is isostructural with $[K(H_2O)_{3/2}]_2[Cu(mal)_2]$ (abbreviated as PBMC). It belongs to orthorhombic crystal system with space group Pbcn, having unit cell parameters a = 0.7398 nm, b = 1.8830 nm, c = 0.9320 nm, $\alpha = \beta = \gamma$ = 90° and Z = 4. Each copper atom is six coordinated and exhibit a 4+2 elongated octahedron

environment. Four carboxylate-oxygen atoms from two bidentate malonate ligands define the equatorial plane around the copper atom. Apical positions are occupied by two symmetry related carboxylated-oxygen atoms from other two monodentate malonate ligands. Single crystal EPR spectra indicate the presence of vanadyl impurity in a single site. Rotation of single crystal along the three orthogonal crystallographic axes has yielded spin Hamiltonian parameters g and A as: g_{xx} = 1.979, g_{yy} = 1.968, g_{zz} = 1.936 and A_{xx} = 6.92, A_{yy} = 6.02, A_{zz} = 18.12 mT respectively. Angular variation studies in all the three orthogonal planes confirm that the VO(II) ion has occupied an interstitial position in the lattice. The spin Hamiltonian parameters indicate orthorhombic nature of the impurity. The analysis of powder spectrum also reveals the presence of only one site. The isofrequency plots and powder spectrum have been simulated to confirm the spin-Hamiltonian parameters. The spin – lattice relaxation parameters have been calculated at various temperatures from line width measurements. The percentage of covalency of metal-oxygen bond has been estimated. The admixture coefficients have also been calculated. The optical absorption spectrum exhibits characteristic bands of VO(II) ion. The FT-IR and X-ray spectra of PBMN and VO(II) ion doped PBMN powder samples show identical bands, indicating no structural changes after doping.

Chapter 5 illustrates the single crystal EPR studies of Mn(II)-doped triaquadipotassiumbis(malonato)zincate $[K(H_2O)_3][Zn(mal)_2]$ (hereafter abbreviated as PBMZ) carried out at room temperature using X-band spectrometer. PBMZ, $[K(H_2O)_{3/2}]_2[Zn(mal)_2]$ is isostructural with $[K(H_2O)_3][Cu(mal)_2]$ (abbreviated as PBMC). The crystal structure is of PBMN is given in Chapter 4. Here instead of Ni we used Zn. Single crystal rotations along the three orthogonal axes show more than 30 lines pattern EPR spectra indicating the presence of two sites, one with large D value and the other with smaller D value. The calculated spin Hamiltonian parameters are:

Site 1: g_{xx} = 2.099, g_{yy} = 2.092, g_{zz} = 1.988, A_{xx} = 9.77; A_{yy} = 9.71, A_{zz} = 8.96 mT;
D_{xx} = -29.09, D_{yy} = -11.90, D_{zz} = 40.99 mT

Site 2: g_{xx} = 2.040, g_{yy} = 1.995, g_{zz} = 1.923; A_{xx} = 9.51, A_{yy} = 9.09, A_{zz} = 8.80 mT;
D_{xx} = -11.94, D_{yy} = -7.51, D_{zz} = 19.45 mT.

The direction cosines of g/A/D do not match with the direction cosines of Zn-O bonds in the host lattice for both sites, suggesting that both the Mn(II) sites entered the lattice interstitially. Various admixture coefficients, bonding and optical parameters have also been calculated. The optical absorption study confirms the lattice distortion in the crystal. The tentative assignment of FT-IR bands for Mn(II) doped PBMZ indicate a slight shift from that of PBMZ. The lattice parameters, calculated from powder XRD measurements of PBMZ and Mn(II) doped PBMZ powder sample, agree with the lattice parameters reported from single crystal XRD of PBMC which confirms the PBMZ is isomorphous of PBMC.

Chapter 6 contains the results of single crystal EPR studies of Mn(II)-doped hexaaquazincdiaquabis(malonato)zincate $[Zn(H_2O)_6][Zn(mal)_2(H_2O)_2]$ (hereafter abbreviated as HZBMZ) carried out at room temperature using X-band spectrometer. $[Zn(H_2O)_6][Zn(mal)_2(H_2O)_2]$ is isostuctural with $[Zn(H_2O)_6][Cu(mal)_2(H_2O)_2]$ (abbreviated as HZBMC). It belongs to triclinic crystal system and space group $P\bar{1}$, having unit cell parameters a = 0.5274 nm, b = 0.7504 nm, c = 1.0314 nm, $\alpha = 106.92^o$, $\beta = 99.15^o$, $\gamma = 95.81^o$ and Z = 2. The coordination polyhedron of the copper atom in the anionic unit $[Cu(mal)_2(H_2O)_2]^{2-}$ is that of an elongated octahedral CuO_6. Four carboxylate oxygens from two bidentate malonate ligands build the equatorial plane, whereas two water molecules occupy the axial sites. The zinc(II) ion in the cationic units $[Zn(H_2O)_6]^{2+}$ is coordinated to six water molecules with a slightly distorted octahedral geometry. Single crystal rotations along the three orthogonal axes show more than 30 line pattern EPR spectra indicating the presence of two types of impurity ions in the host lattice, with intensity ratio of 6:1. However, the latter could not be followed due to its low intensity during crystal rotations. The spin Hamiltonian parameters, estimated from the three mutually orthogonal crystal rotations, are: $g_{xx} = 1.972$, $g_{yy} = 2.000$, $g_{zz} = 2.023$; $A_{xx} = 8.95$, $A_{yy} = 9.48$, $A_{zz} = 9.93$ mT; $D_{xx} = -34.49$, $D_{yy} = -3.25$, $D_{zz} = 37.74$ mT and $E = 15.6$ mT. The direction cosines of one of the principal values of g match with that of Zn-O bond in the host lattice, suggesting that the Mn(II) ion entered the lattice substitutionally. The large value of E is indicative of low symmetry of the substitutional site, in accordance with the crystal structure of the HZBMC. Various admixture

coefficients, bonding and optical parameters have also been calculated. The FT-IR and X-ray spectra of HZBMZ and Mn(II) doped HZBMZ powder samples show identical bands, confirming no structural changes after doping.

Chapter 7 contains the single crystal EPR studies of Cu(II) doped aquomethylmelonatozinc(II) $[Zn(methylmelonato)(H_2O)]_n$ (hereafter abbreviated as AMMZ) carried out at 300 K. AMMZ, $[Zn(methylmelonato)(H_2O)]_n$ is isostructural with $[Cu(methylmelonato)(H_2O)]_n$ (abbreviated as AMMC) and belongs to orthorhombic crystal class with space group $Pn2_1m$, having unit cell parameters a = 0.6203, b = 0.6796, c = 0.6998 nm and Z = 2. The copper complex exhibits perfect square pyramidal structure. The apical position is filled by a water molecule and the equatorial positions are occupied by four methylmalonate oxygen atoms in which two oxygen atoms donated by bidentate methylmalonate ligand, other two oxygen atoms donated by each of two monodentate methylmalonate ligand. Angular variation of copper hyperfine lines in the three orthogonal axes shows the presence of single site in an interstitial position, with spin Hamiltonian parameters: g_{xx} = 2.075, g_{yy} = 2.100, g_{zz} = 2.379 and A_{xx} = 2.69 mT, A_{yy} = 3.04 mT, A_{zz} = 13.45 mT. The low hyperfine value for A_{zz} has been explained by considering considerable admixture between $d_{x^2-y^2}$ ground state and d_{z^2} excited state, with admixture coefficients as: a = 0.2910, b = 0.9510, c = 0.0540, d = 0.0310, e = -0.0310, where a and b correspond coefficients for d_{z^2} and $d_{x^2-y^2}$ respectively. Few other calculated parameters such as κ = 0.2802, $P = 375 \times 10^{-4}$, α^2 = 0.7783, α = 0.8822 and α' = 0.4709 indicate considerable covalency. Powder XRD, FT-IR and UV-Vis data confirm the structure of host complex and the presence of dopant ion.

Chapter 8 describes the single crystal EPR results of Cu(II) doped in Hexaaquazincdiaquabis(malonato)zincate $[Zn(H_2O)_6][Zn(mal)_2(H_2O)_2]$ (hereafter abbreviated as HZBMZ) host carried out at 300 K. $[Zn(H_2O)_6][Zn(mal)_2(H_2O)_2]$ is isostuctural with $[Zn(H_2O)][Cu(mal)_2(H_2O)]$ (abbreviated as HZBMC). The crystal structure of HZBMZ is already explained in Chapter 6. Angular variation of copper hyperfine lines in the three orthogonal axes shows the presence of single site in substitutional position. Host lattice contains two molecules per unit cell. The spin

Hamiltonian parameters calculated from the spectra are: g_{xx} = 2.034, g_{yy} = 2.159, g_{zz} = 2.388 and A_{xx} = 3.39 mT, A_{yy} = 4.89 mT, A_{zz} = 13.72 mT. The g and A tensor direction cosines are evaluated and compared with various Zn – O directions in the host lattice, which confirm that Cu(II) enters substitutionally in the lattice. The low value of A_{zz} has been explained by considering admixture of $d_{x^2-y^2}$ ground state with d_{z^2} excited state. EPR powder spectra at 300 K and 77 K give identical spin Hamiltonian parameters ($g_{\parallel}$ = 2.367, $g_{\perp}$ = 2.088, $A_{\parallel}$ = 11.47mT, $A_{\perp}$ = 2.63 mT), which matched fairly well with the single crystal data. IR, UV-Visible and powder XRD data confirm the structure and symmetry of the Cu(II) doped in host lattice.

The thesis ends with a conclusion highlighting the salient features of the present research work. Also, mention will be made about the possible further work to understand these defects in a general way and scope of further work in these important systems at higher frequencies.

Contents

CHAPTER 1

CHAPTER 2

CHAPTER 3

CHAPTER 4

CHAPTER 5

CHAPTER 6

CHAPTER 7

CHAPTER 8

SUMMARY

INTRODUCTION

1.1 Introduction:

In recent one decade, carboxylate-bridged ligands have been reported in a number of applications, for example, as potential zeolites for their magnetic [1,2], conducting [3] and non-linear optical properties [4]. Research performed on several metals (alkali and alkaline earth, transition, rare earth and actinide elements) with these ligands has provided an insight into these new properties [5]. Dicarboxylic ligands are frequently used as bridging ligands in the design of polynuclear complexes with interesting magnetic properties. Among the different carboxylates studied, Malonate (the dianion of 1,3-propanedioic acid), a dicarboxylic ligand with a singular behaviour different from the other dicarboxylic ligands, has attracted the researchers owing to the flexibility by two interesting reasons. Firstly, it can exhibit different coordination modes such as (a) bidentate [η^5-chelation] (b) bidentate [η^5-chelation] + unidentate, (c) bidentate [η^5-chelation] + bis(unidentate) and (d) bidentate [η^5-chelation] + bis(unidentate) + μ-oxo, in which in addition to the bidentate and bis(unidentate) coordination, one of the oxygens acts as a μ-oxo bridge between two metal centres. Secondly, these complementary ligands can act as bridging or blocking ligands contributing to the interconnection or isolation of the spin carriers and to form molecular magnets [6]. There has been considerable interest in the design and synthesis of transition metal complexes with carboxylate ligands in coordination chemistry because these complexes have potential application in molecular-based magnets, catalysis, supramolecular chemistry and biological systems [7-9]. Additionally, the carboxylate group provides an efficient pathway that couples the magnetic centres either ferro- or antiferrowmagnetically [10-16], the coupling constant being influenced by structural aspects such as the conformation of the bridge or the geometry of the metal environment. As an important dicarboxylate ligand, the malonate dianion acts as a chelating bidentate and adopt different carboxylate bridging coordination modes as mentioned before [6]. A comparison of other metal complexes with those of zinc complexes suggests that the reduced size of the Zn(II) coordination sphere plays an vital role in deciding the linkage of metals. Zn(II) complexes with malonate ligand have potential applications in modified metalloenzymes and in precursor systems for Zn-containing ceramic materials. Several structures of Zn(II) complexes with malonate (mal) have been reported, viz. $\{Na_2[Zn(mal)_2.2H_2O]\}_n$ [17], $\{[Zn_2(mal)_2(pyrimidine)(H_2O)].H_2O\}_n$ [18] and $[Zn_2(H_2O)_2.(mal)_2(C_4H_4N_2)]$ [19]. The structures of these complexes are polymeric

with the malonate ligand serving as bridges. To the best of our knowledge, there have been no reports of Electron Paramagnetic Resonance (EPR) and optical studies of transition metal ions such as VO(II), Mn(II) and Cu(II) doped in model biocomplexes Aquomethylmelonatozinc(II) [20], Hexaaquazincdiaquabis(malonato)zincate [6], Alkaline salt of the bis(malonate) metal(II) anions $\{[A(H_2O)_n]_2\ [Cu(mal)_2(H_2O)_m]\}$ [21], A = Li, K and M = Ni, Zn. Hence, these systems are studied mainly by single crystal EPR technique and also using UV-Visible, FT-IR and powder XRD measurements. The main EPR spectroscopic technique is discussed in detail in this Chapter, while other spectroscopic techniques are discussed in the next Chapter.

1.2 Electron Paramagnetic Resonance:

Electron paramagnetic resonance (EPR) and/or electron spin resonance (ESR) is defined as the form of spectroscopy concerned with microwave-induced transitions between magnetic energy levels of electrons having a net spin and orbital angular momentum. Electron paramagnetic resonance was discovered in 1944 by Zavoisky [22]. EPR has a wide range of applications in Chemistry, Physics, Biology and Medicine; it may be used to probe the "static" structure of solids and liquid systems and is also very useful for investigating dynamic processes. EPR has developed over the past several decades as a technique to provide information on the electronic structure of organic, inorganic, biological, solid state, and surface molecular species. These include organic free radicals, biradicals, triplet excited states and most transition metal and rare earth species. Biological applications, in addition to studies of these organic and inorganic species in biological systems, include the use of "spin labels" as probes of molecular environment in enzyme active sites and membranes. Point defects in solids and active chemical species on surfaces of catalysts are also investigated using EPR.

EPR spectra are routinely obtained for paramagnetic transition ions in crystal, chemical complexes and bio-molecules. Samples may be in the form of crystal, powder, solution and/or frozen solution. Most commonly, these should have electron spin (S), which can be any value from 1/2 to 7/2 in increments of 1/2. When the spin is odd, i.e., for example, S = 1/2, 3/2, 5/2 or 7/2, spectra are easily obtained at room temperature. However if the spin is even, i.e., for example, S = 1, 2 or 3, then the possibility of obtaining spectra depends upon a number of circumstances that are usually not met; thus the EPR of even spin systems is very specialised one. EPR has developed into a potent, multipurpose, non-destructive and non-intrusive analytical method.

EPR can provide valuable information on structural and dynamical aspects, even from current chemical and/or physical processes without influencing the process itself. Therefore, EPR is considered as an ideal complementary technique for other methods in a wide range of studies in the areas of Chemistry, Biology, Medicine, Physics, Material science, Geology et al [23-29].

1.3 EPR Theory: [23, 28, 29]

Electrons in molecular systems, by virtue of their spin and orbital motion, have spin magnetic moment μ_s and orbital magnetic moment μ_l, given by

$$\mu_s = -(2.0023 |e| h/ 4\pi m_e) S \quad (1.1)$$

$$\mu_l = - (|e| h / 4\pi m_e) L \quad (1.2)$$

where S and L are the spin and orbital angular momenta in units of $h/2\pi$, $|e|$ is the magnitude of the electronic charge and m_e is the mass of the electron. The factor 2.0023, known as free-electron gyromagnetic ratio, arises out of the 'anomalous' Zeeman effect and can be derived from Dirac's relativistic wave mechanics and includes a correction of +0.0023 due to relativistic mass variation. The total effective magnetic moment (μ), which is the vector sum of the spin magnetic moment and orbital magnetic moment can be given as

$$\mu = \mu_s + \mu_l = -\beta_e (2.0023 S + L) \quad (1.3)$$

where $\beta_e = |e| h/4\pi m_e$, is known as the Bohr magneton. For a free electron (rarely found in practical systems, except in cases such as conduction electrons or the system with ground state symbol S), the orbital contribution is zero. Hence, the interaction energy, in an applied magnetic field (B) is given by

$$E = -2\beta \mathbf{B}.\mathbf{S} \quad \text{or} \quad -g\,\beta \mathbf{B}.\mathbf{S} \quad (1.4)$$

For free electron systems, the spin moments are quantized along the applied field axis with z components $S_z = |\pm 1/2>$. It means that the time independent components of the precessing spin vectors lie either parallel or anti-parallel to the direction of B. Thus only two energy states are possible for a free electron at $\pm \underline{\beta g B S_z}$ about the unperturbed energy level, as shown in Fig. 1.1.

For a paramagnetic system with S=1/2, the magnetic moment vector can have two orientations corresponding to M_s= +1/2 and −1/2 (fig 1.1) and the energies of the levels corresponding to these orientations are $(+1/2)g\beta_e B_o$ and $(-1/2)g\beta_e B_o$ respectively. Similarly for a system with a total electron spin S, there will be (2S+1) Zeeman levels. The energy gap (ΔE) between successive energy levels is

$$\Delta E = g\beta_e B_o \quad (1.5)$$

The resonance condition is satisfied when a circularly polarized electromagnetic radiation having proper sense of precession with same frequency as that of the precessing spin is applied. If ν is the frequency of radiation, then the resonance condition is

$$\Delta E = h\nu = g\beta_e B_o \quad (1.6)$$

The resonance condition can be satisfied either keeping the field constant or varying the frequency or vice-versa. In general EPR experiments are carried out at a fixed frequency. Two common frequencies are

(i) X–band frequency (range about 9 to 9.5 GHz) where field strength of about 330 mTis employed.

(ii) Q–band frequency (range about 35 GHz) where a field strength of about 1350 mT is used.

In common X–band is used. This frequency corresponds to 3 cm microwave region. In the presence of applied magnetic field, the Boltzmann distribution is established such that the population of the upper level, i.e., $M_s = +1/2$ is lower than that at $M_s = -1/2$. The ratio of population is

$$N_+/N_- = \exp(-g\beta_e B_o/KT) \quad (1.7)$$

where N_+ and N_- are population of $M_s = +1/2$ and $M_s = -1/2$ levels respectively, K is Boltzmann constant and T is absolute temperature in Kelvin. At room temperature, $h\nu<KT$ condition is satisfied for spins leading to a population difference between the two levels of about sixteen in million spins.

Transitions between these levels are possible when the system is subjected to an oscillating electromagnetic field. It is known that the net paramagnetic moment (present as a result of Boltzmann distribution) processes about the external field axis with an angular velocity ω given by $\omega = -|e|B/2m_e$, termed as the Larmor precession frequency. A small rotating magnetic field B_1 rotating in the same sense as the net magnetization vector causes exchange of energy between itself and the system of spins causing transitions to occur between the Zeeman states. i.e., at resonance $\omega_{B1} = -|e|B_1/2m_e$. Experimentally, microwave field replaces the rotating field B_1. The alternating field is equivalent to the rotating field in EPR. The condition that the oscillating field should be applied perpendicular to the static external field has been obtained using quantum mechanics which also explains the selection rules for magnetic dipole transitions. According to the outcome of the time-dependent

perturbation theory, the time-independent transition probability is proportional to the square of the absolute value of the transition moment (P). Hence, P is given by

$$P = < \psi_j \mid V \mid \psi_i >^2 \tag{1.8}$$

where $< \psi_j \mid$ and $\mid \psi_i >$ are the initial and final state vectors and V is the time-independent part of the perturbation that connects these states. In EPR, ψ_i and ψ_j correspond to Ms values and if $B_{1x} = 2B_1 \cos\omega t$ and $V = g\beta\, B_1.S$, then

$$P = <\psi_j \mid V \mid \psi_i>^2 \quad = <-1/2 \mid g\beta B_1 \cdot S \mid +1/2>^2 \tag{1.9}$$

$$= g\beta[<-1/2 \mid B_z S_z \mid +1/2> + <-1/2 \mid B_x S_x \mid +1/2> + <-1/2 \mid B_y S_y \mid +1/2>]^2 \tag{1.10}$$

The first term in square brackets is zero. Hence, B_1 parallel to the axis of quantization will be ineffective. Also when B_1 is perpendicular to the axis of quantization, the operators S_x and S_y lead to $\psi_j = \psi_i \pm 1$ and hence the selection rule $\Delta Ms = \pm 1$. However, in triplet spin ground states, the transitions can occur at low fields with B_1 parallel to the axis of quantization. On the other hand, unpaired electrons in transition metal complexes do possess orbital angular momentum. The spin momentum and the orbital angular momentum vectors couple to give a resultant angular momentum, J, with (2J+1) degeneracy. The J values range from $\mid L+S \mid$ to $\mid L-S \mid$. The energy levels in a magnetic field B are given by

$$E = g\beta\, B\, Mj \tag{1.11}$$

The corresponding g-factors, known as the Lande g- factors are given by

$$g = 1 + [J(J+1)-L(L+1)+S(S+1)] / 2J(J+1) \tag{1.12}$$

with $J = \mid L-S \mid$ for less than half-filled d-shell and $J = \mid L+S \mid$ for more than half-filled shell.

Hamiltonian can represent interaction of the magnetic moment with the applied field B_o.

$$H = -\mu_e B_o \tag{1.13}$$

$$= g\beta_e B_o S \tag{1.14}$$

Here S includes both spin and orbital contribution and is known as effective spin or "Fictitious Spin".

The interaction involved in the case of a paramagnetic species (with particular emphasis on transition metal ions) in a crystal field is discussed in terms of a generalized Hamiltonian. If spin-operators are only considered, it is known as Spin-Hamiltonian.

The extent of coupling between spin and orbital motion depends on the exact nature of the environment of the paramagnetic ion. Surrounding ionic charges, bonded ligands etc. produce a strong electrostatic field and the spin-orbit coupling will breakdown due to the

'quenching' of the orbital angular momentum. Thus EPR systems can be divided into three main categories i.e., weak-field, intermediate field and strong field cases.

1.4 Spin Hamiltonian:

EPR data can be explained with the help of "Spin-Hamiltonian' involving smaller number of terms by use of an effective fictitious spin without information about spin-orbit coupling, the magnitude of crystal field splitting, etc. This Hamiltonian gives electron Zeeman interaction energy only and so, it is otherwise called Zeeman interaction Hamiltonian. Basically, it represents all possible interactions that affect the spin system and give rise to its energy states. For the most general hypothetical case with electronic spin $S>1/2$, and nuclear spin $I\geq1$, the effective spin Hamiltonian is made up of the following terms;

$$H_S = H_{ez} + H_{ss} + H_{hfs} + H_q + H_{nz} \tag{1.15}$$

where, H_{ez} = Electron Zeeman interaction

H_{ss} = Electron Spin-Spin interaction

H_{hfs} = Electron Spin-Nuclear Spin Hyperfine interaction ($I \neq 0$)

H_{nz} = Nuclear Zeeman interaction

H_q = Nuclear Quadrapole interaction

1.5 Hamiltonian terms:

1.5.1 Zeeman Interaction: $\mathcal{H}_{Zee}$

This arises due to the interaction of the external magnetic field with the spin and orbital magnetic moment of the electrons and nuclear spin magnetic moment and is given by

$$\mathcal{H}_{Zee} = \beta\,(L + 2S)\,B - g_n\,\beta_n\,B\,\sum_i I_i \tag{1.16}$$

where β_n is the nuclear magneton, g_n is nuclear g value and I_i are the various magnetic nuclear spins. The first term is known as the electron Zeeman interaction. The second term, which is the nuclear Zeeman interaction, is of minor importance in EPR, except in cases where the hyperfine coupling is much smaller than the nuclear Zeeman Interaction.

1.5.2 Spin-Orbit Interaction: $\mathcal{H}_{L.S}$

This represents the coupling between the magnetic moment arising from the spin and orbital motion of the unpaired electrons and can be written as:

$$\mathcal{H}_{L.S} = \sum_{j,k}\, a_{j,k}\; l_j\; S_k \tag{1.17}$$

If we neglect the electron spin and 'other-orbit' interaction, then the above term can be given in terms of the one-electron spin-orbit coupling constants ξ_i,

$$\mathcal{H}_{L.S} = \sum_i \xi_i \, l_i.S_i \tag{1.18}$$

Within the Russel-Saunders scheme, the interaction reduces to

$$\mathcal{H}_{L.S} = \lambda \, L.S \tag{1.19}$$

where λ is the spin-orbit coupling constant of the ion and is a function of the effective nuclear charge. For more than half-filled shells, λ is negative and for less than half-filled shells, it is positive. In the spin-Hamiltonian formalism, the effect of spin-orbit coupling is incorporated into 'the fictitious' spin concept.

1.5.3 Spin-Spin Interaction: $\mathcal{H}_{SS}$

When more than one unpaired electrons are involved in the systems with ground state triplet or higher spin multiplicity, direct dipole-dipole interactions among these spins lead to the splitting of the spin-states via the spin-spin interaction given by

$$\mathcal{H}_{SS} = (g\beta)^2 \sum_{j<k} \frac{S_j.S_k}{r_{jk}^3} - \frac{3(r_{jk}.S_j)\,(r_{jk}.S_k)}{r_{jk}^5} \tag{1.20}$$

When the external magnetic field is much stronger than the magnitude of spin-spin coupling constant, the above interaction becomes

$$\mathcal{H}_{SS} = (g\beta)^2 (3\cos^2\theta - 1) \frac{S_j.S_k}{r_{jk}^3} \tag{1.21}$$

Here θ is the angle between the external field and the vector joining S_j and S_k.

1.5.4 Hyperfine Interaction: $\mathcal{H}_{S\,I}$

This is a zero-field type interaction between the electron magnetic moment and the associated nuclear magnetic moment. This consists of a pure dipole-dipole type interaction described by a tensor due to unpaired p, d, f type spin-densities and an isotropic Fermi contact term for s-type spin-densities. The interaction is written as:

$$\mathcal{H}_{S.I} = g\beta \, g_n \, \beta_n \left[\left\{\sum_{i,j} \frac{S_j.I_j}{r^3} - \frac{3(S_j.r_{ij})(I_i.r_{ij})}{r^5}\right\} + \frac{8\pi}{3} \sum_{i,j} \delta(r_{ij}) \, I_i.S_j\right] \tag{1.22}$$

The first term describes an interaction of two point-dipoles and the second containing the Dirac delta function, which when integrated with the wave function vanishes except at $r_{ij} = 0$, corresponds to the isotropic interaction. Thus, in the non-relativistic approximation, only s-orbitals can contribute to isotropic coupling to the concerned nuclei.

1.5.5 Nuclear Quadrupole Interaction: $\mathcal{H}_Q$

This interaction is present in systems having nuclei with spin I ≥1 and arises due to the interaction of the nuclear electric quadrupole moment with the electric field gradient at the nucleus, generated by the surrounding electrons. It is expressed as

$$\mathcal{H}_Q = \sum_{i,j} [e^2 Q_i / 2I_i (2I_i-1)] [r^2_{ij}.I_i.(I_i+1) - 3(r_{ij}.I_i)^2] r^{-5}_{ij} \quad (1.23)$$

where Q is the nuclear electric quadrupole moment.

In Dyad operator notation, the above Spin-Hamiltonian can be expressed as

$$\mathcal{H}_S = \beta_e \mathbf{B}.\mathbf{g}.\mathbf{S} + \mathbf{I}.\mathbf{A}.\mathbf{S} + \mathbf{S}.\mathbf{D}.\mathbf{S} + \mathbf{I}.\mathbf{Q}.\mathbf{I} + \ldots \quad (1.24)$$

where g, A, D and Q are second rank tensors, whose principal axes need not coincide. These correspond to the electron g-tensor, hyperfine tensor, zero-field tensor and quadrupole coupling constant tensor respectively.

The main difference between the true spin S and fictitious spin S' is that the latter defines the effective spin-angular momentum endowed due to any orbital contribution. It is known that the spin-only g-factor deviates from the free spin value due to admixture of higher lying states into the ground state via spin-orbit coupling. Since the isotropic g-factor of a free electron is modified into a tensor when orbital momentum is not completely quenched in the principal axis system of the g-tensor, the Hamiltonian is written as

$$\mathcal{H} = \beta (B_x g_{xx} S_x + B_y g_{yy} S_y + B_z g_{zz} S_z) \quad (1.25)$$

If the tensor is cylindrically symmetric, $g_{xx} = g_{yy} = g_{zz} = g$ and $B_x = B_y = B_z = B$, then

$$\mathcal{H} = \beta[BgS] \quad (1.26)$$

And if the tensor is axially symmetric,

$$\mathcal{H} = \beta[B_z g_{\parallel} S_z + g_{\perp}(B_x S_x + B_y S_y)] \quad (1.27)$$

Similarly, the hyperfine terms, which consist of a dipolar and isotropic part, are written as:

$$\mathcal{H} = A_{xx} I_x S_x + A_{yy} I_y S_y + A_{zz} I_z S_z \quad (1.28)$$

If the unpaired electron is purely s-type, then

$$\mathcal{H} = a\, I_z\, S_z \text{ and } a = (8\pi/3)\, g\beta g_n \beta_n |\psi(0)|^2 \quad (1.29)$$

where $|\psi(0)|^2$ is the squared amplitude of the unpaired s-electron density at the nucleus. Isotropic hyperfine interaction arises due to (a) direct unpaired spin-density in an s-orbital or in a molecular orbital (MO) with s-orbital contribution, (b) spin-polarization, due to isotropic hyperfine coupling in an isolated paramagnetic atom or ion, where the electron is in a p or d orbital arises via polarization of core-s-electrons, (c) also configuration interaction between a

ground state M.O. orbital with no s-orbital contribution and states with finite s-orbital contribution.

Dipolar coupling arises out of point dipole interaction between p or d orbital with the nucleus and follows a $(3\cos^2\theta-1)$ variation given by

$$\mathcal{H}_d = g\beta g_n\beta_n(3\cos^2\theta-1)\,(1/\langle r^3\rangle) \tag{1.30}$$

In p^3 or d^5 high spin configuration, due to spherical charge distribution, dipolar-coupling vanishes. Also in paramagnetic systems in solutions, where the molecule tumbles rapidly, it averages to zero, being represented by a traceless tensor.

The signs of the experimental principal values of the hyperfine tensor cannot be inferred from EPR spectra. However, it can be estimated from the ratio of unpaired p and s densities in simple free–radicals [27]. Often hyperfine coupling to ligand-magnetic nuclei in transition metal complexes can lead to an estimate of the covalence of the metal ligand bonds, when the unpaired electron 'formally' occupies a metal nd orbital.

In systems with more than one unpaired electron, the spin-degeneracy is removed even in the absence of external magnetic field by a second spin-orbital coupling known as the zero-field interaction. This is also a dipolar type interaction and is expressed in the spin Hamiltonian as

$$\mathcal{H}_{ss} = D[S_z^2-1/3\ S(S+1)] + E(S_x^2 - S_y^2) \tag{1.31}$$

$$= D_{xx}S_{xx}^2 + D_{yy}S_{yy}^2 + D_{zz}S_{zz}^2 \tag{1.32}$$

The D_{ii}'s are the principal values of the D-tensor and E is an asymmetry parameter, depending on the deviation of the D-tensor from axial symmetry. The relative magnitudes of D and $g\beta B$ are important in perturbation treatment of the spin-Hamiltonian.

The quadrupolar term in the spin-Hamiltonian is quite analogous to the zero-field term and is given by

$$\mathcal{H}_Q = Q_{xx}I_x^2 + Q_{yy}I_y^2 + Q_{zz}I_z^2 \tag{1.33}$$

$$= Q'\,[I_z^2 - 1/3\ I\,(I+1)] + Q''\,[I_x^2 - I_y^2] \tag{1.34}$$

where Q_{ii}'s are the principal values of the quadrupole coupling constant tensor. Here, Q' is similar to D and Q" to E. In single crystals, especially when the external field is perpendicular to the symmetry axis, the analysis becomes difficult due to the presence, sometimes, of intense forbidden transitions [30].

The spin Hamiltonian parameters can be derived theoretically from the knowledge of the ground state molecular orbital and optical spectroscopic data with the use of perturbation

theory [31, 32]. It is possible to obtain bonding parameters for transition metal complexes from EPR data.

1.6 Kramers and Jahn Teller Theorems:

Kramers' theorem [33] states that a purely electrostatic field can never reduce the degeneracy of the system, if it has an odd number of electrons. Such degeneracy (generally two-fold) can be lifted only by an external magnetic field. A corollary of this theorem is that systems with odd numbers of electrons will relax differently from one with even numbers of electrons.

Jahn-Teller [34] theorem states that any non-linear molecular system in a degenerate electronic state will be unstable and will undergo distortion to form a system of lower symmetry and lower energy thereby removing the degeneracy. This is the most fascinating phenomenon in transition metal chemistry in general and EPR in particular, providing a general approach to understanding the properties of molecules and crystals and their origins.

1.7 Relaxation times and line widths:

In an S = 1/2 system, the spins can be oriented either parallel or anti-parallel to the external magnetic field and a perturbation (e.g. pulse) induces transitions between the two energy levels. The M_z magnetization in equilibrium is the result of a small surplus of spins parallel to their quantization axis. Changing the M_z magnetization involves reorientation of the microscopic magnetic moments. Transversal magnetization M_x and M_y on the other hand is given by an in-phase precession of the magnetic moments about the external field, induced e.g. by an MW pulse. Upon relaxation, the Boltzmann M_z magnetization is restored and the transversal magnetic components M_x and M_y vanishes. These changes in magnetization are associated with the spin-lattice or longitudinal relaxation time T_1 and the spin-spin relaxation time T_2, respectively. The spin-lattice relaxation relates to the characteristic lifetime of the spin state and is determined by the dissipation of energy via the thermal vibration of the lattice. T_1 is related through the Heisenberg uncertainty principle to the line width of an individual spin packet. A small T_1 leads to a smearing out of the energy levels and thus a broad resonance line. Large T_1 values are usually found for systems with isolated electronic ground states, well separated from the lowest excited states. The spin-spin relaxation is concerned with the mutual spin flips caused by dipolar and exchange interactions between the assemblies of spin in the sample. T_2 is usually much shorter than T_1 and thus the dominant

contribution to the line width. The two contributions are often summarized by relating the resultant line width of a single spin packet to a relaxation time T'_2 given by

$$\frac{1}{T'_2} = \frac{1}{T_2} + \frac{1}{2T_1} \qquad (1.35)$$

T'_2 is the relaxation time which is of importance in connection with the transverse magnetization generated and observed in pulse EPR experiments. T'_2 is temperature dependent and determines the homogeneous line width of a single spin packet. For transition metal complexes, T'_2 values are in the range of several μs at liquid helium temperatures. Among the various effects influencing T'_2, only high spin concentrations or clustering of paramagnetic molecules which may lead to a considerable shortening of the relaxation time are only mentioned.

1.8 Magnetically and chemically inequivalent sites:

A paramagnetic system with anisotropic g and A tensors will give rise to EPR resonance depending on the orientation of the magnetic field B with respect to the tensor axes. In single crystals, depending on the space group and the number of molecules per unit cell (Z), there will be several different spatial orientations of the paramagnetic sites. Species that are chemically identical (i.e., they are described by identical spin Hamiltonian parameters) but are spatially oriented differently are referred to as magnetically distinct sites. It is also possible that due to charge compensation process [35, 36] in the lattice, many different sets of spin Hamiltonian parameters (although these may differ only slightly) exist. The species themselves would be expected to be identical when the charge-compensating vacancies are not taken into account. Such sites are referred to as chemically distinct sites. These chemically distinct sites are necessarily magnetically distinct, whereas the converse need not necessarily hold.

1.9 EPR Applications:

Therefore, EPR is considered as an ideal complementary technique for other methods in a wide range of studies in the areas of Chemistry, Biology, Medicine, Physics et al [23-28]. The typical applications in each area are outlined below:

Chemistry

Measurement of magnetic susceptibility.

Atoms or ions with partially filled inner electron shells (transition metals).

Molecules with odd number of electrons.

Molecules with even number of electrons (triplet states).

Oxidation and reduction processes.

Biradicals and triplet state molecules.

Reaction kinetics

Structure, dynamics and reaction of polymers.

Short-time behaviour of organic free radicals produced by radiation.

Organo - metallic, Catalysis, Molecular Magnets etc.,

Biology

Enzymatic reactions

Photosynthesis

Metallo-proteins

Spin label and spin probe techniques

Control of irradiated food

Saturation transfer and vector EPR techniques for the study of molecular motions.

Medicine

Radical initiated carcinogenesis

Free radicals in living tissues

Radiation dose assessment

Oxygen concentration measurement

Concentrations and kinetics of short lived radicals by spin trapping.

Physics

Conduction electrons in metals, non-metallic conductors and semiconductors

Defects in crystals

Optically detected magnetic resonance

Relaxation properties, phonon densities.

Material science

Polymers

Glasses

Superconductors

Corrosion

Fullerenes

Applications of EPR also extend to geological and archaeological dating, radiation dosimetry and microscopic magnetic resonance imaging studies [37] and estimating the age of fossils [38].

References:

[1] M. Munakata, L.P. Wu T.K. Sowa, Adv. Inorg. Chem., 46 (1999) 173; C. Janiak, Angew. Chem., Int. Ed. Engl., 36 (1997) 1431.

[2] O. Kahn, C.J. Martinez, Science, 279 (1998) 44; O. Sato, T. Iyoda, A. Fujishama, K. Hashimoto, Science, 271 (1996) 49.

[3] M. Munakata, C.L. Ning, T.K. Sowa, M. Maekawa, Y. Suenaga, T. Horino, Inorg. Chem., 37 (1998) 5651.

[4] W. Lin, Z. Wang, L. Ma, J. Am. Chem. Soc., 121 (1999) 11249; Y.K. Shan, R.H. Huang, S.D. Huang, Angew. Chem., Int. Ed., 38 (1999) 1751.

[5] J.G. Kang, S.K. Yoon, Y. Sohn, J.G. Kim, Y.D. Kim, II. H. Suh, J. Chem. Soc., Dalton Trans., (1999) 1467; I.G. de Muro, F.A. Mautner, M. Insausti, L. Lezama, M.I. Arriortua, T. Rojo, Inorg. Chem., 37 (1998) 3243.

[6] Y. Rodriguez-Martin, M. Hernandez-Molina, F.S. Delgado, J. Pasan, C. Ruiz-Perez, J. Sanchiz, F. Lloret, M. Julve, Cryst. Eng. Comm., 4 (2000) 522.

[7] L. Li, D. Liao, Z. Jiang, S. Yan, Inorg. Chem., 41 (2002) 421.

[8] Z. Shi, L. Zhang, S. Gao, G. Yang, J. Hua, L. Gao, S. Feng, Inorg. Chem., 39 (2000) 1990.

[9] M. Deverex, M. McCann, V. Leon, M. Geraghty, V. McKee, J. Wikaira, Polyhedron, 19 (2000) 1205.

[10] C. Oldham, in: G. Wilkinson, R.D. Gillard, J.A. McCleverty (Eds.), “Comprehensive Coordination Chemistry”, vol. 2, Pergamon Press, Oxford, 1987.

[11] D.K. Towle, S.K. Hoffmann, W.E. Hatfield, P. Singh, P.Chaudhuri, Inorg. Chem., 27 (1988) 394.

[12] P.R. Levstein, R. Calvo, Inorg. Chem., 29 (1990) 1581.

[13] F. Sapin˜ a, E. Escriva´, J.V. Folgado, A. Beltra´n, A. Fuertes, M. Drillon, Inorg. Chem., 31 (1992) 3851.

[14] E. Colacio, J.P. Costes, R. Kiveka¨s, J.P. Laurent, J. Ruiz, Inorg. Chem., 29 (1990) 4240.

[15] E. Colacio, J.M. Domı´nguez-Vera, J.P. Costes, R. Kiveka¨ s, J.P. Laurent, J. Ruiz, M. Sundberg, Inorg. Chem., 31 (1992) 774.

[16] E. Colacio, J.M. Dominguez-Vera, R. Kivekäs, J.M. Moreno, A. Romerosa J. Ruiz. Inorg. Chim. Acta, 212 (1993) 115.

[17] D.D. Lin, L. Zhang, D.J. Xu, Acta Cryst. E, 59 (2003) m1010.

[18] F.S. Delgado, J. Sanchiz, F. Lloret, C. Ruiz-Perez, M. Julve, Cryst. Eng. Comm., 5 (2003) 280.

[19] X. Zhang, C. Lu, Q. Zhang, S. Lu, W. Yang, J. Liu, H. Zhuang, Eur. J. Inorg. Chem., 6 (2003) 1181.

[20] J. Pasan, J. Sanchiz, F. Lloret, M. Julve, C. Ruiz-Perez, Cryst. Eng. Comm., 9 (2007) 478.

[21] F.S. Delgado, C. Ruiz, J. Sanchiz, F. Lloret, M. Julve Cryst. Eng. Comm., 8 (2006) 507.

[22] E. Zavoisky, J. Phys., U.S.S.R., 9 (1945) 211.

[23] A. Abragam, B. Bleaney, "Electron Paramagnetic Resonance of Transition Metal Ions", Clarendon Press, Oxford, 1970.

[24] J.A. Weil, J.R. Bolton, J.E. Wertz, "Electron Spin Resonance: Elementary Theory and Practical Applications", Wiley - Interscience, New York, 1994.

[25] B.R. McGarvey, "Transition metal Chemistry" (R.L. Carlin, Ed.) Dekker, New York, 1968.

[26] L. Kevan, M.K. Bowman, "Modern Pulsed and Continuous Wave Electron Spin Resonance", John Wiley and Sons, New York, 1989.

[27] P.W. Atkins, M.C.R. Symons, "Structure of Inorganic Radicals", Elsevier, Amsterdam, 1967.

[28] J.R. Pilbrow, "Transition ion Electron Paramagnetic Resonance", Clarendon Press, Oxford, 1990.

[29] W. Gordy, "Theory and Applications of Electron Spin Resonance", John Wiley & Co, New York, 1980.

[30] J.R. Byberg, S.J.K. Jensen, L.T. Muss, J. Chem., Phys., 46 (1967) 131.

[31] D. Kivelson, R. Neiman, J. Chem. Phys., 35 (1961) 149.

[32] H.R. Gersmann, J.D. Swalen, J. Chem. Phys., 36 (1962) 3221.

[33] H.A. Kramers, Proc. Amsterdam Acad. Sci., 2 (1930) 432.

[34] H.A. Jahn, E. Teller, Proc. Roy. Soc., (London), Ser. A161 (1937) 220.

[35] P. Sambasiva Rao, S. Subramanian, Mol. Phys., 39 (1980) 935.

[36] P. Sambasiva Rao, S. Subramanian, Mol. Phys., 54 (1985) 415.

[37] F.E. Mabbs, D.C. Collison, "Electron Paramagnetic Resonance of Transition Metal Compounds", Elsevier, Amsterdam, 1992.

[38] M. Ikeya, "New applications of Electron Spin Resonance: Dating, Dosimetry and Microscopy", World Scientific, Singapore, 1993.

EXPERIMENTAL TECHNIQUES

2.1 Introduction:

This chapter discuss briefly about the EPR instrumentation, crystal growth, crystal structure of the host lattices, and interpretation of powder and single crystal EPR spectra. The procedure for the calculation of the direction cosines of the metal - ligand directions from single crystal data is also mentioned. Spin-Hamiltonian parameters from single crystal EPR spectra and Simulation of isofrequency plots are done by using the program EPR-NMR. The simulation of powder spectra are obtained by using the program SimFonia.

Due to dipole interactions as well as spin exchange interactions, EPR spectra are not usually recorded in pure paramagnetic samples (magnetically concentrated samples). Hence, in order to derive information confined to individual paramagnetic entities, they need to be separated, i.e., magnetically diluted. In solution samples, this condition is readily achieved at low concentrations. In solid samples, two common methods are known. One is irradiation method, where as the other one is doping method which is used in our work. The irradiation method is to produce the paramagnetic centres in a diamagnetic lattice. The common method of attaining this is radiation damage using UV, X- ray or γ-rays. This technique may be employed in pure host lattice or a doped host lattice. However, the paramagnetic centres of this type produced by this technique are not considered in the present thesis. In doping method, the paramagnetic impurity is doped in a diamagnetic or paramagnetic lattice, which is EPR inactive at room temperature. When the temperature of the sample is lowered, the paramagnetic ion of the host lattice becomes EPR active and leads to the broadening of the hyperfine lines from which the spin-lattice relaxation times between the host and the impurity are calculated. The dopant concentration is quite low. This leads to well-resolved EPR spectra, free from dipole and exchange interactions. Such doping is quite common with transition metal complexes. In these cases, the dopant substance does not necessarily have the same crystal structure as the host lattice.

2.2 Instrumentation:

2.2.1 EPR spectrometer:

The details of instrumentation and measurement techniques have been discussed extensively in the literature [1, 2]. From the resonance condition $h\upsilon = g\beta B$, it follows that the EPR spectra can be measured by fixed frequency and variable field or vise-versa; it is

always convenient to follow the former procedure. Depending upon the irradiation frequency, EPR spectrometers are classified as L, S, C, X, P, K, Q, U, V, E, W, F, D and J band spectrometers for which the approximate frequency ranges are 1, 3, 4, 10, 15, 24, 35, 50, 65, 75, 95, 111, 140, 285 GHz respectively with the corresponding magnetic field required for a free electron to resonance. The most common ones are X and Q band spectrometers. At X-band, the frequency is normally around 9 GHz, with free-electron resonance field at ~330 mT, while at Q-band, the corresponding values are 35 GHz and 1350 mT.

In order to observe a well resolved EPR spectrum, one has to operate the spectrometer under optimum conditions of microwave power, modulation amplitude, spectrometer gain, filter time constant, scan range and scan time. The work described in this thesis has been carried out on a JEOL JES-TE100 ESR spectrometer operating at X-band frequencies, having a 100 kHz field modulation to obtain a first derivative EPR spectrum. For single crystal X-band work, the crystal was mounted at the end of a Perspex rod with 'quick fix' and then inserted into the cavity and rotated a goniometer device. The other end of the Perspex rod was attached to a large protractor, calibrated in degrees. An accuracy of θ=2 in the orientation of the crystal with respect to the magnetic field could be achieved by this set up. The axis of rotation was always perpendicular to the magnetic field. DPPH, with a g value of 2.0036, has been used for g-factor calculations. The variable temperature spectra are recorded using ES-DVT3 variable temperature controller and 77 K spectra are recorded using ES-UCD3X insertion type Dewar.

2.2.2 UV-VIS, FTIR and Powder XRD:

UV-VIS spectroscopy is another analytical technique used in the solid state mainly to prove the formation of the complexes. The optical spectrum has been recorded for samples at room temperature using Varian Cary 5000 UV-VIS NIR spectrophotometer. UV-Vis spectroscopy is usually applied to molecules and inorganic ions or complexes in solution and powder. The absorption of ultraviolet or visible (UV-Vis) light by a molecule can excite electron from lower energy, highest occupied molecular orbital (HOMO) to higher energy, lowest unoccupied molecular orbital (LUMO). This process is called an electronic transition. The specific wavelengths of light absorbed depend on the types of functional groups present in the molecule and this information is useful for qualitative identification of the functional groups.

The FTIR spectra are recorded using Shimadzu FTIR-8300/8700 spectrometer, in the frequency range 4000-400 cm^{-1}. The absorption of infrared light by a molecule will cause excitation of the vibrational motions of the atoms present. Different types of bonds in the molecule will absorb light of different wavelengths, thus allowing qualitative identification of certain bond types in the sample. The measurements are made using almost transparent KBr pellets containing fine powdered samples at room temperature. Fourier transform infrared spectroscopy is employed to identify the nature of the bonding between the various groups and the metal ions present in the complex. Depending on the environment around the functional group, a shift in the stretching and bending vibrations is generally observed.

The powder X-ray diffraction studies are carried out using PANalytical X'pert PRO Diffractometer with Cu-Kα radiation of wavelength λ = 1.5406 Å. The powder X-ray diffraction is used to identify and characterize the powder samples possessing the long rang and short rang order respectively in the crystalline materials.

2.3 Crystal growth:

Single crystals give more information from EPR measurements than powders and solutions. Hence, a brief discussion about crystal growth is mentioned. The aim in growing crystals for a single crystal EPR experiment is to grow single crystals of suitable size. The optimum size for a crystal is one which has dimensions of 0.2-0.4 mm in at least two of the three dimensions. A number of crystals with different paramagnetic dopant have to be prepared using various techniques [3-6] such as slow evaporation method, slow cooling, and variation on slow evaporation and slow cooling, vapour diffusion, solvent diffusion, reactant diffusion, sublimation, convection, counter ions, ionization of neutral compounds etc.

Among the different techniques, slow evaporation technique is the main and simplest technique to grow single crystals. All the single crystals studied in the thesis are prepared using the slow evaporation technique. The evaporation of solvents makes the solution supersaturated so that, it attempts to achieve the equilibrium saturated state by rejecting the seed crystals to solution. The factors that control the growth process are (1) character of the solution (2) effect of additives and (3) operating variable such as the degree of super saturation and the temperature range.

The choice of solvent is an important factor that determines the growth of a crystal from solution. Growth of a large crystal is virtually impossible unless a solvent is found in which the solute is appreciably soluble. In the present work, water is used as the solvent for all crystal growth. No additives are added to the solution except the dopant. The rate of

growth depends on the temperature at which the solution is maintained. At higher temperatures, the growth rate will be high. All the crystals are grown at room temperature.

2.4 Crystal structure of the host lattices:

A brief introduction of the various host lattices employed in this thesis have been presented here. The details of crystal structures are discussed in the respective chapters.

Aqualithiumaquabismalonatozincate $[Li(H_2O)]_2[Zn(mal)_2(H_2O)]$ (ALMZ) is isomorphous with $[Li(H_2O)]_2[Cu(mal)_2(H_2O)]$ (abbreviated as ALMC) [7]. It belongs to triclinic crystal system with space group *P*1, having unit cell parameters a = 0.6851 nm, b = 0.8852 nm, c = 1.0529 nm, α = 80.65° β = 75.04° γ = 70.36°, and Z = 2. The copper atom is five coordinated with a distorted square pyramidal environment. Four caboxylate-oxygen atoms from two crystallographically independent malonate groups build the equatorial plane around the copper atom. A water molecule occupies the apical position.

Triaquapotassiumbis(malonato)nickelate, $[K(H_2O)_{3/2}]_2[Ni(mal)_2]$ (PBMN) and Triaquadipotassiumbis(malonato)zincate $\{[K_2(H_2O)_3][Zn(mal)_2]\}$(hereafter abbreviated as PBMZ) are isostructural with $[K(H_2O)_{3/2}]_2[Cu(mal)_2]$ (abbreviated as PBMC) [7]. It belongs to orthorhombic crystal system with space group Pbcn, having unit cell parameters a = 0.7398 nm, b = 1.8830 nm, c = 0.9320 nm, $\alpha = \beta = \gamma = 90°$, and Z = 4. Each copper atom is six coordinated and exhibit a 4+2 elongated octahedron environment. Four carboxylate-oxygen atoms from two bidentate malonate ligands define the equatorial plane around the copper atom. Apical positions are occupied by two symmetry related carboxylated-oxygen atoms from other two monodentate malonate ligands.

Hexaaquazincdiaquabis(malonato)zincate, $[Zn(H_2O)][Zn(mal)_2(H_2O)]$ (abbreviated as HZBMZ) is isostuctural with $[Zn(H_2O)][Cu(mal)_2(H_2O)]$ (abbreviated as HZBMC) [8]. It belongs to triclinic crystal system and space group $P\bar{1}$, having unit cell parameters a = 0.5274 nm, b = 0.7504 nm, c = 1.0314 nm, α = 106.92°, β = 99.15°, γ = 95.81° and Z = 2. The coordination polyhedron of the copper atom in the anionic unit $[Cu(mal)_2(H_2O)]^{2-}$ is that of an elongated octahedral CuO_6. Four carboxylate oxygens from two bidentate malonate ligands build the equatorial plane, whereas two water molecules occupy the axial sites. The zinc(II) ion in the cationic units $[Zn(H_2O)]^{2+}$ is coordinated to six water molecules with a slightly distorted octahedral geometry.

Aquomethylmelonatozinc(II), $[Zn(methylmelonato)(H_2O)]_n$ (abbreviated as AMMZ) is isostructural with $[Cu(methylmelonato)(H_2O)]_n$ (abbreviated as AMMC) [9] and belongs to orthorhombic crystal class with space group $Pn2_1m$, having unit cell parameters a = 0.6203

nm, b = 0.6796 nm, c = 0.6998 nm, $\alpha = \beta = \gamma = 90°$ and $Z = 2$. The copper complex exhibits perfect square pyramidal structure. The apical position is filled by a water molecule and the equatorial positions are occupied by four methylmalonate oxygen atoms in which two oxygen atoms donated by bidentate methylmalonate ligand, other two oxygen atoms donated by each of two monodentate methylmalonate ligand.

2.5 Interpretation of EPR spectra:

It is apparent from the theoretical treatment that the interpretation of spectra means, primarily, determination of i) g-factors, ii) hyperfine coupling parameters iii) concentrations, iv) relaxation times, v) line-widths. As one can measure EPR spectra from solution, powder and single crystal samples, the procedure to obtain spin-Hamiltonian parameters from theses spectra must be known. A brief discussion is mentioned below. In order to calculate the g and A values, the following expression has been used to calculate g factor:

$$g = (g_{DPPH} - B_{DPPH})/B \quad (2.1)$$

where B is the magnetic field position at the EPR peak, B_{DPPH} is the field position corresponding to DPPH and g_{DPPH} is the g-value of DPPH which is equal to 2.0036. One can as well calculate the g-value directly using the spectrometer frequency (υ) at which resonance occurs. The expression is as follows

$$g = 71.44836 \text{ X } \upsilon \text{ (GHz)} / B \text{ (mT)} \quad (2.2)$$

The hyperfine coupling constant 'A' is given by the field separation between the hyperfine components. If the spacing is unequal, an average of them is taken to be the value of A. For n number of hyperfine lines, the average hyperfine value is

$$A = (B_n - B_1) / (n-1) \quad (2.3)$$

where B_n is the field position for the n^{th} hyperfine line and B_1 is the first hyperfine line field position.

In the present thesis, EPR spectra are recorded for samples, both in single crystal and poly-crystalline forms. A brief outline of the interpretation of the data is given below.

2.5.1 Polycrystalline:

It is called powders when a sufficient number of randomly oriented small crystals are present. Hence the spectrum is an envelope of statistically weighed average of all these molecules having different orientations. The theory of powder line shapes on EPR has been dealt in detail [10-12]. In powders, each paramagnetic species is likely to have the same surroundings as in the single crystal. Thus the spectral parameters are expected to be the

same. And it is assumed that no change is produced in the immediate surroundings of the spin species and hence no new EPR species are created. But in some cases, there may be partial orientation of the magnetic species rather than complete randomness. And in some other cases, the static magnetic field can cause partial ordering of crystallites. However the molecular framework cannot be obtained from the powder spectra. Powder spectra become more complicated, when more than one type of species is present. However, this problem can be overcome when the spectra are measured at different frequencies and sorting out the field dependent and field independent terms in the Hamiltonian. The orientation axes and hence with respect to molecular framework cannot be obtained from powder data. This moves us towards the single crystal EPR. Moreover, powder spectra are used to cross check the crystal data and almost they agree well with each other.

2.5.2 Single crystal:

The procedure for the extraction of principle values of the magnetic tensors from single crystal studies has formed extensive coverage in literature as described by many authors [13-18]. The method consists of measuring the variation of $g^2(\theta)$ for rotations about three mutually perpendicular axes in the crystal. Jacobi diagonalization of this matrix gives rise to the eigen values corresponding to the principal values of the g tensor and the transformation matrix, which diagonalizes the experimental g^2 matrix, provides the direction cosines of these tensors with respect to the three orthogonal rotations. In the case of hyperfine tensor, when g is not highly anisotropic, the same procedure as above can be adopted.

2.6 Calculation of Direction cosines:

2.6.1 Direction cosines of the substitutional sites:

Single crystal X-ray analysis data provides the positional parameters p, q, r and the unit cell dimensions a, b, c, and angles α, β and γ. For crystal system with non-orthogonal crystal axes, the positional parameters p, q, r of the various atoms can be converted to an orthogonal framework and the Cartesian co-ordinates x, y, z could be calculated using the relation

$$\begin{pmatrix} x \\ y \\ z \end{pmatrix} = \begin{pmatrix} a & b\cos\gamma & c\cos\beta \\ 0 & b\sin\gamma & (c/\sin\gamma)(\cos\alpha - \cos\beta\cos\gamma) \\ 0 & 0 & d \end{pmatrix} \begin{pmatrix} p \\ q \\ r \end{pmatrix} \qquad (2.4)$$

where $d = [\, c^2 - c^2\cos^2\beta - (c^2 / \sin^2\gamma)(\cos\alpha - \cos\beta\cos\gamma)^2]^{1/2}$

By setting the metal atom as the origin, the coordinates of the various atoms in the crystal surrounding the metal are calculated. The normalized Cartesian co-ordinates of these atoms give the direction cosines of the metal-ligand bond of the co-ordination polyhedron. The direction cosines of these metal-ligand bonds can be compared with the direction cosines of the g and A- tensors, obtained by the program EPR-NMR [21]. Sometimes, it is found that the magnetic tensor directions coincide with some of the bond directions, which may not be so in low symmetry cases.

2.6.2 Direction cosines of interstitial sites:

As in the case of substitutional sites, the direction cosines of metal – ligand bonds are calculated for interstitial sites also. But none of the direction cosines of metal-ligand bonds are matched with the direction cosines of any one of the g and A. So, a number of interstitial positions for dopant ion are assumed from the X-ray data of the host lattice. From the fractional coordinates and unit cell dimension values of the X-ray data, the Cartesian coordinates are calculated for host lattice metal atoms and surrounding ligand atoms in a unit cell. The midpoint of opposite ligand atoms is taken as the location of dopant ion. One of the interstitial positions is suggested for the dopant ion of which its direction cosines matched with one of the g and A direction cosines.

2.7 Spin-lattice relaxations:

If a paramagnetic ion is incorporated into a paramagnetic host, it will be interesting to study the nature and extent of dipolar interaction. As Ni(II) is EPR silent at room temperature, it is possible to successfully analyse the data at this temperature, as if we are dealing a paramagnetic system in a diamagnetic host lattice. However, as the temperature is lowered, a tremendous change in the line width has been noticed, due to the dipole-dipole interaction between the paramagnetic host and the impurity. Hence, a particular orientation is selected from the crystal orientation and the variable temperature measurements are made, from which the line widths (ΔB) are measured. It is noticed that as the temperature is decreased, the line width increases with a decrease in intensity and below a certain temperature, the peaks broadened almost to a straight line. This type of resonance broadening is noticed even from the powder sample. This type of line broadening is mainly due to the dipolar interaction of the host paramagnetic lattice and the impurity. The line-width variation of the impurity hyperfine lines in paramagnetic lattice can be understood on the basis of host spin-lattice relaxation mechanism. The fast spin-lattice relaxation of the

host ions can randomly modulate the dipolar interaction between the paramagnetic host and the impurity ions resulting in "Host spin-lattice relaxation narrowing" [19]. When the spin-lattice relaxation narrowing mechanism is effective, the host spin-lattice relaxation time (T_1) is given by [19, 20]

$$T_1 = (3/7)(h/2g_h\beta)(\Delta B_{imp}/Bd^2_d) \quad (2.5)$$

$$Bd^2_d = 5.1(g_h\beta n)^2 S_h(S_h+1)$$

where,

g = the host g value

S_h = the effective host spin and it is taken to be 1/2

n = the number of host spins per unit volume which can be calculated from the crystallographic data of the crystal lattice. Here, $n = N_A(\rho/M)$, where N_A – Avogadro number, M – Molecular weight, ρ - Density.

ΔB_{imp} = the impurity line width.

The calculated spin-lattice relaxation times (T_1) are plotted against temperature and the graph indicates that as the temperature decreases the spin-lattice relaxation time T_1 increases.

2.8 Computer Program EPR-NMR [21]**:**

The program sets up spin-Hamiltonian (SH) matrices and determines their eigen values (energies) using "exact" diagonalization. It is a versatile program, having many operating models tailored to a variety of applications [21].

2.8.1 SimFonia powder simulation:

The simulation of the powder spectrum is generally carried out to verify the agreement between the experimentally calculated spin Hamiltonian parameters with those predicted from theoretical view. The simulation of the powder spectrum is done using the computer program SimFonia developed and supplied by Brucker Company. The algorithm used in the SimFonia program for powder simulation is based on perturbation theory, which is an approximation. The assumption made in the simulations is that the electron Zeeman interaction is the largest, followed by the zero-field splitting, hyperfine interaction, nuclear quadrupole interaction and the nuclear Zeeman term is the smallest. Perturbation theory works best when the ratio between the successive interactions is at least ten. If the limits exceeded, perturbation theory still gives a good picture of EPR spectrum; however, it may not be suitable for the quantitative analysis.

The SimFonia powder simulation program simulates EPR spectra for systems having electron spin 1/2 to 7/2. For spin greater than 1/2, the zero-field splitting terms (D and E) are implemented. There are essentially no restrictions on the spin of the nuclei. All the naturally occurring spins have been programmed.

SimFonia can simulate both types of line shapes i.e., Lorentzian and Gaussian-complicated spectra. Detailed theory of the powder spectra simulation can be obtained from the references [22, 23].

References:

[1] D.J.E. Ingram (ed.), "Biological and Biochemical Applications of Electron Spin Resonance", Adam Hilder LTD, London, 1969.

[2] C.P. Poole, "Electron Spin Resonance", 2nd Ed., Dover Publications, USA, 1996.

[3] C. Bridle, T.R. Lomer, Acta Cryst., 19 (1965) 483.

[4] H. Hope, J. Appl. Cryst., 4 (1971) 333.

[5] D.J. Watkin, J. Appl. Cryst., 5 (1972) 250.

[6] Margaret C. Etter, Paul W. Baures, J. Am. Chem. Soc., 110 (1988) 639.

[7] F.S. Delgado, C. Ruiz, J. Sanchiz, F. Lloret, M. Julve, Cryst. Eng. Comm., 8 (2006) 507.

[8] Y.R. Martin, J. Sanchiz, C.R. Perez, F. Lloret, M. Julve, Cryst. Eng. Comm., 4 (2002) 631.

[9] J. Pasan, J. Sanchiz, F. Lloret, M. Julve, C. Ruiz-Perez, Cryst. Eng. Comm., 9 (2007) 478.

[10] E.K. Kneubuhl, J. Chem. Phys., 33 (1960) 1074.

[11] R.H. Sands, Phys. Rev., 99 (1955) 1222.

[12] J.A. Ibers, J.D. Swallen, Phys. Rev., 127 (1962) 1914.

[13] J.E. Geusic, L.C. Brown, Phys. Rev., 112 (1958) 64.

[14] J.A. Weil, J.H. Anderson, J. Chem. Phys., 28 (1958) 864.

[15] A. Lund, T. Vannagard, J. Chem. Phys., 42 (1965) 2979.

[16] M.H.L. Pyrce, Proc. Phys. Soc. A, 63 (1950) 25.

[17] W.G. Waller, Max T. Rogers, J. Mag. Res., 9 (1973) 92.

[18] D.S. Schonland, Proc. Phys. Soc., 73 (1959) 788.

[19] T. Mitsuma, J. Phys. Soc. Jpn., 17 (1962) 128.

[20] S.K. Mishra, Magn. Reson. Rev., 12 (1987) 191.

[21] EPR-NMR Program developed by F. Clark, R.S. Dickson, D.B. Fulton, J. Isoya, A. Lent, D.G. McGavin, M.J. Mombourquette, R.H.D. Nuttall, P.S. Rao, H. Rinneberg, W.C. Tennant, J.A. Weil, University of Saskatchewan, Saskatoon, Canada, 1996.

[22] A. Abragam, B. Bleaney, "Electron Paramagnetic Resonance of Transition metal Ions", Clarendon, Oxford, 1970.

[23] J.R. Pilbrow, "Transition Ion Electron Paramagnetic Resonance", Clarendon, Oxford, 1990.

EPR AND OPTICAL SPECTRAL INVESTIGATIONS OF VO(II) ION DOPED IN AQUALITHIUMAQUABISMALONATOZINCATE SINGLE CRYSTAL

3.1 Introduction:

Electron Paramagnetic Resonance (EPR) studies in diamagnetic host lattices by incorporating paramagnetic transition metal ions gives information about the strength of the ligand field around the central metal atom. In these cases, the resonances are sharp due to the absence of dipole-dipole interaction. Vanadyl ion, i.e., VO(II), being one of the most stable molecular paramagnetic transition metal ion which is widely used as an EPR probe to understand phase transitions, distortion, strength and magnitude of crystal fields, relaxation times, etc. Vanadium exists as bivalent, trivalent and tetravalent. Out of these, the ion commonly exists as VO(II), with a single unpaired 3d electron bound to an oxygen atom by strong bond in its tetravalent state. The orientation of the V=O bond in complexes depends on the nature of the ligands and hence shows very interesting results [1-4]. Most of the EPR results reported for this ion can be classified into two types, one in which the vanadyl ion freely rotates at normal temperatures and second category in which the ion is preferentially oriented. For example, if the ligands are water or sulfate ions, the vanadyl ion has fixed orientation, in others, it has a random orientation. In addition, the analysis of the EPR spectra of VO(II) ion in various host lattices indicates that the paramagnetic impurity was found to enter the host lattice, predominantly as substitutionally [5-8]. However, interstitial position or both are also known [9, 10]. The importance of malonato ligand in treating malignant tumors when coordinated with platinum is known (United States Patent 4140707). Coordination polymer compounds containing malonic acid as a ligand have been recently intensively studied due to their potential application as materials in molecular electronics, catalysts, biologically active compounds, molecular-based magnetic materials, microporosity, electrical conductivity, non-linear optical activity, etc. [11, 12]. Malonic acid acts as a ligand with various dentate abilities. Additionally, the carboxylate group provides an efficient pathway that couples the magnetic centres either ferro- or antiferromagnetically [13-19]. In view of this importance of the ligand, the present single crystal EPR study of VO(II) in aqualithiumaquabismalonatozincate has been undertaken to identify the location and nature of impurity in the host lattice.

3.2. Material and Methods:

3.2.1 Preparation of single crystal of VO(II)-doped $[Li(H_2O)]_2[Zn(mal)_2(H_2O)]$:

Malonic acid, zinc(II) basic carbonate, lithium hydroxide were purchased from commercial sources and used as received. $[Li(H_2O)]_2[Zn(mal)_2(H_2O)]$ was synthesized by adding solid zinc(II) basic carbonate to an aqueous solution of malonic acid under continuous stirring. The suspension was heated at 40 – 50° C, until a colorless solution was obtained. This solution was filtered and mixed with an aqueous solution of lithium hydroxide. To this solution, five different concentrations of vanadyl sulfate (0.5, 1.0, 1.5, 2.0 and 5.0 %) were added as paramagnetic impurity while adding zinc(II) basic carbonate. All the crystals were transparent and light blue color with well shaped and separated out on concentrating the solution at room temperature. Aqualithiumaquabismalonatozincate is abbreviated here as ALMZ.

3.2.2 EPR Measurements:

EPR spectra are recorded at 300 K on a JEOL JES-TE100 ESR spectrometer operating at X-band frequencies, having a 100 kHz field modulation to obtain the first-derivative EPR spectrum. 1,1-Diphenyl-2-picrylhydrazyl (DPPH) with a g-value of 2.0036 is used as a reference for g-factor calculations.

3.2.3 UV-Visible, FT-IR, Powder XRD Measurements:

The optical spectrum has been recorded at room temperature using a Varian Cary 5000 ultraviolet-visible (UV-Vis) near-infrared spectrophotometer in the range of 200-1300 nm. FT-IR spectra are recorded for doped and undoped materials on a Shimadzu FT-IR-8300/8700 spectrometer, in the frequency range of 4000-400 cm^{-1}. The measurements are made using almost transparent KBr pellets containing fine-powdered samples at room temperature. Powder XRD studies are carried out for doped and undoped materials on a PANalytical X'pert PRO diffractometer with Cu Kα radiation of wavelength λ = 0.15406 nm, 2θ values between 5-75°, at room temperature.

3.3 Crystal structure:

$[Li(H_2O)]_2[Zn(mal)_2(H_2O)]$ is isostructural with $[Li(H_2O)]_2[Cu(mal)_2(H_2O)]$ [20]. It belongs to triclinic crystal system with space group *P*1, having unit cell parameters a = 0.6851 nm, b = 0.8852 nm, c = 1.0529 nm, α = 80.65°, β = 75.04°, γ = 70.36° and Z = 2. The copper atom is five coordinated with a distorted square pyramidal environment. Four carboxylate-oxygen atoms from two crystallographically independent malonate groups build the equatorial plane around the copper atom. A water molecule occupies the apical position.

3.4 Results and Discussion:

3.4.1 EPR studies:

For a vanadyl impurity, along a crystallographic axis, an eight line pattern is observed since the electron spin is 1/2 and ^{51}V nuclear spin is 7/2. In order to obtain spin Hamiltonian parameters at room temperature, single crystal rotations were performed along the three mutually orthogonal axes a*, b and c*, where axis b is the crystallographic axis b, axis a* is orthogonal to axis b in ab plane and axis c* is mutually perpendicular to both the axes b and a*. Crystals with 0.5, 1.0 and 1.5 % concentrations of dopant ion gave resonances that are relatively weak and hence difficult to follow during crystal rotations. However, in case of crystals with dopant ion concentration of 5.0 %, the resonances are relatively broad. Hence, the higher concentration 5.0 % is used for XRD, IR and UV-Vis studies. Hence, in the present EPR investigation, crystals with 2.0 % concentration are used for single crystal EPR analysis. An EPR spectrum, when the applied magnetic field (B) is parallel to axis c* is shown in Fig. 3.1. Here, one can notice eight strong lines marked by 1-8, indicating that the ion under study is VO(II). However, additional resonance lines of relatively lower intensity, are also seen, corresponding to other VO(II) sites in the lattice. As mentioned later, these lines could not be followed during crystal rotations, due to their lower intensity. Another EPR spectrum, recorded in a*c* plane, when B is 40^o away from axis c* is given in Fig. 3.2. In this figure, the eight resonances corresponding to the higher intensity site which have been taken to calculate spin Hamiltonian parameters g and A. Another EPR spectrum, when B is parallel to axis a* is shown in Fig. 3.3, which corresponds to the minimum spread. From the spectra obtained in the three orthogonal planes, isofrequency plots were plotted in the three orthogonal planes and are given in Figs. 3.4, 3.5 and 3.6 for a*c*, bc* and a*b planes respectively. These plots are on expected lines. In all these plots, the g minima and A minima are occurring at the same angle indicating that these two tensors are coincident.

3.4.1.1 Calculation of spin-Hamiltonian parameters:

The spectra obtained in the three orthogonal planes for VO(II) ion are fitted with the following spin-Hamiltonian using the program EPR – NMR [21]

$$\hat{H} = \beta(g_x B_x S_x + g_y B_y S_y + g_z B_z S_z) + A_x S_x I_x + A_y S_y I_y + A_z S_z I_z \qquad (3.1)$$

The g and A matrices thus calculated are given in Table 3.1, along with the principal values and direction cosines. It is clear from the Table 3.1 that the direction cosines of the principal values of g and A are nearly coincident. The system shows rhombic symmetry, more so in g values. This point is also clear from isofrequency plot in a*b plane. In general, if a paramagnetic system exhibits axial symmetry, the isofrequency plots in a*c* and bc* planes

will be identical, whereas the resonance lines in a*b plane show invariance. On the other hand, a slight deviation from axial symmetry makes the resonance lines in a*b plane show angular dependence. In the present system, the isofrquency plot in a*b plane is angle dependent and isofrequency plots in a*c* and bc* planes are not identical. Using these g and A matrices, the angular variation plots are simulated and are also given in Figs. 3.4, 3.5 and 3.6 respectively, where a good agreement is noticed. In all these figures, the solid lines indicate the theoretical values and the solid circles indicate the experimental values.

3.4.1.2 Orientation of impurity:

The direction cosine of Zn – O bonds in ALMZ lattice are given in Table 3.2. These are helpful to predict the location of the paramagnetic impurity. If the direction cosines of principal value of g_{zz} match with any one of the direction cosines of Zn – O bonds, one can assume that the dopant has entered the lattice substitutionally. Otherwise, an interstitial location is expected for the paramagnetic impurity. A close look at the direction cosines given in Tables 3.1 and 3.2 indicate that none of them matches with each other. In other words, one can suggest that the vanadyl ion might have entered the lattice in an interstitial location. In addition, the unit cell contains two molecules and in all the three planes, only one site is noticed during crystal rotations. This also suggests that the impurity has not entered substitutionally.

3.4.1.3 Polycrystalline EPR studies:

The EPR spectrum of the powder sample of VO(II)/ALMZ, recorded at room temperature, is given in Fig. 3.7. The spin Hamiltonian parameters calculated from the powder spectrum are also given in Table 3.1. The agreement between these values and the values obtained from single crystal analysis is relatively good. However, g_{xx}/g_{yy} and A_{xx}/A_{yy} are not resolved in powder spectrum due to the closeness in their values. This kind of observation is very common in VO(II) impurities. Using these parameters, the powder spectrum has been simulated and is also given in Fig. 3.7. The principal values of the spin-Hamiltonian parameters of VO(II) ion in ALMZ are tabulated with similar lattices in Table 3.3.

An octahedral complex with a tetragonal compression would give $g_{\parallel} < g_{\perp} < g_e$ and $|A_{\parallel}| > |A_{\perp}|$, [26, 27]. The value of $\Delta g_{\parallel}/\Delta g_{\perp}$ gives the tetragonality of VO(II) site where $\Delta g_{\parallel}$ and $\Delta g_{\perp}$ are deviation of $g_{\parallel}$ and $g_{\perp}$ from the free electron value, g_e (2.0023). In the present work, the value of $\Delta g_{\parallel}/\Delta g_{\perp}$ is greater than unity, indicating that the VO(II) ions are tetragonally distorted. The distortion takes place along V=O direction and the ground state of vanadium splits into d_{xy}, d_{xz} and d_{yz} states.

3.4.1.4 Admixture coefficients:

The admixture coefficients are calculated from the spin-Hamiltonian parameters. The single unpaired electron on the metal ion occupies d_{xy} or d_{xz} or d_{yz} orbital in an octahedral configuration. Upon lowering the symmetry, the ground state d_{xy} can mix with $d_{x^2-y^2}$, d_{yz} and d_{xz}. The admixture coefficients C_1, C_2 and C_3 are related to the spin-Hamiltonian parameters by the relations [28]

$$g_{\parallel} = 2\left(3C_1^2 - C_2^2 - 2C_3^2\right) \tag{3.2}$$

$$g_{\perp} = 4C_1\left(C_2 - C_3\right) \tag{3.3}$$

The equations (3.2) and (3.3) along with the normalization condition $\left(C_1^2 + C_2^2 + C_3^2 = 1\right)$ can be solved iteratively to obtain the admixture coefficients. The values of C_1, C_2, and C_3 obtained are given in Table 3.4, along with few literature values.

3.4.2 Optical absorption studies:

The optical absorption spectrum of VO(II) doped in ALMZ at room temperature is shown in Fig. 3.8. The spectrum consists of three absorption bands at 327 nm (30,581 cm^{-1}), 575 nm (17,391 cm^{-1}) and 700 nm (14,285 cm^{-1}) respectively. VO(II) ion with d^1 configuration has ^2D ground state. In octahedral crystal field, the ^2D state splits into $^2T_{2g}$ and ^2E_g, while an octahedral field with tetragonal distortion further splits the $^2T_{2g}$ level into ^2E_g and $^2B_{2g}$, and ^2E_g level splits into $^2A_{1g}$ and $^2B_{1g}$. Among these levels, B_{2g} will be the ground state. Thus, for VO(II), two bands are expected corresponding to the transitions $^2B_{2g} \rightarrow {}^2E_{2g}$ and $^2B_{2g} \rightarrow {}^2B_{1g}$. These two bands can be assigned to $\Delta\perp = {}^2B_{2g} \rightarrow {}^2E_{2g}$ ($Ed_{xy} \rightarrow d_{xz,}\, d_{yz}$) and $\Delta_{\parallel} = {}^2B_{2g} \rightarrow {}^2B_{1g}$ ($Ed_{xy} \rightarrow d_{x^2-y^2}$) transitions respectively. Except for the high – energy band at 30,581 cm^{-1}, all other bands are attributed as d-d transitions. The band at 30,581 cm^{-1} is due to charge transfer, arising from the promotion of electron from the filled bonding level (oxygen orbital) e_{π}^{b} to nonbonding level b_2 and is assigned to the transition $e_{\pi}^{b} \rightarrow {}^2B_{2g}$ (b_2) (from filled level to d_{xy} level) [32].

Both EPR and optical data can be used to calculate the molecular orbital coefficients by using following equations [33, 34]

$$g_{\parallel} = g_e\left[1 - \frac{4\lambda\beta_1^2\beta_2^2}{\Delta\parallel}\right], \tag{3.4}$$

$$g_{\perp} = g_e\left[1 - \frac{\lambda\gamma^2\beta_2^2}{\Delta_{\perp}}\right], \tag{3.5}$$

Here g_e is free electron g value equal to 2.0023 and λ is the free ion value of the spin-orbit coupling constant of VO(II) ion (170 cm^{-1} [35]). β_1^2, β_2^2 and γ^2 are the molecular orbital coefficients of the d^1 electron. These molecular orbital coefficients (also called bonding coefficients) thus characterize in-plane σ bonding, in-plane π bonding and out-of-plane π bonding, respectively.

The parallel and perpendicular components of hyperfine interaction $A_\parallel$ and $A_\perp$ are related to the molecular orbital coefficients by the following expressions [36],

$$A_\parallel = -P[\kappa - 4/7\,\beta_2^2 - (g_e - g_\parallel) - 3/7(g_e - g_\perp)] \quad (3.6)$$

$$A_\perp = -P[\kappa - 2/7\,\beta_2^2 - 11/14\,(g_e - g_\perp)] \quad (3.7)$$

The degrees of distortion can be estimated from the Fermi contact term κ and the P parameter, which are related to radial distribution of wave function of the ions given as $P = g_e g_N \beta_e \beta_N (r^{-3})$. Here, β_2^2 is the covalency ratio of V=O bonds. The parameter P is related to the isotropic hyperfine coupling and represents the amount of unpaired electron density at the nucleus.

Neglecting the second order effects and taking negative values for $A_\parallel$ and $A_\perp$, P value is calculated from Eq. (3.8) [37] and the results are given in Table 3.4.

$$P = 7(A_\parallel - A_\perp) / 6 + (3/2)(\lambda/\Delta_\parallel) \quad (3.8)$$

The Fermi contact parameter (κ) is calculated by using the equation

$$\kappa = - A_{iso} / P - (g_e - g_{iso}) \quad (3.9)$$

Here, A_{iso} and g_{iso} are calculated from the powder A and g values respectively. Combine Eqs. (3.6) and (3.7) and eliminating κ, one can get an expression for β_2^2 in terms of the principal values of the g and A tensors,

$$\beta_2^2 = (-7/6)[(A_\parallel - A_\perp)/P + (g_e - g_\parallel) - (5/14)(g_e - g_\perp)] \quad (3.10)$$

The calculated parameters are given in Table 3.5. The deviation of β_1^2 from unity usually represents the degree of the admixture of the ligand orbitals and increase in the degree of covalency. β_2^2, found in this work, clearly indicates that the bonding is nearly ionic and represents poor π bonding of the ligands. If $\beta_1^2 = 1$, the bond would be completely ionic. If $\beta_1^2 = 0.5$, the bond would be completely covalent. The parameters $1 - \beta_1^2$ and $1 - \gamma^2$ are the measures of the covalency. First term gives an indication of the influence of σ bonding between vanadium atom and equatorial ligands, second indicates the influence of π bonding between the vanadium ion and the vanadyl oxygen.

3.4.3 FT-IR spectral studies:

Fourier transform infrared spectroscopy is employed to identify the nature of the bonding between various atoms, the stretching and bending vibrations is generally observed. The FTIR spectra of pure and VO(II) doped ALMZ at room temperature are shown in Fig. 3.9. Observed FTIR bands and their tentative assignments [38] for pure ALMZ and VO(II) doped ALMZ are tabulated in Table 3.6.

3.4.4 Powder XRD studies:

Powder XRD pattern of VO(II) doped ALMZ at room temperature is shown in Fig. 3.10. The powder XRD is used to identify and characterize the powder sample, in the crystalline materials. According to powder XRD measurements, the VO(II) doped ALMZ powder sample has identical lattice parameters as the pure ALMZ powder sample. The lattice parameters are tabulated in Table 3.7 with the single crystal XRD parameter of ALMC [20]. It is clear from the table that the parameters of pure ALMZ and VO(II) doped ALMZ matched with reported values of copper complex [20], indicating that the zinc and copper complexes are isomorphic and the low dopant concentration of VO(II) ion in ALMZ does not alter the structure and symmetry of the host lattice.

3.5 Conclusion:

Single crystal vanadyl ion doped ALMZ has been studied at room temperature using EPR spectroscopy. The results indicate more than one site in the lattice and the number of sites seems to be independent of concentration of the impurity. The spin Hamiltonian parameters indicate that the impurity is axially distorted and entered the lattice in an interstitial position. The isofrequency plots and the powder EPR spectrum have been simulated, which authenticates evaluated spin Hamiltonian parameters. The optical absorption spectrum at room temperature shows three bands characteristic of vanadyl ions in distorted octahedral symmetry. Admixture coefficients, molecular orbital coefficients, Fermi contact term and dipolar interaction parameter have also been calculated. FTIR and XRD studies confirm the formation and structure of the complex.

References:

[1] I. Sougandi, R. Venkatesan, T.M. Rajendran, P. Sambasiva Rao, Phy. Scripta, 67 (2003) 53.

[2] Ram Kripal, Manju Maurya, Solid State Commn., 150 (2010) 95.

[3] I. Sougandi, R. Venkatesan, P. Sambasiva Rao, J. Phys. Chem. Solids, 64 (2003) 1231.

[4] R. Tapramaz, B. Karabulut, F. Koksal, J. Phys. Chem. Solids, 61 (2000) 1367.

[5] C. Shiyamala, S. Mithira, P. Sambasiva Rao, J. Phys. Chem. Solids, 69 (2008) 2773.

[6] B. Karabulut, A. Tufan, Spectrochim. Acta, A65 (2006) 285.

[7] E. Bozkurt, B. Karabulut, I. Kartal, Y.S. Bozkurt, Che. Phys. Lett. 477 (2009) 65.

[8] I. Ucar, Spectrochim. Acta, A72 (2009) 399.

[9] B. Deva Prasad Raju, K.V. Narasimhulu, N.O. Gopal, J. Lakshmana Rao, J. Phys. Chem. Solids, 64 (2003) 1339.

[10] Ram Kripal, Indrajeet Mishra, S.K. Gupta, Manju Arora, Spectrochim. Acta, A71 (2009) 1969.

[11] C. Ruiz-Perez, Y. Rodriguez-Martin, M. Hernandez-Molina, F.S. Delgado, J. Pasan, J. Sanchiz, F. Lloret, M. Julve, Polyhedron, 22 (2003) 2111.

[12] J. Pasan, F.S. Delgado, Y. Rodriguez-Martin, M. Hernandez-Molina, C. Ruiz-Perez, J. Sanchiz, F. Lloret, M. Julve, Polyhedron, 22 (2003) 2143.

[13] C. Oldham, G. Wilkinson, R.D. Gillard, J.A. McCleverty (Eds.), "Comprehensive Coordination Chemistry", vol. 2, Pergamon Press, Oxford, 1987, 435.

[14] D.K. Towle, S.K. Hoffmann, W.E. Hatfield, P. Singh, P.Chaudhuri, Inorg. Chem., 27 (1988) 394.

[15] P.R. Levstein, R. Calvo, Inorg. Chem., 29 (1990) 1581.

[16] F. Sapin˜ a, E. Escriva´, J.V. Folgado, A. Beltra´n, A. Fuertes, M. Drillon, Inorg. Chem., 31 (1992) 3851.

[17] E. Colacio, J.P. Costes, R. Kiveka¨s, J.P. Laurent, J. Ruiz, Inorg. Chem., 29 (1990) 4240.

[18] E. Colacio, J.M. Domı´nguez-Vera, J.P. Costes, R. Kiveka's, J.P. Laurent, J. Ruiz, M. Sundberg, Inorg. Chem., 31 (1992) 774.

[19] E. Colacio, J.-M. Dominguez-Vera, R. Kivekäs, J.M. Moreno, A. Romerosa, J. Ruiz. Inorg. Chim. Acta, 212 (1993) 115.

[20] F.S. Delgado, C. Ruiz, J. Sanchiz, F. Lloret, M. Julve, Cryst. Eng. Comm., 8 (2006) 507.

[21] EPR-NMR Program devoleped by F. Clark, R.S. Dickson, B.D. Fulton, J. Isoya, A. Lent, D.G. McGavin, M.J. Mombourquette, R.H.D. Nuttall, P.S. Rao, H. Rinnerberg, W.C. Tennant, J.A. Well, University of Saskatchewan, Saskatoon, Canada, 1996.

[22] B. Natarajan, S. Mithira, S. Deepa, R.V.S.S.N. Ravikumar, P. Sambasiva Rao, Radiat. Eff. Defects Solids, 61 (2006) 177.

[23] B. Natarajan, S. Mithira, S. Deepa, R.V.S.S.N. Ravikumar, P. Sambasiva Rao, J. Phys. Chem. Solids. 68 (2007) 1995.

[24] I. Siegel, Phys. Rev., A193 (1964) 134.

[25] R.M. Golding, Mol. Phys., 5 (1962) 369.

[26] A. Abragam, B. Bleaney, "Electron Paramagnetic Resonance of Transition Ions", Clarendon, Oxford, 1970.

[27] A. Murali, J.L. Rao, A.V. Subbaiah, J. Alloys Compd., 257 (1997) 96.

[28] V.P. Seth, S.K. Yadav, V.K. Jain, Pramana, J. Phys., 21 (1983) 65.

[29] H. Anandalakshmi, T.M. Rajendiran, R. Venkatesan, P. Sambasiva Rao, Spectrochim. Acta, A56 (2000) 2617.

[30] R. Poonguzhali, R. Venkatesan, T.M. Rajendiran, P. Sambasiva Rao, R.V.S.S.N. Ravikumar, Y.P. Reddy, Cryst. Res. Technol., 35 (2000) 1203.

[31] K. Velavan, I. Sougandi, R. Venkatesan, P. Sambasiva Rao, J. Phys. Chem. Solids, 66 (2005) 15.

[32] A.B.P. Lever, "Inorganic Electronic Spectroscopy", 2nd Ed., Elsevier, New York, 1986.

[33] V.P. Seth, S. Gupta, A. Jindal, S.K. Gupta, J. Non-Cryst. Solids, 162 (1993) 263.

[34] R. Muncaster, S. Parke, J. Non-Cryst., 24 (1977) 399.

[35] C.J. Ballhausen, H.B. Gray B, Inorg. Chem., 1 (1961) 111.

[36] D. Pathinettam Padiyan, C. Muthukrishnan, R. Murugesan, J. Mol. Struct., 648 (2003) 1.

[37] U.B. Gangadharmath, S.M. Annigeri, A.D. Naik, V.K. Revankar, V.B. Mahale, J. Mol. Struct., 572 (2000) 61.

[38] K. Nakamoto, P.J. McCarthy, A. Ruby, A.E. Martell, J. Am. Chem. Soc., 83 (1961) 1066.

SPIN-LATTICE RELAXATION MEASUREMENTS AND STRUCTURAL INVESTIGATION OF VO(II) ION DOPED IN A PARAMAGNETIC HOST BY EPR STUDY

4.1 Introduction:

Electron Paramagnetic Resonance (EPR) studies provide a great deal of information about the magnetic properties of paramagnetic ion in different host lattices. They also lead to understanding of the nature of the bonding of the metal ion with its ligands. The EPR studies of paramagnetic ion doped in diamagnetic host gives valuable information about the magnetic properties of matter, chemical bonding, dynamic interactions of spins with lattice, nuclear moments, the possibility of nuclear alignment and orientational properties of the host lattice [1-3]. The observed resonances are sharp, due to the absence of dipole – dipole broadening. Alternatively, it is necessary in a few cases, to dope a paramagnetic impurity into a paramagnetic host lattice. In this situation, the dipole-dipole interaction between the two paramagnetic centres will help to estimate relaxation times. However, reasonably sharp EPR lines are seen even in paramagnetic lattice [4-8], if the paramagnetic host does not show its characteristic EPR spectra at room temperature, but provide resonances only at low temperature.

Vanadium is one of the transition group elements that has been studied with EPR spectroscopy in divalent, trivalent and tetravalent states. The tetravalent state, V(IV) exists as VO(II) ion with a single unpaired d-electron. The $3d^1$ configuration of vanadyl ion allows electron paramagnetic resonance to be observed at ambient temperatures [9-11]. The behaviour of vanadyl complex is dictated by the strong V=O bonding and most of the complexes possess C_{4v} symmetry. EPR studies of VO(II) ion in a variety of host lattices have been reported [12-19]. However, in a recent work [20], both substitutional and interstitial sites for VO(II) impurity are reported. Therefore, interest is developed to ensure the location of the impurity ion and nature of bonding in Triaquapotassiumbismalonatonickelate single crystal. Triaquapotassiumbismalonatonickelate is abbreviated here as PBMN. In this chapter, the EPR and optical absorption studies of VO(II) ion doped single crystal PBMN are discussed. These studies deduce the spin Hamiltonian parameters, spin-lattice relaxation time and molecular orbital (MO) coefficients, which are further used to discuss the nature of bonding of VO(II) ion with ligand atoms in the crystal.

4.2 Materials and Methods:

4.2.1. Preparation of single crystal of VO(II)-doped $[K(H_2O)_{3/2}]_2[Ni(mal)_2]$:

Malonic acid, nickel(II) basic carbonate, potassium hydrogen carbonate were purchased from commercial sources and used as received. $[K(H_2O)_{3/2}]_2[Ni(mal)_2]$ was synthesized by adding solid nickel(II) basic carbonate to an aqueous solution of malonic acid under continuous stirring. The suspension was heated at 40 – 50° C, until a colourless solution was obtained. This solution was filtered and mixed with an aqueous solution of potassium hydrogen carbonate. The solution was then filtered and doped with five different concentrations of vanadyl sulfate (0.5, 1.0, 1.5, 2.0 and 5.0 %). All the crystals were transparent and blue colour with well shaped and separated out on concentrating the solution at room temperature.

4.2.2 EPR Measurements:

The EPR spectra are recorded at 300 K on a JEOL JES-TE100 ESR spectrometer operating at X-band frequencies, having a 100 kHz field modulation to obtain the first-derivative EPR spectrum. 1,1-Diphenyl-2-picrylhydrazyl (DPPH) with a g-value of 2.0036 is used as a reference for g-factor calculations.

4.2.3 UV-Visible, FT-IR, Powder XRD Measurements:

The optical spectrum has been recorded at room temperature using a Varian Cary 5000 ultraviolet-visible (UV-Vis) near-infrared spectrophotometer in the range of 200-1300 nm. In the present investigation, the FT-IR spectra are recorded for doped and undoped materials on a Shimadzu FT-IR-8300/8700 spectrometer, in the frequency range of 4000-400 cm^{-1}. The measurements are made using almost transparent KBr pellets containing fine-powdered samples at room temperature. In the current study, powder XRD studies are carried out for doped and undoped materials on a PANalytical X'pert PRO diffractometer with Cu Kα radiation of wavelength λ = 0.15406 nm, 2θ values between 5-75°, at room temperature.

4.3 Crystal structure:

PBMN, $[K(H_2O)_{3/2}]_2[Ni(mal)_2]$ is isostructural with $[K(H_2O)_{3/2}]_2[Cu(mal)_2]$ [21]. It belongs to orthorhombic crystal system with space group Pbcn, having unit cell parameters a = 0.7398 nm, b = 1.8830 nm, c = 0.9320 nm, $\alpha = \beta = \gamma = 90°$, and Z = 4. Each copper atom is six coordinated and exhibit a 4+2 elongated octahedron environment. Four carboxylate-oxygen atoms from two bidentate malonate ligands define the equatorial plane around the

copper atom. Apical positions are occupied by two symmetry related carboxylated-oxygen atoms from other two monodentate malonate ligands.

4.4. Results and Discussions:

4.4.1 EPR Studies:

The EPR studies on the single crystal doped with diluted paramagnetic impurity provided interesting results. As the crystals were grown with five different concentrations, crystals with 0.5, 1.0 and 1.5 % concentration of dopant show weak lines; whereas crystal with 5.0 % gave relatively broad lines. Hence, in all the further EPR measurements, crystals with concentration of 2.0 % dopant are used. However, 5.0 % concentration samples are used for powder XRD, IR and optical measurements. A good, well-shaped single crystal of optimum size has been chosen to rotate in three orthogonal axes namely a, b and c. Generally one could expect eight lines for a vanadyl ion due to the interaction of electronic spin (S = 1/2) with the nuclear spin (I = 7/2). During the crystal rotations in the three orthogonal planes namely ab, bc and ac, a maximum of eight lines are only noticed in each plane. This indicates the presence of only one type of the impurity in the crystal. An EPR spectrum of VO(II) doped in PBMN, when the applied external magnetic field (B) is 50º away from the crystallographic axis a is given in Fig. 4.1. Fig. 4.2 is showing the EPR spectrum of VO(II)/PBMN recorded in ac plane, when B is 140º away from the axis c, corresponding to maximum hyperfine separation. Fig. 4.3 corresponds to an EPR spectrum of VO(II)/PBMN when B is parallel to axis c. In single crystal of PBMN doped with VO(II), reasonably sharp EPR lines are observed in all the three crystallographic planes except in few orientations which are having dipole broadening due to the paramagnetic host–impurity interaction. However, the line width of the hyperfine lines of PBMN is found to be slightly larger than those found in the corresponding diamagnetic lattice. This is due to the presence of the Ni(II) ion. Crystal rotations are done in all the three planes to calculate the spin Hamiltonian parameters (g and A matrices) from the isofrequency plots.

4.4.1.1 Calculation of spin-Hamiltonian parameters:

In order to obtain spin Hamiltonian parameters, single crystal EPR spectra, recorded in the three orthogonal planes for VO(II) ion, are fitted with the following spin Hamiltonian .

$$\hat{H} = \beta(g_x B_x S_x + g_y B_y S_y + g_z B_z S_z) + A_x S_x I_x + A_y S_y I_y + A_z S_z I_z \qquad (4.1)$$

The spin Hamiltonian parameters (g and A matrices), calculated using the program EPR-NMR [22] are given in Table 4.1, along with the direction cosines. The direction cosines of the principal g and A are nearly coincident. Hence the maxima and minima of g and A

variation are obtained at the same angle. For comparison, the direction cosines of Ni–O bonds in PBMN are given in Table 4.2. These are helpful to predict the location of the paramagnetic impurity. If the direction cosines of principal value of g match with any one of the direction cosines of Ni–O bonds, a substitution location can be suggested. Otherwise, the impurity might have entered an interstitial location. A close look at the direction cosines given in Tables 4.1 and 4.2 indicate that none of them matches well with each other. In other words, one can suggest that the vanadyl ion might have entered the lattice in an interstitial location. The spin Hamiltonian values agree well with the literature values, a few of which are summarized in Table 4.3. Using the g and A matrices, the angular variation plots are simulated and it is found to fit with the experimental values. In general, if a paramagnetic system exhibits axial symmetry, the isofrequency plots in ac and bc planes will be identical, whereas the resonance lines in ab plane show invariance. Most of the systems studied so far for VO(II) fall under this category. On the other hand, a slight deviation from axial symmetry makes the resonance lines in ab plane show angular dependence. In the present system, the isofrquency plot in ab plane is angle dependent and isofrequency plots in ac and bc planes are almost identical. This immediately confirms that the impurity has nearly axial symmetry. In all the isofrequency plots, Figs. 4.4 – 4.6, the solid lines indicate the theoretical values and the solid circles indicate the experimental values. A good agreement is obtained.

4.4.1.2 Polycrystalline studies:

To confirm the single crystal analysis, powder EPR spectrum, recorded at room temperature, is given in Fig. 4.7. It clearly indicates eight parallel and eight perpendicular features, typical of vanadyl impurity in axially symmetric form. The spin Hamiltonian parameters calculated from the powder spectrum are also given in Table 4.1. The agreement between the powder data and single crystal data is good. However, g_{xx}/g_{yy} and A_{xx}/A_{yy} are not resolved in powder spectrum due to the closeness in their values. This type of observation is very common in VO(II) ion impurity. The powder spectrum is simulated using the program SimFonia and is also given in Fig. 4.7 itself. The agreement is good, further confirming the values which are calculated from single crystal analysis.

4.4.1.3 Admixture coefficients:

We have also calculated the admixture coefficients from the spin Hamiltonian parameters. The single unpaired electron on the metal ion occupies d_{xy} or d_{xz} or d_{yz} orbital in an octahedral configuration. Upon lowering of symmetry, the ground state d_{xy}, when acted upon by spin-orbit term can mix with $d_{x^2-y^2}$, d_{yz} and d_{xz}. If C_1, C_2 and C_3 are the admixture

coefficients, where the ground state d_{xy} can mix with d_x^2-$_y^2$, d_{yz} and d_{xz} these are related to the spin-Hamiltonian parameters by the relations [25]

$$g_{\parallel} = 2\left(3C_1^2 - C_2^2 - 2C_3^2\right) \quad (4.2)$$

$$g_{\perp} = 4C_1\left(C_2 - C_3\right) \quad (4.3)$$

These equations along with the normalization condition $\left(C_1^2 + C_2^2 + C_3^2 = 1\right)$ can be solved iteratively to obtain the admixture coefficients. The values thus obtained are given in Table 4.4, along with the data obtained for other systems. Using these coefficients and spin Hamiltonian parameters, two more parameters κ (a dimensionless constant describing core s-polarisation) and P have also been calculated using the equations (4.4) and (4.5) [28]

$$A_{\parallel} = P[g_{\parallel} - (\kappa + (15/7)(1 - 2C_3^2) - (3/7)(1 + C_1C_2C_3)] \quad (4.4)$$

$$A_{\perp} = P[(11/14)\ g_{\perp} - 2C_1C_2(\kappa + (9/7)] \quad (4.5)$$

and these values are also given in Table 4.4.

4.4.1.4 Evaluation of MO coefficients:

The spin-Hamiltonian parameters are related to the molecular orbital coefficients by the expressions [29]

$$g_{\parallel} = g_e - 8\beta_1^2\ \beta_2^2\ \lambda/(\Delta E_1(b_2 - b_1^*) \quad (4.6)$$

$$g_{\perp} = g_e - (2\lambda\beta_1^2\ e_{\pi}^2/\Delta E_2(b_2 - e_{\pi}^*) \quad (4.7)$$

$$A_{\parallel} = -p\kappa - (4/7)\beta_2^2\ p - (g_e - g_{\parallel})P - (3/7)(g_e - g_{\parallel})P \quad (4.8)$$

$$A_{\perp} = -p\kappa + (2/7)\beta_2^2\ p - (11/14)(g_e - g_{\perp})P \quad (4.9)$$

where β_1^2, β_2^2 and e_{π}^2 are molecular orbital coefficients. The isotropic EPR parameters are calculated by using the relations

$$g_0 = (1/3)(g_{\parallel} + 2g_{\perp}) \quad (4.10)$$

$$A_0 = (1/3)(A_{\parallel} + 2A_{\perp}) \quad (4.11)$$

Combining the above relations with the expressions (4.8) and (4.9), we get

$$A_0 = -p\kappa - (g_e - g_0)P \quad (4.12)$$

Using the above equation, the Fermi contact term is calculated. The Fermi contact term is directly related to the isotropic hyperfine coupling and represents the amount of unpaired electron density at the nucleus [30]. Combining Eq. (4.8) and (4.9) and eliminating κ, one can get an expression for β_2^2 in the form of g and A tensor values.

$$\beta_2^2 = (-7/6)[(A_{\parallel} - A_{\perp})/P + (g_e - g_{\parallel}) - (5/14)(g_e - g_{\perp})] \quad (4.13)$$

Using the above relation β_2^2 is calculated. The deviation of β_2^2 from unity usually represents the degree of admixture of the ligand orbital and increase in the degree of covalency. The present value of β_2^2 = 0.93 clearly indicates that the bonding is nearly ionic and represents poor π bonding of the ligands. The β_2^2 should be equal to unity for a nonbonding orbital in the case of pure $[VO(H_2O)_5]^{2+}$ complex [31].

β_1^2 indicates the delocalisation in the σ system. The in-plane σ bonding varies from compound to compound and decreases from unity as the covalency of the bond increases. From Eq. (4.6), the value of β_1^2 is calculated and found to be 0.94. β_1^2 values reported in different hosts are collected in Table 4.5 and are compared with the present value. Considerable contribution of 4s spin density to κ is predicted from the value of β_1^2. The out-of-plane π bonding represented by e_π^2, calculated from Eq. (4.7), is 0.89, which is comparable with many other systems.

4.4.1.5 Spin – lattice relaxation times:

To study the nature and extent of dipole interaction of the paramagnetic ion is interesting when it is incorporated in a paramagnetic host. At room temperature, the Ni(II) is EPR silent and this helps us to successfully analyze the data at this temperature. A change in the line width is noticed as the temperature is decreased from 300 K to 148 K. A few powder spectra of VO(II) ion doped in PBMN are given in Fig. 4.8. Hence, this change in line width during cooling of the sample can be ascribed to the influence of the paramagnetic host. In other words, this is due to the dipole-dipole interaction between the paramagnetic impurity VO(II) and the paramagnetic host Ni(II). As the temperature is reduced, the nickel ion becomes EPR active at low temperature and dipole-dipole interaction between nickel and vanadyl ion is increased, thus causing broadness in resonances of VO(II) ion. The line-width variation of VO(II) hyperfine lines in paramagnetic lattice can be understood on the basis of host spin-lattice relaxation mechanism. The fast spin-lattice relaxation of the host ions can randomly modulate the dipolar interaction between the paramagnetic host and the impurity ions resulting in "Host spin-lattice relaxation narrowing" [34]. When the spin-lattice relaxation narrowing mechanism is effective, the host spin-lattice relaxation time (T_1) is given by [34]

$$T_1 = \frac{3}{7}\frac{h}{2g_h\beta}\frac{\Delta B_{imp}}{Bd_d^2} \qquad (4.14)$$

$$Bd_d^2 = 5.1(g_h\beta n)^2 S_h (S_h + 1)$$

where, g_h = the host g value

S_h = the effective host spin and it is taken to be 1/2

n = the number of host spins per unit volume which can be calculated from the crystallographic data of the crystal lattice (0.8423×10^{24}) and

ΔB_{imp} = the impurity line width.

The calculated spin-lattice relaxation times T_1 are plotted as a function of temperature and the graph indicates that as the temperature decreases the spin-lattice relaxation time T_1 increases, as shown in Fig. 4.9. The order of spin-lattice relaxation time obtained in our work is found to be agreeable with the values reported for Ni(II) host in literature [34]. The T_1 value varies from 0.11×10^{-12} s at 300 K to 0.20×10^{-12} s at 148 K. These relaxation times are so short and may be due to the dipole-dipole interaction of the host and the impurity, which corresponds to cross-relaxation mechanism.

4.4.2 Optical absorption studies:

The optical absorption spectrum of vanadyl ion doped PBMN powder sample recorded at room temperature is given in Fig. 4.10. The spectrum consists of three bands at 272, 382 and 689 nm respectively. The latter two peaks correspond to d–d transitions in vanadyl. The band at 689 nm corresponds to the transition $b_2 - e_\pi^*$ and the band at 382 nm is due to the transition $b_2 - b_1^*$ levels. The higher energy band at 272 nm can be assigned as charge transfer band due to the promotion of the electron from the filled bonding level (oxygen orbital) to the nonbonding orbital level [35].

4.4.2.1 Spin – orbit coupling:

EPR and optical absorption data are combined to calculate the spin orbit coupling constant (λ). For an electron in the d_{xy} ground state, neglecting the covalence effects, the g values related to the optical transitions are given by

$$g_\parallel = g_e - (8\lambda/\Delta E_1)(b_2 - b_1^*) \quad (4.15)$$

$$g_\perp = g_e - (2\lambda/\Delta E_2)(b_2 - e_\pi^*) \quad (4.16)$$

where g_e is the free electron g value of 2.0023. Here, one can take $g_\parallel = g_{zz}$ and $g_\perp = (g_{xx} + g_{yy})/2$. Using the above equations, the value of λ obtained is 115 cm^{-1}. The value of λ for free ion of the VO(II) ion is 170 cm^{-1} [36, 37]. Such a drastic reduction in the value of λ observed in the present study indicates the weak covalency of bonds in the vanadyl complex.

4.4.3 FT-IR spectral studies:

The FT-IR spectra of pure and VO(II) doped PBMN at room temperature are shown in Fig. 4.11. It shows the bands in the range 3600 – 2400, 2500 – 2000, 1750 – 1250, 1100 –

400 cm^{-1}. Observed FTIR bands and their tentative assignments for pure PBMN and VO(II) doped PBMN are tabulated in Table 4.6. Carboxylic acid shows broad and intense O–H stretching absorption in the region of 3400 – 2500 cm^{-1}. The bands observed at 3350 and 3250 cm^{-1} are due to the O–H bonding corresponding to water ligation [38]. The bands at 1690 and 1590 cm^{-1} are assigned to C=O and C=C stretching, respectively. The twin bands at 1400 and 1440 cm^{-1} are due to O–H bending vibration. The C–H bending vibrations are generally observed in the 1370 – 1220 cm^{-1} wavenumber region. The bands at 1370 and 1270 cm^{-1} have been assigned to C–H bending vibrations. The bands at 1180, 1110 and 987 cm^{-1} have been assigned to O–H out-of-plane deformation bands. The bands observed at 779, 737 and 698 cm^{-1} are attributed as out-of-plane C–H bending vibration. The bands at lower wave number region from 600 to 400 cm^{-1} are due to O–H deformation bands.

4.4.4 Powder XRD studies:

Powder XRD pattern of VO(II) doped PBMN at room temperature is shown in Fig. 4.12. According to powder XRD measurements [39], VO(II) doped PBMN powder sample has identical lattice parameters as PBMN powder sample, as expected from the low impurity concentration. The lattice parameters are tabulated in Table 4.7 with the single crystal XRD parameter of PBMC [21]. It is clear from the Table 4.7 that the parameters of PBMN and VO(II) doped PBMN matched with reported values of copper complex [21], confirming that the PBMN is isomorphic with PBMC and the low dopant concentration of VO(II) in PBMN does not alter the symmetry of host lattice.

4.5 Conclusion:

Single crystal vanadyl ion doped PBMN is studied at room temperature using EPR technique which indicates only one site in the lattice and the number of sites seems to be independent of concentration of the impurity. The spin Hamiltonian parameters indicate that the impurity is axially distorted and entered the lattice in an interstitial position. The angular variation plot and the powder EPR spectrum have been simulated, which authenticates evaluated spin Hamiltonian parameters. The spin lattice relaxation times measured as a function of temperature indicated a substantial change in their values. The optical absorption spectrum shows three bands characteristic of vanadyl ions in distorted octahedral symmetry. By using EPR and optical data, admixture coefficients, molecular orbital coefficients, Fermi contact term and dipolar interaction parameter have also been calculated. FTIR and XRD studies confirm the formation and structure of the complex.

References:

[1] R.S. Alger, "Electron Paramagnet Resonance: Techniques and Application", Wiley, New York, 1968.

[2] J.A. Weil, J.R. Bolton, and J.E. Wertz, "Electron Paramagnetic Resonance: Elementary Theory and Applications", John Wiley and Sons, New York, 1994.

[3] K.V. Narashimhulu, J. Lakshmana Rao, Spectrochim. Acta, A53 (1997) 2605.

[4] V. Somasekharm, P. Sivaprasad, K. Ramesh, Y.P. Reddy, Phys. Scr., 33 (1986) 169.

[5] N.O. Gopal, K.V. Narasimhulu, J. Lakshmana Rao, Physica B, 307 (2001) 117.

[6] V.K. Jain, J. Chem. Phys., 84, (1986) 1994.

[7] P. Chand, V.K. Jain, G.C. Upreti, Magn. Reson. Rev., 14, (1988) 49.

[8] S.K. Misra, J. Sun, X. Li, Physica B, 168 (1991) 170.

[9] S. Dhanuskodi, A.P. Jeyakumari, Spectrochim. Acta, A57 (2001) 971.

[10] S. Deepa, K. Velavan, I. Sougandi, R. Venkatesan, P.S. Rao, Spectrochim. Acta, A61 (2005) 2482.

[11] B. Karabulut, A. Tufan, Spectrochim. Acta, A65 (2006) 742.

[12] A.K. Viswanath, J. Chem. Phys., 67 (1977) 3744.

[13] B.P. Maurya, A. Punnoose, M. Umar, R.J. Singh, Solid State Commun., 89 (1994) 59.

[14] P.A.A. Mary, S. Dhanuskodi, Spectrochim. Acta, A57 (2001) 2345.

[15] B.D.P. Raju, K.V. Narasimhulu, N.O. Gopal, J.L. Rao, J. Phys. Chem. Solids, 64 (2003) 1339.

[16] R. Kripal, P. Singh, J. Mag. Magn. Mater., 307 (2006) 308.

[17] C. Shiyamala, S. Mithira, B. Natarajan, R.V.S.S.N. Ravikumar, P.S. Rao, Phys. Scr., 74 (2006) 549.

[18] B. Natarajan, S. Mithira, S. Deepa, R.V.S.S.N. Ravikumar, P.S. Rao, Radiat. Eff. Defects Solids, 161 (2006) 177.

[19] R. Kripal, M. Maurya, H. Govind, Physica B, 392 (2007) 281.

[20] H. Anandalakshmi, R. Venkatesan, T.M. Rajendiran, P.S. Rao, Spectrochim. Acta, A56 (2000) 2617.

[21] F.S. Delgado, C. Ruiz, J. Sanchiz, F. Lloret, M. Julve, Cryst. Eng. Comm., 8, (2006) 507.

[22] F. Clark, R.S. Dickson, O. B. Fulton, J. Isoya, A. Lent, D. G. Mc Gavin, M. J. Mombourquette, R. H. D. Nuttall, P. S. Rao, H. Rinnerberg, W.C. Tennant, J. A. Weil, EPR-NMR Program, University of Saskatchewan, Saskatoon, Canada, 1996.

[23] I. Sougandi, K. Velavan, R. Venkatesan, P. Sambasiva Rao, Phys. Stat. Sol., (b)241 (2004) 3014.

[24] E. Bozkurt, B. Karabulut, I. Kartal, Y.S. Bozkurt, Chem. Phys. Lett., 477 (2009) 65.

[25] V.P. Seth, S.K. Yadav, V.K. Jain, Pramana, J. Phys., 21 (1983) 65.

[26] I. Sougandi, R. Venkatesan, T.M. Rajendiran, P. Sambasiva Rao, Phy. Scr., 67 (2003) 153.

[27] C. Shiyamala, T.M. Rajendiran, R. Venkatesan, P. Sambasiva Rao, Cryst. Res. Technol., 37 (2002) 841.

[28] D. Pathinettam Padiyan, C. Muthukrishnan, R. Murugesan, J. Mol. Struct., 648 (2003) 1.

[29] A.H. Maki, B.R. McGarvey, J. Chem. Phys., 31 (1958) 35.

[30] A. Kasiviswanath, S. Radhakrishna, J. Phys. Chem. Solids, 52 (1991) 232.

[31] S.G. Sathyanarayana, V.G. Krishnan, G.S. Sastry, J. Chem. Phys., 65 (1976) 4181.

[32] R. Kripal, I. Mishra, S.K. Gupta , M. Arora, Spectrochim. Acta, A71 (2009) 1969.

[33] R. Kripal, I. Mishra, Spectrochim. Acta, A72 (2009) 538.

[34] T. Mitsuma, J. Phy. Soc. Jpn., 17 (1962) 128; S.K. Mishra, Magn. Reson. Rev., 12 (1987) 191; V.K. Jain, J. Mag. Reson., 64 (1985) 512.

[35] A.B.P. Lever, “Inorganic Electronic Spectroscopy”, 2nd Ed., Elsevier, New York, 1986.

[36] T.M. Dunn, Trans. Faraday Soc., 57 (1961) 1441.

[37] D. Kivelson, S.K. Lee, J. Chem. Phys., 41 (1964) 1896.

[38] K. Nakamoto, P.J. McCarthy, A. Ruby, A.E. Martell, J. Am. Chem. Soc., 83 (1961) 1066.

[39] B. D. Cullity, “Elements of X-ray Diffraction”, Addison Wesley, Massachusetts, USA, 1978.

EFFECT OF PARAMAGNETIC DOPING ON AN INORGANIC POLYMER TRIAQUADIPOTASSIUMBIS(MALONATO)ZINCATE: SPECTROSCOPIC INVESTIGATION

5.1 Introduction:

Electron Paramagnetic Resonance (EPR) of Mn(II) has been investigated widely in octahedral, tetrahedral and cubic environments [1-9], since Mn(II), being a d^5 ion, is sensitive to distortions from perfect octahedral or tetrahedral symmetries. Hence, it is used as a paramagnetic impurity to identify distortions, phase transitions, structural and dynamic aspects of crystalline state etc. [1-4, 10-15]. In general, the EPR spectrum of Mn(II) is rather complex due to 'fine-structure' and 'hyperfine-structure'. The former is due to the interaction of the free electron spins within themselves, where as the latter arises from the interaction of the free electron with the nuclear spin of ^{55}Mn nucleus. In the absence of an external magnetic field, the six spin states, known as Kramers' doublets, are labeled as $|\pm5/2\rangle$, $|\pm3/2\rangle$ and $|\pm1/2\rangle$. These are separated by 4D and 2D respectively, where D is zero-field splitting parameter. When an external magnetic field is applied, these spin states split further resulting in five EPR transitions with selection rule $\Delta M_s = \pm1$. In addition, each of these five lines split further into a sextet, due to the nuclear spin of ^{55}Mn (I = 5/2). Hence, a 30-line pattern is expected. On the other hand, in polycrystalline samples, only $|+1/2\rangle \leftrightarrow |-1/2\rangle$ transition is generally observed, since the other four transitions have large anisotropy [1]. If D is very small compared to hyperfine coupling constant (A), the 30 lines will be so closely packed that one could see only six lines. If D is very large, five bunches of resonance lines, each split into sextet are observed. During our studies of this impurity ion in various host lattices [8], the ion was found to occupy substitutional, interstitial or both, depending on the concentration of the ion and geometrical coordination. The importance of malonato ligand in treating malignant tumour when coordinated with platinum (United States Patent 4140707) was studied. Coordination polymer compounds containing malonic acid as a ligand have been studied due to their potential applications as materials in molecular electronics, catalysts, biologically active compounds, molecular-based magnetic materials, etc. [16, 17]. In addition, malonic acid acts as a ligand with various dentate abilities. Hence, the current study of Mn(II) doped in triaquadipotassium bismalonatozincate was carried out to ascertain number of sites, site symmetry, location (whether substitutional or interstitial), and also to predict the extent of distortion.

5.2 Materials and Method:

5.2.1 Preparation of single crystals of Mn(II)-doped $[K_2(H_2O)_{3/2}]_2[Zn(mal)_2]$:

Malonic acid, zinc(II) basic carbonate, potassium hydrogen carbonate were purchased from commercial sources and used as received. $[K_2(H_2O)_{3/2}]_2[Zn(mal)_2]$ was synthesized by adding solid zinc(II) basic carbonate to an aqueous solution of malonic acid under continuous stirring. Along with Zn(II), three different concentrations of manganese sulfate (0.5, 1.0, 1.5, 2.0 and 5.0 %) were also added. The suspension was heated at 40 – 50° C, until a colorless solution was obtained. This solution was filtered and mixed with an aqueous solution of potassium hydrogen carbonate. All the crystals were transparent and colorless with well shaped and separated out on concentrating the solution at room temperature. Triaquadipotassiumbismalonatozincate is abbreviated here as PBMZ.

5.2.2 EPR Measurements:

EPR spectra are recorded at 300 K on a JEOL JES TE100 ESR spectrometer operating at X-band frequencies, having a 100 kHz field modulation to obtain first-derivative EPR spectrum. 1,1-Diphenyl-2-picrylhydrazyl (DPPH) with a g-value of 2.0036 is used as a reference for g-factor calculations.

5.2.3 UV-Visible, FT-IR, Powder XRD Measurements:

Optical spectrum has been recorded at room temperature using a Varian Cary 5000 ultraviolet-visible (UV-Vis) near-infrared spectrophotometer in the range of 200-1300 nm. FT-IR spectra are recorded for doped and undoped materials on a Shimadzu FT-IR-8300/8700 spectrometer in the frequency range of 4000-400 cm^{-1}. The measurements are made using almost transparent KBr pellets containing fine-powdered samples at room temperature. Powder XRD studies are carried out for doped and undoped samples on a PANalytical X'pert PRO diffractometer with Cu Kα radiation of wavelength λ = 0.15406 nm, 2θ values between 5-75°, at room temperature.

5.3 Crystal structure:

PBMZ, $[K_2(H_2O)_3]_2[Zn(mal)_2]$, is isostructural with $[K_2(H_2O)_3]_2[Cu(mal)_2]$ [18]. It belongs to orthorhombic crystal system with space group Pbcn, having unit cell parameters a = 0.7398 nm, b = 1.8830 nm, c = 0.9320 nm, $\alpha = \beta = \gamma = 90°$, and Z = 4. Each copper/zinc atom is six coordinated and exhibits a 4+2 elongated octahedron environment. Four carboxylate-oxygen atoms from two bidentate malonate ligands define the equatorial plane around the metal atom. Apical positions are occupied by two symmetry related carboxylated-oxygen atoms from other two monodentate malonate ligands [18].

5.4 Results and discussion:

5.4.1 EPR studies:

Any system with a total electron spin of 5/2 will give just one EPR line in the absence of zero-field splitting. When D is not zero, a five set pattern of six components each, i.e., 30 line patterns, is expected. Due to second order effects, these sextets in each group are not equally spaced. As single crystals of Mn(II) with various concentrations are grown, the EPR spectra are recorded for all the samples. Among the five concentration 0.5, 1.0 and 1.5 % are gave very weak resonance lines, which are difficult to follow during crystal rotations. In case of crystals with 5.0 % dopant concentration, the lines are broad due to dipole-dipole interactions. Hence, in the present study, crystals with 2.0 % dopant concentration have been used for single crystal EPR studies, due to well resolved hyperfine resonance lines. However, for IR, optical and powder XRD studies, samples with 5.0 % concentration are used. In all the crystals with different dopant concentrations, the number of impurity sites remained the same indicating that dopant concentration has no effect on the number sites observed in EPR spectrum. A well shaped single crystal of optimum size is taken and crystal rotations are done along the three mutually perpendicular crystallographic axes, namely a, b and c. Single crystal EPR measurements of Mn(II) ion doped PBMZ at room temperature show a variety of complicated spectra. A typical EPR spectrum, when the applied magnetic field (B) is parallel to crystallographic axis c, is shown in Fig. 5.1. In this spectrum, the five fine structure transitions for site 1 are indicated. This 30 line spectrum is characteristic of a system with S = 5/2 and I = 5/2. Generally, whenever an impurity enters the lattice either substitutionally or interstitially, one would expect a 30 line pattern along any one of the crystallographic axes. In addition, a bunch of extra resonances are noticed in the middle of the spectrum, which corresponds to another site, i.e., site 2 with small D (see below), compared to main set of resonances. The transitions at high and low field regions of site 1 are well resolved at most of the orientations in the bc plane of rotation. However, the resonances corresponding to the transitions, $|\pm 3/2> \leftrightarrow |\pm 1/2>$ and $|+1/2> \leftrightarrow |-1/2>$ are overlapped with resonances corresponding to site 2, at few orientations. This kind of observation is noticed in other planes also. The expected intensity ratio of Mn(II) fine structure lines is 5:8:9:8:5. A look at the figure indicates a different situation (assuming a quintet with sextet in each).

Fig. 5.2 contains an EPR spectrum of Mn(II) doped PBMZ corresponding to the minimum spread of the spectrum in the ac plane, which roughly corresponds to the magic angle. This EPR spectrum is not symmetrical. Hence it may be suggested that E term, which

indicates deviation of D from axial symmetry, is non-zero. In addition, the central sextet in Fig. 5.1 shows abnormal intensity behaviour. The crystal rotations of Mn(II)/PBMZ are also performed in the other two planes namely ab and ac. An EPR spectrum in ab plane is given in Fig. 5.3. Iso frequency plots are drawn in all the three orthogonal planes ab, ac and bc respectively. An iso-frequency plot in the ac plane is given in Fig. 5.4. This road map clearly follows the expected pattern. When the angle between the crystallographic axis c and the magnetic field is zero, one can see a maximum spread corresponding to 8D, i.e., $4D(3\cos^2\theta - 1)$. As θ is varied, the term in bracket before D becomes zero, when $(3\cos^2\theta - 1) = 0$, i.e., at $\theta = 54^o\ 47'$. Later on, the term changes sign and becomes 4D, at $\theta = 90^o$. This pattern repeats from 90 to 180º. The iso-frequency plots in bc and ab planes are given in Figs. 5.5 and 5.6 respectively.

The isofrequency plot in ab plane should have invariant resonance line position, if $g_{xx} = g_{yy}$, $A_{xx} = A_{yy}$ and $D_{xx} = D_{yy}$. However, due to small variations in these parameters (see below), one can notice variation in these resonance lines also. In addition, these resonance lines will not cross over, as observed in Fig. 5.4. The road map in bc plane is similar to the road map obtained in ac plane except for a small change, due to the difference in the spin-Hamiltonian parameters reflecting the deviation from axial symmetry. In all the three iso-frequency plots, only the outer lines (|±5/2> to |±3/2>) are given for site 1 and site 2 indicated by solid circles for experimental values and solid lines for theoretical values and open circles and dotted lines corresponding to experimental and theoretical values respectively, for the sake of clarity. In these figures, the resonance lines due to |+1/2> to |-1/2> transition, which are independent of D, are not shown. From these iso-frequency plots, the spin-Hamiltonian parameters are calculated as mentioned below.

5.4.1.1 Calculation of spin-Hamiltonian parameters:

The spin-Hamiltonian for a spin sextet, including second order effects and zero-field term D is given by

$$H = \beta(g_{xx}B_xS_x + g_{yy}B_yS_y + g_{zz}B_zS_z) + (A_{xx}S_xI_x + A_{yy}S_yI_y + A_{zz}S_zI_z) + D[S_2^2 - \frac{1}{3}S(S+1)] + E(S_x^2 - S_y^2) \quad (5.1)$$

Here the first term represents the electron Zeeman interaction and the second and third terms represent the hyperfine interaction. The fourth and fifth terms correspond to the axial components of the zero-field splitting and deviation from axial symmetry respectively. As the system contains more than one center, the analysis has been done separately, using the program EPR-NMR [19]. The spin-Hamiltonian parameters, thus obtained from the analysis

are given in Table 5.1 for both the sites, along with the direction cosines. The direction cosines of metal – oxygen bonds have been calculated from the single crystal XRD data of the host lattice and are given in Table 5.2. A few set of spin-Hamiltonian parameters, taken from literature are given in Table 5.3, for comparison. A good agreement is noticed. As suggested earlier, deviation from axial symmetry is seen and the calculated E values are 8.6 mT and 2.2 mT for site 1 and 2 respectively.

Using the g and A values obtained from program EPR-NMR, iso-frequency plots in the three planes have been simulated and are also given in Figs. 5.4, 5.5 and 5.6 for both the sites respectively. In these figures, solid and dotted lines corresponds to theoretical variation for two sites. The solid and open circles correspond to the experimental data. A good agreement is observed in all the planes, confirming the accuracy of our calculated spin-Hamiltonian parameters.

5.4.1.2 Location of the impurity:

The location of the impurity can be detected by comparing the direction cosines of the principal values of g/A tensors with any of the metal-ligand bond directions (Zn-O). The direction cosines of g, A and D are tabulated in Table 5.1 and that of metal ligand bond direction of PBMZ crystal lattice are given in Table 5.2. It is evident from these tables that the direction cosines of the principal values of g and A tensors of sites 1 and 2 do not match with any Zn-O metal ligand bond directions. This suggests that both the Mn(II) ions have entered the lattice interstitially. This is also quite expected considering the arrangement of ligands around the metal ion.

5.4.1.3 Polycrystalline EPR spectrum:

In order to confirm the single crystal analysis, powder spectrum of the Mn(II)/PBMZ is recorded at room temperature and is given in Fig. 5.7. The powder spectrum is not symmetrical with respect to central portion (corresponding to |+1/2> to |-1/2> transition) indicating the deviation of spin Hamiltonian parameters from axial symmetry. The two sites noticed in single crystal analysis were not shown clearly in the powder spectrum, due to the overlap of second site with the first site. Here, it is to be noted that the spread of the spectrum depends on the relative values of D. The spin-Hamiltonian parameters (g, A and D) calculated from the powder spectrum is also given in Table 5.3.

5.4.1.4 Covalency of the metal-ligand bond:

The percentage of covalency of the Mn – O bond can be calculated from Matamura's plot [20, 21]. The covalency of a bond between manganese and its ligands depend on the magnitude of the isotropic hyperfine coupling constant *A* (average of the three *A* values). An

empirical relationship for the covalency c of a bond between the atoms *p* and *q* and their electro negativities χ_p and χ_q is given by

$$c = [1 - 0.16(\chi_p - \chi_q) - 0.035(\chi_p - \chi_q)^2]/n \quad (5.2)$$

Here, n is the number of ligands around Mn(II) ion. The percentage of covalency obtained is around 8, assuming χ_{Mn} = 1.4 and χ_O = 3.5 and the value of hyperfine splitting constant predicted from the graph (85.86×10^{-4} cm^{-1}) agrees reasonably well with the observed value. Again, the approximate covalency c is calculated from the hyperfine coupling constant (A_{iso}) by the following equation [22]

$$A_{iso} = (2.04c - 104.5) \times 10^{-4}\ cm^{-1} \quad (5.3)$$

The value obtained is 8 %. This calculated value agrees well with the one calculated from electro negativity relationship, indicating normal ionic character for Mn–O bond of the complex under study.

5.4.2 Optical absorption studies:

Electronic configuration of Mn(II) (d^5) gives rise to free ion terms ^6S, ^4P, ^4F, ^4G in addition to a number of doublet states of which ^6S is the ground state. ^6S and ^4P terms transform as $^6A_{1g}$ and $^4T_{1g}$ respectively, in crystal fields. ^4D and ^4G splits into ^4E_g + $^4T_{2g}$ and $^4A_{1g}$ + ^4E_g + $^4T_{1g}$ + $^4T_{2g}$ respectively. The ground state $^6A_{1g}$ is the only state on the diagram with a multiplicity of 6. This means that for d^5 octahedral complexes, all transitions are not only Laporte forbidden but also spin forbidden. Hence, the molar absorptivity (ε) for many octahedral complexes of d^5 ion, e.g., $[Mn(H_2O)_6]^{2+}$ is 10^{-3} to 1 l mol^{-1} cm^{-1} [23].

Optical absorption spectrum of Mn(II) doped PBMZ, recorded at room temperature in the region 200 – 800 nm, is shown in the Fig. 5.8. The spectrum consists of five bands at 681, 647, 542, 292 and 225 nm characteristic of Mn(II) in octahedral symmetry. Ligand field bands are sharp, when the energy expressions for the transitions are independent of Dq whereas the bands are broad when they depend on Dq. Accordingly the sharp bands at 225 and 292 nm are assigned to the transitions $^6A_{1g}(S) \rightarrow {}^4T_{2g}(D)$ and $^6A_{1g}(S) \rightarrow {}^4E_g(D)$ respectively as its energy expression is independent of Dq. The broad bands at 542 and 647 nm are assigned to the transitions $^6A_{1g}(S) \rightarrow {}^4A_{1g}(G)$, $^4E_g(G)$ and $^6A_{1g}(S) \rightarrow {}^4T_{2g}(G)$ respectively, are dependent on Dq. The other band at 681 nm is assigned to the transition $^6A_{1g}(S) \rightarrow {}^4T_{1g}(G)$, with the help of Tanabe – Sugano diagram [24]. The energy matrices for d^5 configuration with Tree correction (α = 76) are solved for various values of the crystal field parameter (Dq) and Racah parameters (B and C). The values which give best fit with observed data are Dq = 673, B = 612 and C = 3417 cm^{-1}. The observed band positions along with their transitions are given in Table 5.4.

5.4.3 FT-IR Spectral studies:

FT-IR spectra of PBMZ and Mn(II) doped PBMZ at room temperature are shown in Fig. 5.9. FT-IR spectrum of PBMZ shows the characteristic bands for Zn–O, - OH, -OH_2, -C = O and –CH_2. FT-IR spectrum of Mn(II) doped PBMZ also shows similar characteristic bands with light shift due to addition of low concentration of Mn(II). The observed FTIR bands and their tentative assignments [29] for PBMZ and Mn(II) doped PBMZ are given in Table 5.5. In the region of 400 – 4000 cm^{-1}, the spectrum exhibits a number of bands at 719, 793, 862, 945, 1170, 1280, 1370, 1450, 1570, 2340, 2921, 3030, 3190 and 3470 cm^{-1}. The compound consists of H_2O and OH groups in the formula. The bands in the region 1150 – 4000 cm^{-1} are characteristic of these two groups. H_2O has C_{2V} symmetry and accordingly has three fundamental modes of vibrations. The symmetric OH stretch, the asymmetric stretch and H – O – H band are denoted by ν_1, ν_3 and ν_2 respectively. In general, lattice water absorbs at 3550 – 3200 cm^{-1} (antisymmetric and symmetric O–H stretching modes) and at 1630 – 1600 cm^{-1} (H – O – H bending mode).

5.4.4 Powder XRD studies:

Powder XRD pattern of Mn(II) doped PBMZ at room temperature is shown in Fig. 5.10. From powder XRD data, Mn(II) doped PBMZ powder sample has identical lattice parameters as PBMZ powder sample, as expected from the low impurity concentration. The lattice parameters are tabulated in Table 5.6 with the single crystal XRD parameter of PBMC [18]. It is clear from the Table 5.6 that the parameters of PBMZ and Mn(II) doped PBMZ matched with reported values of copper complex [18], confirming that the zinc complex is isomorphic with copper complex and the low dopant concentration of Mn(II) in PBMZ does not alter the symmetry of host lattice.

5.5 Conclusions:

The spin Hamiltonian parameters for Mn(II)/PBMZ have been obtained from single crystal rotation in the three orthogonal planes. The locations of the impurities, in the present case, are found to be interstitial. In the powder spectrum, site 1 is shown by strong lines and the site 2 is shown by very weak lines which are overlapped with site 1. The detailed single crystal data analysis has yielded g, A and D matrices, the direction cosines of which have not matched with the directions of Zn – O in the lattice. The deviation from axial symmetry is reflected more in D tensor than in g and A tensors. The deviation from the axial symmetry shown by the E value confirms the orthorhombic nature of the paramagnetic impurity. The observed band positions in the UV-Visible region confirmed that the Mn(II) ions are in a

distorted octahedral symmetry. The Mn – O bond seems to be almost ionic with only 8% covalency. The structure of the complex has been confirmed from FT-IR and powder XRD studies. The presence of two sites and their interstitial location may be due to the polymeric nature of the host lattice.

References:

[1] A. Abragam, B. Bleaney, "Electron Paramagnetic Resonance of Transition Ions", Clarendon Press, Oxford, 1970.

[2] J.A. Weil, J.R. Bolton, and J.E. Wertz, "Electron Paramagnetic Resonance: Elementary Theory and Applications", John Wiley and Sons, New York, 1994.

[3] J.R. Pilbrow, "Transition Ion Electron Paramagnetic Resonance", Clarendon Press, Oxford, 1990.

[4] B. Sankar, B. Natrajan, S. Mithira, H. Anandhalakshmi, P. Sambasiva Rao, Cryst. Res. Technol., 42 (2007) 173.

[5] S. Deepa, B. Natarajan, S. Mithira, K. Velavan, P. Sambasiva Rao, Radiat. Eff. Defects Solids, 160 (2005) 357.

[6] K. Velavan, R. Venkatesan, P. Sambasiva Rao, J. Phys. Chem. Solids, 66 (2005) 876.

[7] Ram Kripal, D.K. Singh, Spectrochim. Acta, A69 (2008) 889.

[8] S. Boobalan, P. Sambasiva Rao, J. Organo. Chem., 695 (2010) 963.

[9] B. Natarajan, S. Mithira, P. Sambasiva Rao, Solid State Sciences, 10 (2008) 1916.

[10] Ch. Linga Raju, N.O. Gopal, K.V. Narasimhulu, J. Lakshmana Rao, B.C. Venkata Reddy, Spectrochim. Acta, A61 (2005) 2181.

[11] S. K. Misra, S. I. Andronenko, K. A. Earle, J. H. Freed, Appl. Magn. Reson., 21 (2001) 549.

[12] S.K. Misra, S.I. Andronenko, G. Rinaldi, P. Chand, K.A. Earle, J.H. Freed, J. Magn. Reson., 160 (2003) 131.

[13] N.O. Gopal, K.V. Narasimhulu, J. Lakshmana Rao, J. Phys. Chem. Solids, 63 (2002) 295.

[14] T. Bodziony, I.E. Lipinski, L. Kuriata, W. Bednarski, Physica B, 299 (2001) 70.

[15] Jesiamma Joseph, P. Sambasiva Rao, Spectrochim.Acta, A52 (1996) 607.

[16] C. Ruiz-Perez, Y. Rodriguez-Martin, M. Hernandez-Molina, F.S. Delgado, J. Pasan, J. Sanchiz, F. Lloret, M. Julve, Polyhedron, 22 (2003) 2111.

[17] J. Pasan, F.S. Delgado, Y. Rodriguez-Martin, M. Hernandez-Molina, C. Ruiz-Perez, J. Sanchiz, F. Lloret, M. Julve, Polyhedron, 22 (2003) 2143.

[18] Fernando S. Delgado, Catalina Ruiz, Joaquin Sanchiz, Francese Lloret and Miguel Julve Cryst. Eng. Comm., 8 (2006) 507.

[19] EPR-NMR Program developed by F. Clark, R.S. Dickson, D.B. Fulton, J. Isoya, A. Lent, D.G. McGavin, M.J. Mombourquette, R.H.D. Nuttall, P.S. Rao, H. Rinnerberg, W.C. Tennant, and J.A. Weil, University of Saskatchewan, Saskatoon, Canada, 1996.

[20] O. Matamura, J. Phys. Soc. Jpn., 14 (1959) 108.

[21] E. Simanek, K. A. Muller, J. Phys. Chem. Solids, 31 (1970) 1027.

[22] A.M.F. Benial, V. Ramakrishnan, R. Murugesan, Spectrochim. Acta, A55 (1999) 2573.

[23] A.B.P. Lever, "Inorganic Electronic Spectroscopy", 2nd Ed., Elsevier, New York, 1986.

[24] Y. Tanabe, S. Sugano, J. Phys. Soc. Jpn., 9 (1954) 753.

[25] B.N. Figgis, "Introduction to Ligand Fields", Wiley, New York, 1976.

[26] R.M. Krishna, V.P. Seth, S.K. Gupta, D. Prakash, I. Chand, J. Lakshmana Rao, Spectrochim. Acta, A53 (1997) 253.

[27] H. Anandalakshmi, K. Velavan, I. Sougandi, R. Venkatesan, P. Sambasiva Rao, Pramana, 62 (2004) 77.

[28] C. Shiyamala, T.M. Rajendiran, R. Venkatesan, P. Sambasiva Rao, Phys. Scripta., 66 (2002) 183.

[29] K. Nakamoto, P.J. McCarthy, A. Ruby A.E. Martell, J. Am. Chem. Soc., 83 (1961) 1066.

STRUCTURAL ELUCIDATION BY SINGLE CRYSTAL EPR STUDY OF MN(II) DOPED HEXAAQUAZINC DIAQUABISMALONATOZINCATE

6.1 Introduction:

Out of all the first row transition metal ions, EPR studies of Mn(II), high spin d^5 ion, play an important role, as it has five 3d electrons and the ground state is $^6S_{5/2}$. As the resultant angular momentum is zero, only the electron spin contributes for the paramagnetism. When the ground state is a pure sextet, the EPR spectrum would be a single line at free-spin value of 2.0023, because all the five $\Delta M_S = \pm 1$ transitions have the same energy. Since the S-state ions are characterized by long spin lattice relaxation times, it gives well resolved EPR spectra even at room temperature [1, 2]. Hence, these ions have been studied in a variety of crystal lattices [3–5] by EPR technique. Moreover, the zero field splitting is very sensitive even to minute distortions [6] and hence gives explicit information about the crystal symmetry and phase transitions of the host lattice [7-10]. The main emphasis of the EPR studies of Mn(II) in crystals has been the determination of site symmetries and orientations, the study of phase transitions and the magnetic properties of the host lattices. In addition, the effect of charge compensation is also studied in Mn(II) doped single crystals. The impurity ions, such as transition metal ions, are responsible for modification of many physical properties and play a major role in devices like wave-guides, holography and electro-optical devices [11]. Mn(II) ion has been used as a probe in large varieties of host lattices because it shows no Jahn-Teller effect and hence its EPR spectra reflect the true point symmetry.

EPR study of Mn(II) in different host lattices indicate that it can enter the lattice either substitutionally or interstitially or both [12, 13]. Malonic acid acts as a ligand with various dentate abilities. Coordination polymer compounds containing malonic acid as a ligand have been studied due to their potential application as materials in molecular electronics, catalysts, biologically active compounds, molecular-based magnetic materials, microporosity, electrical conductivity, non-linear optical activity, etc. [14, 15]. Additionally, the carboxylate group provides an efficient pathway that couples the magnetic centres either ferro- or antiferromagnetically [16-22], the coupling constant being influenced by structural aspects such as the conformation of the bridge or the geometry of the metal environment. Organic complexes of manganese(II) have studied due to their magnetic interactions [23, 24], formation of self-assemblies of molecular rods and tubes where long distance phenomena,

such as the electron-energy transfer or magnetic coupling in transition ions, which can be changed by structural modifications [25, 26] and in view of short or long order magnetic states [23, 24].

Hence the present study of Mn(II) in hexaaquazincdiaquabismalonato zincate (hereafter abbreviated as HZBMZ) is carried out to ascertain site symmetry, location and also to predict the extent of distortion of symmetry. Also, the relative signs of the zero-field parameters have been ascertained and the percentage covalency of the metal-ligand bond has been estimated.

6.2. Materials and Methods:

6.2.1 Preparation of single crystal of Mn(II) doped $[Zn(H_2O)_6][Zn(mal)_2(H_2O)_2]$:

Malonic acid, basic zinc(II) carbonate and zinc acetate were purchased from commercial sources and used as received. Solid zinc(II) basic carbonate was added to an aqueous solution of malonic acid under continuous stirring. The suspension was heated at 50 – 60 ºC until a clear solution was obtained. This solution was filtered and mixed with an aqueous solution of the zinc(II) acetate. The solution was concentrated to 25 cm^3 in a steam bath and then it was allowed to grow single crystals doped with five different concentrations of manganese sulfate (0.5, 1.0, 1.5, 2.0, and 5.0 %) at room temperature. Well shaped, colorless single crystals suitable for EPR studies were obtained with in fifteen days.

6.2.2 EPR Measurements:

The EPR studies are performed on a JEOL JES-TE100 ESR spectrometer operating at X-band frequencies, having a 100 kHz field modulation to obtain the first-derivative EPR spectrum at room temperature. 1,1-Diphenyl-2-picrylhydrazyl (DPPH) with a g-value of 2.0036 was used as a reference for g-factor calculations.

6.2.3 UV-Visible, FT-IR, Powder XRD Measurements:

UV – Vis absorption spectrum of the powder sample in the range of 200 – 1200 nm was recorded on a Varian Cary 5000 ultraviolet-visible (UV-Vis) near-infrared spectrophotometer. FT - IR spectra of doped and undoped materials in the frequency range of 4000-400 cm^{-1} were recorded on a Shimadzu FT-IR-8300/8700 spectrometer with the samples prepared as KBr pellets. The powder XRD studies were carried out for doped and undoped materials on a PANalytical X'pert PRO diffractometer with Cu Kα radiation of wavelength λ = 0.15406 nm, 2θ values between 5-75°, at room temperature.

6.3. Crystal structure:

$[Zn(H_2O)_6][Zn(mal)_2(H_2O)_2]$ is isostuctural with $[Zn(H_2O)_6][Cu(mal)_2(H_2O)_2]$ (hereafter referred as HZBMC) [27]. HZBMC belongs to triclinic crystal system with space group $P\bar{1}$, having unit cell parameters a = 0.5274 nm, b = 0.7504 nm, c = 1.0314 nm, α = 106.92°, β = 99.15°, γ = 95.81° and Z = 2. The coordination polyhedron of the copper atom in the anionic unit $[Cu(mal)_2(H_2O)]^{2-}$ is that of an elongated octahedral CuO_6. Four carboxylate oxygens from two bidentate malonate ligands build the equatorial plane, whereas two water molecules occupy the axial sites. The zinc(II) ion in the cationic units $[Zn(H_2O)_6]^{2+}$ is coordinated to six water molecules with a slightly distorted octahedral geometry.

6.4. Results and Discussion:

6.4.1 EPR studies:

The ground state of Mn(II) ion, with a d^5 configuration is unique among d^n configurations, in that there is only one state with maximum spin multiplicity (^6S). This splits into three Kramers' doublets (±5/2, ±3/2 and ±1/2) in an orthorhombic crystalline field, which are further split in the presence of an applied magnetic field. These six levels give rise to five fine-structure transitions. Each fine-structure transition splits into six levels, due to nuclear spin of ^{55}Mn (I = 5/2) giving rise to 30 allowed transitions. However, in polycrystalline samples, only $|+1/2\rangle \leftrightarrow |-1/2\rangle$ transition is generally observed, since the other four transitions have large anisotropy [1]. If zero-filed splitting parameter (D) is very small compared to hyperfine coupling constant (A), the 30 line pattern will be so closely packed that one could see only six lines. On the other hand, if D is very large, one would expect five bunches of resonance lines, each bunch split into a sextet.

Single crystals of optimum size are selected for crystal rotations along the three mutually perpendicular crystallographic axes, i.e., *a**, *b* and *c**. Axis *c** is perpendicular to the crystal axis *b* in the *bc* crystal plane and axis *a** is orthogonal to *b* and *c**. In other words, a*bc* corresponds to orthogonal xyz coordinate system. As the crystals were grown with five different dopant concentrations, crystals with 0.5, 1.0 and 1.5 % concentration show weak lines; whereas crystals with 5.0 % gave relatively broad lines. Hence, in all the further EPR measurements, crystals with dopant concentration of 2.0 % are used. However, 5.0 % concentration samples are used for powder XRD, IR and optical measurements. Single crystal EPR measurements of Mn(II)/HZBMZ at room temperature show a variety of complicated spectra. A typical EPR spectrum of Mn(II)/HZBMZ, when the applied magnetic field (B) is parallel to axis c*, is shown in Fig. 6.1. It clearly indicates a 30 line pattern. In

addition, a few resonances are seen at the centre of the spectrum suggesting a second site, with relatively small zero field value. This second site could not be followed during crystal rotations, due to its low intensity and overlap with the transitions of the other site. The transitions are marked in the figure. Another spectrum, when B is parallel to axis a* is shown in Fig. 6.2. Here, all the transitions are merged indicating a very low value of zerofield splitting (see below). Generally, one expects the intensity of fine-structure lines for Mn(II) system to be in the ratio of 5:8:9:8:5. However, in the present case, this ratio is randomly distributed in all the three planes. This may be due to the overlap other site, which shows at random orientations. Fig. 6.3 showing the single crystal EPR spectrum of Mn(II)/HZBMZ when B is perpendicular to axis b.

Crystal rotations are carried out in the three mutually orthogonal planes and iso frequency plots in *a*c** and *bc** planes are shown in Figs. 6.4 and 6.5 respectively. In these figures, maximum spread is noticed at $\theta = 0^{o}$ and the spread between two extreme fine-structures decreases as θ increases. At $\theta = 54.7^{o}$, the fine-structure lines collapse in Fig. 6.4 and moderately collapse in Fig. 6.5. This orientation roughly corresponds to the magic angle, where D becomes zero. Further increase of θ, again increases the spread and the pattern is repeated. This shows that the angular variation of fine-structure follows a $(3\cos^2\theta - 1)$ variation. In the two iso-frequency plots, only the resonance lines corresponding to $(|\pm 5/2> \leftrightarrow |\pm 3/2>)$ and $(|\pm 3/2> \leftrightarrow |\pm 1/2>)$ are given, and resonance lines due to $|+1/2> \leftrightarrow |-1/2>$ transition, which are independent of D, are not given because of invariant. In malonato ligand complexes, the iso frequency plot for $(|-5/2> \leftrightarrow |-3/2>)$ transition is narrow but the $(|+5/2> \leftrightarrow |+3/2>)$ transition is broad for Mn(II) ion dopant [28]. From these iso-frequency plots, the spin-Hamiltonian parameters are calculated as mentioned below.

6.4.1.1 Calculation of spin Hamiltonian parameters:

The spin-Hamiltonian for a spin sextet, including second order effects is given by [1]

$$H = \beta(g_{xx}B_xS_x + g_{yy}B_yS_y + g_{zz}B_zS_z) + (A_{xx}S_xI_x + A_{yy}S_yI_y + A_{zz}S_zI_z) + D[S_2^2 - \frac{1}{3}S(S+1)] + E(S_x^2 - S_y^2) \quad (6.1)$$

Here the first term represents the electron Zeeman interaction, the second represents the hyperfine interaction, the third term represents zero-field splitting and the fourth term represents deviation from axial symmetry. The spin-Hamiltonian parameters, obtained by using the resonance data in all the three planes with program EPR-NMR [29] are given in Table 6.1, along with the direction cosines. The direction cosines of metal-oxygen bonds have been calculated from the single crystal XRD data of the HZBMC and are given in Table

6.2. A few set of spin-Hamiltonian parameters, taken from literature are given in Table 6.3, for comparison, where a good agreement is noticed. As suggested earlier, deviation from axial symmetry is seen and the calculated *E* value is 15.6 mT.

Using the *g* and *A* values obtained in the EPR-NMR program, the iso-frequency plots are simulated for *a*c** and *bc** planes and are also given in Figs. 6.4 and 6.5. In these figures, solid lines correspond to theoretical variation and the solid circles correspond to the experimental data. A good agreement is observed in both the planes, confirming the accuracy of calculated spin-Hamiltonian parameters.

Since the isotropic hyperfine coupling constant arises by the use of the polarization of the inner s-electrons, the sign of A for high spin Mn(II) complexes is always assigned as negative [30]. The sign of D is assigned relative to A by considering the separation between hyperfine lines at low field and high field. If the separation between hyperfine lines in the low field is greater than the high field, then the ratio D/A becomes positive or negative for the reverse case. In the present case, the separation increases from lower filed to higher field, D/A is positive. Since A is negative, D becomes positive. This is also confirmed by measuring the spectra at lower temperatures.

Generally, Mn(II) ions enter the lattice either substitutionally or interstitially. A survey of literature shows that Mn(II) ion invariably enters the Zn(II) host lattices substitutionally and this may be attributed to comparable ionic radii of Mn(II) (0.08 nm) and Zn(II) (0.08 nm). So it is reasonable, here also, to assume that the Mn(II) ions enter substitutionally at Zn(II) sites in the HZBMZ lattice.

6.4.1.2 Location of the impurity:

The location of the impurity can be detected by comparing the direction cosines of the principal values of *g* and *A* tensors with any of the metal-ligand bond directions (Zn–O). The direction cosines of *g*, *A* and *D* are tabulated in Table 6.1 and that of metal ligand bond direction cosine of HZBMC crystal lattice are given in Table 6.2. It is evident from the table that one of the direction cosines of the one of the principal g value (2.0236) is found to match fairly well with that of the metal-oxygen (Zn–O1w) bond direction. The deviation between these directions is around 5º. This suggests that the Mn(II) ion has entered the lattice substitutionally.

6.4.1.3 Polycrystalline EPR spectrum:

In order to reconfirm the single crystal analysis, powder spectrum of the Mn(II) doped HZBMZ is recorded at room temperature. The room temperature powder EPR spectrum is given in Fig. 6.6. Here one can notice clearly six lines (corresponding to $|+1/2\rangle \leftrightarrow |-1/2\rangle$

transition) indicating a single site of Mn(II) ion. Generally, due to large anisotropic effects in *D*, the other four transitions corresponding to (|±5/2>↔|±3/2>) and (|±3/2>↔|±1/2>) are weak. The powder spectrum is not symmetrical with respect to central portion of the spectrum indicating the presence of deviation from axial zero-field terms. This means that D_{xx} and D_{yy} are different. The spin Hamiltonian parameters (*g*, *A* and *D*) obtained from the powder spectrum, are also given in Table 6.3. These values agree well with the crystal data. Here, it is to be noted that D obtained from powder spectrum is related to D_{zz} by the equation, $D = (3/2)D_{zz}$ and $E = 1/2|(D_{xx}-D_{yy})|$.

6.4.1.4 Covalency of the metal-ligand bond:

The percentage of covalency of the Mn–O bond has been calculated using Matamura's plot [33]. The covalency of the bond between manganese and its ligands depends on the isotropic hyperfine coupling constant *A*. The empirical relationship for the covalency of a bond between the *p* and *q* and their electronegativities χ_p and χ_q is given by

$$C = 1/n[1 - 0.16(\chi_p - \chi_q) - 0.035(\chi_p - \chi_q)^2] \quad (6.2)$$

Here, n is the number of ligands around Mn(II) ion. The percentage of covalency obtained from the above equation, assuming $\chi_{Mn} = 1.55$ and $\chi_O = 3.44$ is around 9.5 %. The value of hyperfine splitting constant predicted from the graph (89.5×10^{-4} cm^{-1}) is in reasonable agreement with the observed value from powder spectrum.

6.4.2 Optical absorption studies:

Optical absorption spectrum of Mn(II) ion doped in HZBMZ, recorded at room temperature, is shown in Fig. 6.7. Mn(II) d–d absorption transitions are difficult to be seen as these are spin and parity forbidden in octahedral symmetry. However, charge transfer (CT) bands are parity allowed [34]. The sharp band at 211 nm is assigned to $^6A_{1g}$ (S) → $^4A_{2g}$ (F), the weak band at 273 nm is assigned to $^6A_{1g}$ (S) → $^4T_{2g}$ (D) of Mn(II) ion, which exits in the UV-region in absorption spectrum. The band at 273 nm is low in sharpness and intensity compared with 211 nm band. The strong and weak bands at 211 and 273 nm respectively have been attributed to the transitions of electron from ground state to excited states $^4A_{2g}$(F), $^4T_{2g}$ (D) respectively.

6.4.3 FT-IR Spectral studies:

The infrared spectra of carboxylic acids display two important features: first due to very strong hydrogen bonding between the carboxyl groups of acid molecules, the bands will appear as strong and broad from 3400 to 2500 cm^{-1} stretching frequencies of the O–H single bond and second, the stretching frequency for the carbonyl group of the carboxylic acid appears in one of the two regions [35-37]. FT-IR spectra of HZBMZ and Mn(II) doped

HZBMZ at room temperature are shown in Fig. 6.8. The infrared band positions and their tentative assignments for HZBMZ sample observed in the present work are given in Table 6.4.

6.4.4 Powder XRD studies:

Powder XRD pattern of Mn(II) doped HZBMZ at room temperature is shown in Fig. 6.9. According to powder XRD measurements, Mn(II) doped HZBMZ powder sample has identical lattice parameters as HZBMZ powder sample, as expected from the low impurity concentration. The lattice parameters are tabulated in Table 6.5 with the single crystal XRD parameter of HZBMC [27]. It is clear from the table that the parameters of HZBMZ and Mn(II) doped HZBMZ matched with reported values of copper complex [27], confirming that the zinc complex is isomorphic with copper complex and the low dopant concentration of Mn(II) in HZBMZ does not alter the symmetry of host lattice.

6.5. Conclusion:

EPR spectra of Mn(II) doped HZBMZ have been studied at room temperature. The angular variation reveals the presence of more than one site, which correspond to distinct sites of Mn(II). The detailed EPR analysis of one site indicates that Mn(II) ion has entered the lattice substitutionally. The evaluated spin Hamiltonian parameters reflect orthorhombic symmetry. The magnitude of the hyperfine splitting constant *A* indicates that the bonding between the paramagnetic ion and the ligand is ionic in nature. The large *D* and *E* values reveal the distortion present in the crystal lattice due to steric effects of the crystal packing caused by malonate ligands. From the observed band positions assigned to charge transfer transition in the UV region, the Mn(II) ions are in a distorted octahedral symmetry. The observed bands in the FT-IR spectrum have been assigned to Zn-O, O-H, -C=O, -C-O, -CH_2- and H_2O bonds. Powder XRD confirms the formation of HZBMZ which is isomorphous with HZBMC.

References:

[1] A. Abragam, B. Bleaney, “Electron Paramagnetic Resonance of Transition Ions”, Clarendon Press, Oxford, 1970.

[2] J.R. Pilbrow, “Transition Ion Electron Paramagnetic Resonance”, Clarendon Press, Oxford, 1990.

[3] B. Natarajan, S. Mithira, P. Sambasiva Rao, Solid State Sciences, 10 (2008) 1916.

[4] Ram Kripal, Har Govind, Manisha Bajpai, Manju Maurya, Spectrochim. Acta, A71 (2008) 1302.

[5] Jessiamma Joseph, P. Sambasiva Rao, Spectrochim. Acta, A52 (1996) 607.

[6] Sushil K. Misra, Serguei I. Andronenko, Prem Chand, Keith A. Earle, Sergei V. Paschenko, Jack H. Freed, J. Magn. Reson., 174 (2005) 265.

[7] K. Velavan, R. Venkatesan, P. Sambasiva Rao, J. Phys. Chem. Solids, 66 (2005) 876.

[8] R. Murugesan, A. Thamaraichelvan, A.M. Franklin, V. Ramakrishnan, Mol. Phys., 79 (1993) 663.

[9] R. Kripal, H. Govind, M. Maurya, J. Magn. Magnetic Mat., 308 (2007) 243.

[10] Ch. Linga Raju, N.O. Gopal, K.V. Narasimhulu, J. Lakshmana Rao, B.C. Venkata Reddy, Spectrochim. Acta, A61 (2005) 2181.

[11] Wen-Chen Zheng, Phys. Status Solidi. B 205 (1998) 627.

[12] S.N. Rao, Y.P. Reddy, P.S. Rao, Solid State Commun., 82 (1992) 419.

[13] R. Murugesan, V.S.X. Anthonisamy, S. Subramanian, Spectrochim. Acta, A49 (1993) 1801.

[14] C. Ruiz-Perez, Y. Rodriguez-Martin, M. Hernandez-Molina, F.S. Delgado, J. Pasan, J. Sanchiz, F. Lloret, M. Julve, Polyhedron, 22 (2003) 2111.

[15] J. Pasan, F.S. Delgado, Y. Rodriguez-Martin, M. Hernandez-Molina, C. Ruiz- Perez, J. Sanchiz, F. Lloret, M. Julve, Polyhedron, 22 (2003) 2143.

[16] C. Oldham, in: G. Wilkinson, R.D. Gillard, J.A. McCleverty (Eds.), “Comprehensive Coordination Chemistry”, vol. 2, Pergamon Press, Oxford, 1987, 435.

[17] D.K. Towle, S.K. Hoffmann, W.E. Hatfield, P. Singh, P.Chaudhuri, Inorg. Chem., 27 (1988) 394.

[18] P.R. Levstein, R. Calvo, Inorg. Chem., 29 (1990) 1581.

[19] F. Sapin˜ a, E. Escriva´, J.V. Folgado, A. Beltra´n, A. Fuertes, M. Drillon, Inorg. Chem., 31 (1992) 3851.

[20] E. Colacio, J.P. Costes, R. Kiveka¨s, J.P. Laurent, J. Ruiz, Inorg. Chem., 29 (1990) 4240.

[21] E. Colacio, J.M. Domı´nguez-Vera, J.P. Costes, R. Kiveka¨ s,J.P. Laurent, J. Ruiz, M. Sundberg, Inorg. Chem., 31 (1992) 774.

[22] E. Colacio, J.M. Dominguez-Vera, R. Kivekäs, J.M. Moreno, A. Romerosa J. Ruiz. Inorg. Chim. Acta, 212 (1993) 115.

[23] A.N Papadopoulos, Inorg. Chem., 35 (1996), 559.

[24] V. Tangoulis, D.A. Malamatari, K. Soulti, V. Stergiou, C.P. Raptopoulos, A. Terzis, T.A. Kabanos, D.P. Kessissoglou, Inorg. Chem., 35 (1996) 4974.

[25] H. Li, C.E. Davis, T.L. Groy, D.G. Kelley, O.M. Yaghi, J. Am. Chem. Soc., 120 (1998) 2186.

[26] S.K. Chawla, A. Arora, K. Nattinen, K. Rissanen, J.V. Yakhmi, Polyhedron, 23 (2004) 3007.

[27] Y. Rodriguer-Martin, J. Sanchiz, C. Ruiz-Perez, F. Lloret, M. Julve, Cryst. Eng. Comm., 4 (2002) 631.

[28] B. Natarajan, Ph,D. Thesis submitted to Pondicherry University, Pondicherry, 2007.

[29] EPR-NMR Program developed by F. Clark, R.S. Dickson, D.B. Fulton, J. Isoya, A. Lent, D.G. McGavin, M.J. Mombourquette, R.H.D. Nuttall, P.S. Rao, H. Rinnerberg, W.C. Tennant, J.A. Weil, University of Saskatchewan, Saskatoon, Canada, 1996.

[30] M. Korkman, M. Dupont, B. Aktas, J. Phys. Chem. Solids, 45 (1984) 465.

[31] R.M. Krishna, V.P. Seth, R.S. Bensal, I. Chand, S.K. Gupta, J.J. Andre, Spectrochim. Acta, A54 (1998) 517.

[32] P.Chand and O.P. Agarwal, Spectrochim. Acta, A47 (1991) 775.

[33] O. Matumura, J. Phys. Soc. Jpn., 14 (1959) 108.

[34] R. Selomulya, S. Ski, K. Pita, C.H. Kam, Y. Zhang, S. Buddhudu, Mater. Sci. Eng. B, 100 (2003) 136.

[35] K. Nakamoto, “Infrared and Raman Spectra of Inorganic and Coordination Compounds”, 4th Ed, John Wiley Interscience, New York, 1986.

[36] N.O. Gopal, K.V. Narasimhulu, J. Lakshmana Rao, J. Phys. Chem. Solids, 63 (2002) 295.

[37] R.M. Silerstein, G. Clayton Bassler, T.C. Morril, “Spectrometric Identification of Organic Compounds”, 5th Ed., Wiley, New York, 1991.

IDENTIFICATION OF STRUCTURE AND POSITION OF Cu(II) ION DOPED IN AQUOMETHYLMELONATOZINC(II) HOST BY EPR SPECTROSCOPY

7.1 Introduction:

Electron paramagnetic resonance (EPR) spectroscopy has been used extensively as a powerful tool to identify the characteristics of transition metal ions. As Cu(II) ion is a simplest probe to enter a diamagnetic host lattice easily, an idea about the ground state of the ion, the type of distortion, the position of the paramagnetic impurity and so on [1-5] can be obtained from single crystal EPR study. The diamagnetic host ions possess a closed outer electronic shell, there by causing the local symmetry of the host lattice to be high. When Cu(II) ions are introduced in such host lattices, substituting for the diamagnetic ions, local distortions will take place, because of the mismatch of Cu(II) ion size to that of the host ions and dynamic effects such as the Jahn-Teller effect [6]. In addition, these studies also provide additional information about the ground state (compressed/elongated octahedron) and type of Jahn-Teller distortions (static/dynamic/tunneling) [3, 7-9]. Moreover, EPR studies on paramagnetic systems will also help to identify the ground state of the ion in low symmetry environments, along with relaxation times [3, 7, 10-23]. Cu(II) ion with d^9 electronic configuration has the ground state arrangement of six electrons in t_{2g} orbital and the other three electrons in doubly degenerate e_g orbital, when the crystal symmetry is octahedral. The orbital degeneracy is removed either by a lowering in symmetry arising due to charge compensating vacancies, crystalline fields, etc. or by Jahn-Teller distortion [7, 12-16]. In those situations, the ground state will be $d_{x^2-y^2}$ or d_{z^2}. However, in most cases, the symmetry is low enough to remove the degeneracy. In the majority of Cu(II) system studied so far, the ion was found in $d_{x^2-y^2}$ ground state corresponding to axial elongation. However a few systems were known, which exhibit axial compression corresponding to d_{z^2} ground state [10, 11]. In the present chapter, single crystal EPR studies of Cu(II) in aquomethylmelonatozinc(II) at 300 K are reported.

7.2 Experimental Methods:

7.2.1 Preparation of single crystals of Cu(II) doped [Zn(methylmelonato)(H_2O)]$_n$:

[Zn(methylmelonato)(H_2O)]$_n$ was synthesized by adding zinc(II)nitrate trihydrate, containing five different concentrations of copper(II)nitrate trihydrate (0.5, 1.0, 1.5, 2.0 and 5.0 %), was added to an aqueous solution of methylmalonic acid and sodium carbonate under

stirring. The resulting solution was filtered and on slow evaporation at room temperature yielded transparent and light bluish crystals. Aquomethylmelonatozinc(II) is abbreviated here as AMMZ.

7.2.2 EPR Measurements:

The EPR spectra are recorded at 300 K on a JEOL JES-TE100 ESR spectrometer operating at X-band frequencies, having a 100 kHz field modulation to obtain the first-derivative EPR spectrum. 1,1-Diphenyl-2-picrylhydrazyl (DPPH) with a g-value of 2.0036 is used as a reference for g-factor calculations.

7.2.3 UV-Visible, FT-IR, Powder XRD Measurements:

The optical spectrum has been recorded at room temperature using a Varian Cary 5000 ultraviolet-visible (UV-Vis) near-infrared spectrophotometer in the range of 200-1300 nm. In the present investigation, the FT-IR spectra are recorded for doped and undoped materials on a Shimadzu FT-IR-8300/8700 spectrometer, in the frequency range of 4000-400 cm^{-1}. The measurements are made using almost transparent KBr pellets containing fine-powdered samples at room temperature. In the current study, powder XRD studies are carried out for doped and undoped materials on a PANalytical X'pert PRO diffractometer with Cu Kα radiation of wavelength λ = 0.15406 nm, 2θ values between 5-75°, at room temperature.

7.3 Crystal structure:

[Zn(methylmelonato)$(H_2O)]_n$ is isostructural with [Cu(methylmelonato)$(H_2O)]_n$ (abbreviated as AMMC) [24] and belongs to orthorhombic crystal class with space group $Pn2_1m$, having unit cell parameters a = 0.6203 nm, b = 0.6796 nm, c = 0.6998 nm and Z = 2. The copper complex exhibits perfect square pyramidal structure. The apical position is filled by a water molecule and the equatorial positions are occupied by four methylmalonate oxygen atoms in which two oxygen atoms donated by bidentate methylmalonate ligand, other two oxygen atoms donated by each of two monodentate methylmalonate ligand.

7.4 Results and Discussion:

7.4.1 EPR Studies:

As single crystals of Cu(II) with various concentrations are grown, the EPR spectra are recorded for all the samples. Among the five concentration crystals (0.5, 1.0, 1.5, 2.0 and 5.0 %), the low concentrations 0.5, 1.0 and 1.5 % are gave very weak resonance lines, which are difficult to follow during crystal rotations. In case of crystals with 5.0 % dopant

concentration, the lines are broad due to dipole-dipole interactions. Hence, in the present study, crystals with 2.0 % dopant concentration have been used for single crystal EPR studies, due to well resolved hyperfine resonance lines. However, for IR, optical and powder XRD studies, sample with 5.0 % concentration is used. In all the crystals with different dopant concentrations, the number of impurity sites remained the same indicating that dopant concentration has no effect on the number of sites observed in EPR spectrum. Single crystal EPR spectra of Cu(II) doped AMMZ are recorded at 300 K. A good single crystal was mounted along crystallographic axis b and a typical EPR spectrum, when the external magnetic field (B) is parallel to crystallographic axis a is shown in Fig. 7.1. It consists of four resolved resonance lines characteristic of Cu(II) with S = 1/2 and I = 3/2. During crystal rotation in bc plane, the resonance lines show anisotropy. Other EPR spectra, when B//c and B//b are given in Fig. 7.2 and Fig. 7.3 respectively. During single crystal rotations, variation in hyperfine resonance positions in ab, ac and bc planes have been noticed. In order to obtain spin Hamiltonian parameters for Cu(II)/AMMZ, crystal rotations were performed in the three mutually orthogonal planes and the isofrequency plots are given in Figs. 7.4, 7.5 and 7.6 respectively for ab, ac and bc planes. Here, mention is made that during crystal rotations, only one set of four lines are observed in all the three planes, even though the unit cell contains two molecules. In all the isofrequency plots, the experimental field positions are represented by closed circles.

7.4.1.1 Calculation of spin-Hamiltonian parameters:

The angular variation of the Cu(II) hyperfine resonances in the three planes has been successfully fitted to the following spin Hamiltonian using program EPR-NMR [25] to obtain spin Hamiltonian parameters.

$$H = g_{xx}\beta B_x S_x + g_{yy}\beta B_y S_y + g_{zz}\beta B_z S_z + A_{xx} S_x I_x + A_{yy} S_y I_y + A_{zz} S_z I_z \qquad (7.1)$$

where the symbols have their usual meaning. The values thus obtained from the program are given in Table 7.1, along with the respective direction cosines.

A close look at Table 7.1 indicates that the system represents orthorhombic symmetry and the direction cosines of principal values of g and A are coincided. The next aim is to obtain the location of the paramagnetic impurity, Cu(II). For this, one has to compare the direction cosines of the principal values of g/A with the direction cosines of metal-ligand bond directions in the crystal lattice. From the X-ray data of AMMZ, the various Zn-O bond directions have been calculated and are presented in Table 7.2. It is clear from these two tables that one of the direction cosines of Zn-O bond matched with the principal values of

g/A. Hence, it can be suggested that the paramagnetic impurity has entered the lattice substitutionally.

7.4.1.2 Orientation of impurity:

The angular variation studies show that the copper ion has occupied substitutional site by replacing the Zn(II) ion in the AMMZ lattice. Using X-ray data of AMMC [24], the direction cosines of the five metal-oxygen bond directions have been calculated and are given in Table 7.2. The direction cosines of the principal g values are match fairly well with that of the Zn–O (1a) bond direction, the deviation angle being small (9º).

7.4.1.3 Polycrystalline spectrum:

In order to confirm the single crystal analysis, powder spectrum of the sample is recorded at room temperature and is given in Fig. 7.7. It clearly indicates the axially symmetric nature of the impurity. Due to large line width in powder spectrum, the perpendicular component does not show further splitting, a common observation in most of the Cu(II) complexes. The *g* and *A* values have been calculated from this spectrum and are given in Table 7.3, along with the values for Cu(II) systems in other host lattices. Using these parameters and Bruker Simfonia program, the powder spectrum has been simulated and included in Fig. 7.7 itself. The agreement is very good and the values have matched well with the single crystal analysis. As the perpendicular hyperfine lines are not resolved and A_{zz} value deviates from single crystal data at room temperature in the powder spectrum, the sample is cooled to 77 K. The 77 K EPR spectrum of the powder sample does not show any change in *g* and *A* values and in resolution.

A close look at the hyperfine values indicates that one of the principal values (A_{zz}) is appreciably smaller than a generally observed value of $A_{\parallel}$ for a copper ion. A few systems, having a smaller A_{zz} hyperfine value, have been selected from the literature and are given in Table 7.3, for comparison. This low value of A_{zz} has been explained by considering the admixture of $d_{x^2-y^2}$ (ground state) with d_{z^2} (excited state) orbital and metal – ligand covalent character [26]. The spin orbit coupling will further modify the weights of the mixing of the eigenstates. Generally, this contribution will be small. However, a significant contribution is needed to explain the observed very low hyperfine coupling constant. In other words, the magnitude of A_{zz} gets decreased because of the opposite sign of hyperfine coupling value for the electrons in $d_{x^2-y^2}$ and d_{z^2} orbital. The total dipolar coupling gets vanished to first order, for 1:1 admixture of $d_{x^2-y^2}$ and d_{z^2}. Hence it is found that a 10 % admixture of $d_{x^2-y^2}$ and d_{z^2} results in a 20 % reduction in dipolar anisotropy. The low hyperfine value is also due to a direct mixing of metal 4s orbital with the ground state orbital of Cu(II) having low symmetry.

The admixture opposes the core polarization of isotopic coupling, which occurs due to the involvement of outer 4s orbital, results in the reduction of hyperfine values [27, 28]. This is mainly due to the presence of electron in a $d_{x^2-y^2}$ orbital, which is the ground state. The admixture coefficients of $d_{x^2-y^2}$ and d_{z^2} can be evaluated using the method given in the literature [29].

7.4.1.4 Calculation of admixture and molecular orbital parameters:

From g values, the coefficients of the d-orbital of the Kramers' doublet are determined. The $d_{x^2-y^2}$ orbital gets admixed with d_{xy}, d_{yz} and d_{xz}. The d_{z^2} gets admixed with d_{yz} and d_{xz}. The Kramers' doublet wave function for the ground state can be expressed as,

$$\psi = a\phi_1\alpha + b\phi_3\alpha + ic\phi_2\alpha - id\phi_4\beta - e\phi_5\beta \quad (7.2)$$

$$\psi^* = i(a\phi_1\beta + b\phi_3\beta - ic\phi_2\beta - id\phi_4\alpha + e\phi_5\alpha) \quad (7.3)$$

Where $\phi_1 = d_{3z^2-r^2}(A)$; $\phi_2 = d_{xy}(B_1)$; $\phi_3 = d_{x^2-y^2}(A)$; $\phi_4 = d_{yz}(B_3)$ and $\phi_5 = d_{xz}(B_2)$.

This equation represents that if a = 1, the system has d_{z^2} ground state and lowest A_{33} value and if b = 1, the system is in $d_{x^2-y^2}$ ground state and maximum hyperfine value. The constants a, b, c, d and e indicate the mixing of d-orbital brought about by metal spin – orbit coupling. In terms of admixture coefficients, the expression for the g and A values are given as,

$$g_z = 2 - 4d^2 - 4e^2 + 8bc + 4de \quad (7.4)$$

$$g_y = 2 - 4c^2 - 4e^2 + 4\sqrt{3}ad - 4ce + 4bd \quad (7.5)$$

$$g_x = 2 - 4c^2 - 4d^2 + 4\sqrt{3}ae - 4be + 4cd \quad (7.6)$$

$$A_z = P\{8bc + 4de + (6\xi - \kappa)(1 - 2d^2 - 2e^2) - 3\xi[4c^2 + 4b^2 - e^2 + \sqrt{3}a(d + e) + 3(d - e)(c - b)]\} \quad (7.7)$$

$$A_y = P\{4\sqrt{3}ad - 4ce + 4bd + (6\xi - \kappa)(1 - 2c^2 - 2e^2) - 3\xi[(\sqrt{3}a + b)^2 - c^2 + 4d^2 - e^2 - \sqrt{3}a(e + 2c) + 3dc\ 3be - 3de]\} \quad (7.8)$$

$$A_x = P\{4\sqrt{3}ae + 4dc - 4be + (6\xi - \kappa)(1 - 2c^2 - 2d^2) - 3\xi[(\sqrt{3}a + b)^2 - c^2 - d^2 + 4e^2 - \sqrt{3}a(d - 2c) + 3ce - 3db - 3de]\} \quad (7.9)$$

a, b, c, d and e are the coefficients of ϕ_1, ϕ_2, ϕ_3, ϕ_4, and ϕ_5 [18] respectively. ξ is a constant and depends on the electronic configuration of the ion and the value of ξ = 2/21 for Cu(II) ion. P is the gyromagnetic ratio of copper and its free ion value is 360×10^{-4} cm^{-1} and κ is the Fermi contact term, which is a measure of bonding effects on the Cu(II) in crystal lattice. From the Spin Hamiltonian parameters, the dipolar term (P) and Fermi contact term (κ) [30] are calculated using the following expressions:

$$A_{\parallel} \approx P[-(4\alpha^2/7) - \kappa + (g_{\parallel} - g_e) + 3/7(g_{\perp} - g_e)] \quad (7.10)$$

$$A_{\perp} \approx P[(2\alpha^2/7) - \kappa + 11/14\ (g_{\perp} - g_e)] \quad (7.11)$$

$$P = 2r_{Cu}\beta_0\beta_N(r^{-3}), \quad (7.12)$$

$$\kappa = A_0/P + \Delta g_0 \quad (7.13)$$

Here r_{Cu} is the magnetic moment of copper, β_0 is the Bohr magneton, β_N is the nuclear magneton and r is distance of the central nucleus to the electron. $A_0 = (A_{\parallel} + A_{\perp})/3$, where $A_{\parallel}$ and $A_{\perp}$ are the hyperfine coupling constants in the parallel and perpendicular directions to the field and $\Delta g_0 = g_0 - g_e$ where $g_0 = (g_{\parallel} + g_{\perp})/3$ and g_e is the free-electron g value (2.0023). The Fermi contact term κ is a measure of the polarization produced by the uneven distribution of d-electron density on the inner core s-electron and it has been suggested [31] that 3d transition metal ions, $\kappa = 0.3$. The values of P and κ obtained are 0.030 cm^{-1} and 0.352 (by assuming axial symmetry taking the average value of g_{yy} and g_{zz} for $g_{\perp}$ and A_{yy} and A_{zz} for $A_{\perp}$). Assuming that $d = -e$, the coefficients a, b, c and d have been calculated and given in Table 7.4. Using a similar procedure, the coefficients have been calculated for Cu(II)/AMMZ also and are included in Table 7.4, along with some other values. As expected, an increase in the coefficient of a is noticed whenever a decrease in hyperfine is observed.

From the above equations, P and κ have been calculated and are given in Table 7.5, along with some known values. The ratio of $P_{complex}$ to P_{free} ion is around 84 %, indicating the delocalization of the d-electron. The percentage of unpaired spin density on copper ion is 16 % and the remaining density is being distributed onto the ligands. The molecular orbital coefficient α^2, which gives a measure of covalent nature of σ-bonding is given as,

$$\alpha^2 = (A_{\parallel}/0.036) + (g_{\parallel} - 2.0023) + 3/7\ (g_{\perp} - 2.0023) + 0.04 \quad (7.14)$$

α' can be evaluated from the normalization condition on the ground state orbital as

$$\alpha' = (1 - \alpha^2)^{1/2} + \alpha S \quad (7.15)$$

where S is the overlap integral between $d_{x^2-y^2}$ orbital and normalized ligand orbital. The value of S is given as 0.076 for a copper complex with water ligands. The complex is found to be partially covalent in nature. These values are also given in Table 7.5. Value of β_1^2 which is a direct measure of the covalence of the in-plane π-bonding is calculated using the formula

$$g_{\parallel} = 2.0023 - 8\rho[\alpha\beta_1 - 1/2\ \alpha'(1 - \beta_1^2)^{1/2}T(n)] \quad (7.15)$$

where $\rho = \lambda_0\ \alpha\beta_1/\Delta E$, $T(n)$ is a function involving metal – ligand distance, hybridization constant (n) and effective nuclear charges for the ligand 2s, 2p orbitals and the metal 3d

orbital. Assuming λ_0 = -828 cm^{-1} and $T(n)$ = 0.220, the calculated values of the covalence parameters are

α^2 = 0.778; α' = 0.470; α = 0.882; β_1^2 = 0.221; β_1 = 0.470;

The parameter α^2 describes the covalence of the σ bond between the metal and its ligands. It has a value of unity, if the bond is totally ionic and 0.5 if it is completely covalent. The present value of α^2 = 0.778 indicates moderate covalence for the in-plane σ bonding and β_1^2 = 0.221 indicates greater covalence for the in-plane π-bonding. Here it may be mentioned that β_1^2 is more sensitive to variations in covalence than α^2 and is therefore a better indicator of covalent character [32]. Yet, another parameter *R*, the ratio difference between second and third value to first and second values of the increasingly arranged g value is also calculated, which gives an idea about the ground state nature of the paramagnetic impurity on the host lattice.

$$R = (g_2 - g_3)/ (g_1 - g_2) \quad (7.16)$$

If *R* is greater than unity, the ground state is predominantly d_z^2 and if it is less than unity it is $d_{x^2-y^2}$. In this case *R* is found to be 0.08 and so the ground state is of $d_{x^2-y^2}$ type.

7.4.2 Optical absorption studies:

In an octahedral crystal field the ^2D ground state of the Cu(II) ion with d^9 configuration splits into a triplet $^2T_{2g}$ and a doublet ^2E_g, the latter being lower. All the broad spin absorption bands are related to the transition between the levels derived from $2D \rightarrow {}^2E_g + {}^2T_{2g}$. The ground state ^2E_g is often found to split under Jahn-Teller effect, which causes distortion in the octahedral symmetry. In a tetragonally distorted octahedral symmetry (C_{4v}), ^2E_g split into $^2B_{1g}$ (corresponds to $d_{x^2-y^2}$ orbital) and $^2A_{1g}$ (corresponds to d_z^2 orbital) while the $^2T_{2g}$ splits into $^2B_{2g}$ (corresponds to d_{xy} orbital) and ^2E_g (corresponds to d_{yz} and d_{xz} orbital levels). The energy levels of different terms in tetragonal field are given in the literature [41] and therefore, three bands are expected for a Cu(II) complex [42,43]. The optical absorption spectrum of the Cu(II)/AMMZ sample is shown in Fig. 7.8. Since the spectrum consists of two bands, the site symmetry of Cu(II) is presumed to be D_{4h}. The bands in the range 5000 – 15000 cm^{-1} are characteristic of d-d transitions in Cu(II) systems. The broad band at 13793 cm^{-1} is characteristic of the Cu(II) ion in tetragonal distorted octahedral symmetry. Accordingly this broad band is assigned to $^2B_{1g} \rightarrow {}^2B_{2g}$. 10Dq = 13,793 cm^{-1}. The strong band at 37,454 cm^{-1} is assigned to a charge transfer band which usually occurs in the range of 35,000 – 50,000 cm^{-1}.

7.4.3 FT – IR Spectral studies:

FT-IR spectra of Cu(II) doped AMMZ recorded at room temperature is given in Fig. 7.9. It shows the bands in the regions of 3000 – 3600; 2700 – 3200; 1050 – 2300 and 600 – 1100 cm^{-1}. The bands at 3000 – 3600 cm^{-1} are assigned to – OH, at 2700 – 3200 cm^{-1} are assigned to -OH_2, at 1050 – 2300 cm^{-1} are assigned to C=O, at 600 – 1100 cm^{-1} are assigned to Zn–OH_2 [44]. Observed FT-IR bands and their tentative assignment for Cu(II) doped AMMZ are shown in Table 7.6. However, this spectrum is helpful in suggesting that no structural changes took place in the host lattice when a small amount of paramagnetic Cu(II) was incorporated into the lattice.

7.4.4 Powder XRD Studies:

Powder XRD pattern of Cu(II) doped AMMZ at room temperature is shown in Fig. 7.10. According to powder XRD measurements [45], Cu(II) doped AMMZ powder sample has identical lattice parameters as single crystal XRD parameters of AMMC [24]. The lattice parameters are tabulated in Table 7.7 with the single crystal XRD parameters of AMMC. It is clear from the Table 7.7 that the lattice parameters of Cu(II) doped AMMZ matched with reported values of copper complex, confirming that the zinc complex is isomorphic with copper complex and the low dopant concentration of the Cu(II) in AMMZ does not alter the symmetry of the host lattice.

7.5 Conclusion:

The EPR investigation of Cu(II) doped AMMZ single crystal studied at 300 K indicates that a number of impurity sites in the crystal is found to be independent of concentration and shows only one type of impurity in the crystal and that it enters the lattice substitutionally. The angular variation of the EPR spectra reveals that Cu(II) ion has been substituted at Zn(II) ion site. An important observation is that the parallel component of copper hyperfine value ($A_{\parallel}$) has been reduced considerably and this has been explained by considering an admixture of excited d_{z^2} state with $d_{x^2-y^2}$ ground state. In addition, the RT powder EPR spectrum suggests a typical $d_{x^2-y^2}$ ground state for Cu(II) ion. A reduced $A_{\parallel}$ value and observed in-plane anisotropy indicate a reduction in the site symmetry. The powder EPR spectrum recorded at liquid nitrogen temperature does not show any changes compared with room temperature spectrum. The Fermi-contact parameter κ and dipolar interaction parameter P have also been calculated and the co-valency of the metal-ligand bond is deduced as 84 %. From the observed spin Hamiltonian parameters, the admixture coefficients of the ground state have been calculated. The optical spectrum confirms the

distorted octahedral symmetry and EPR results reveals that the copper (II) is of tetragonally elongated symmetry. Zn–O, Zn–OH_2, -OH and O–C=O molecular bonds are confirmed by FT-IR. Powder XRD confirms the formation of the lattice AMMZ.

References:

[1] R. Tapramaz, B. Karabulut, F. Koksal, J. Phys. Chem. Solids, 61 (200) 1367.

[2] S. Dhanuskodi, S. Manikandan, Ferroelectrics, 234 (1999) 183.

[3] B.L. Silver, D. Getz, J. Chem. Phys., 61 (1974) 638.

[4] M.J. Riley, M.A. Hitchman, A.W. Mohammed, J. Chem. Phys., 87 (1987) 3766.

[5] C.P. Keijizers, T. Jension, E. de Boer, G. Van kalkeren, J. Magn. Reson., 52 (1983) 211.

[6] T.K. Kundn, P.T. Manoharan, Chem. Phys. Lett., 241 (1995) 627.

[7] P. Sambasiva Rao, A.K. Viswanath, S. Subramanian, Spectrochim. Acta, A48 (1992) 1745.

[8] S.N. Rao, Y.P. Reddy, P. Sambasiva Rao, Solid State Commun., 78 (1991) 1025.

[9] R.M. Krishna, J.L. Rao, S.V. Lakshman, J. Radiat. Eff. Defects Solids, 132 (1994) 67.

[10] R. Murugesan, S. Subramanian, Mol. Phys., 52 (1984) 129.

[11] R. Murugesan, S. Subramanian, J. Magn. Reson., 16 (1974) 82.

[12] H.A. Jahn, E. Teller, Proc. R. Soc. Lond., 161A (1937) 220.

[13] P. Sambasiva Rao, T.M. Rajendiran, R. Venkatesan, N. Madhu, A.V. Chandrasekar, B.J. Reddy, Y.P. Reddy, R.V.S.S.N. Ravikumar, Spectrochim. Acta, A57 (2001) 2781.

[14] N. Madhu, A.V. Chandrasekar, B.J. Reddy, Y.P. Reddy, R.V.S.S.N. Ravikumar, P. Sambasiva Rao, Indian J. Chem., 38A (1999) 590.

[15] P. Sambasiva Rao, S. Subramanian, J. Magn. Reson., 22 (1976) 191.

[16] S.K. Hoffmann, J. Goslar, W. Hilczer, M.A. Augustyniak-Jablokow, J. Phys.: Condens. Matter, 13 (2001) 707.

[17] D. Getz, B.L. Silver, J. Chem. Phys., 61 (1974) 630.

[18] D. Srinivas, M.B.V.L.N. Swamy, S. Subramanian, Mol. Phys., 57 (1986) 55.

[19] J. Chandrasekhar, S. Subramanian, J. Magn. Reson. 16 (1974) 82.

[20] M.A. Augustyniak-Jablokow, Yu.V. Yablokov, Solid State Commun., 115 (2000) 439.

[21] M.A. Augustyniak-Jablokow, J. Phys. Chem. Solids, 62 (2001) 1319.

[22] M.A. Hitchman, V. Maaskant, J. Van der Plas, C.J. Simmons, H. Stratemeier, J. Am. Chem. Soc., 121 (1999) 1488.

[23] E. Poonguzhali, R. Srinivasan, R.V.S.S.N. Ravikumar, A.V. Chandrasekhar, B.J. Reddy, Y.P. Reddy, P. Sambasiva Rao, Phys. Scr., 66 (2002) 391.

[24] J. Pasan, J. Sanchiz, F. Lloret, M. Julve, C. Ruiz-Perez, Cryst. Eng. Comm., 9 (2007) 478.

[25] EPR-NMR Program devoleped by F. Clark, R.S. Dickson, B.D. Fulton, J. Isoya, A. Lent, D.G. McGavin, M.J. Mombourquette, R.H.D. Nuttall, P.S. Rao, H. Rinnerberg, W.C. Tennant, J.A. Well, University of Saskatchewan, Saskatoon, Canada, 1996.

[26] D. Attansio, J. Magn. Reson., 26 (1977) 81.

[27] D. Attansio, G. Dessy, V. Fares, J. Chem. Soc., Dalton Trans., (1979) 28.

[28] J.A. Guckert, M.D. Lowery, E.J. Solomon, J. Am. Chem. Soc., 117 (1995) 2817.

[29] J.D. Swalen, B. Johnson, H.M. Gladney, J. Chem. Phys., 52 (1970) 4078.

[30] K.E. Falk, F. Ivanova, B. Roos, T. Vanngavel, Inorg. Chem., 9 (1970) 556.

[31] J.H. Van Vleck, Phys. Rev., 41 (1932) 208.

[32] D. Kivelson, R. Neiman, J. Chem. Phys., 35 (1961) 149.

[33] K.K. Mothilal, C. Karunakaran, P. Sambasiva Rao, R. Murugesan, Spectrochim. Acta, A59 (2003) 3337.

[34] A.M.F. Benial, V. Ramakrishnan, R. Murugesan, Spectochim. Acta, A56 (1976) 2775.

[35] S. Mithira, B. Natarajan, S. Deepa, R.V.S.S.N. Ravikumar, P. Sambasiva Rao, J. Mol. Struct., 839 (2007) 2.

[36] I. Sougandi, R. Venkatesan, P. Sambasiva Rao, Spectrochim. Acta, A60 (2004) 2653.

[37] P.N. Selvakumar, B. Natrajan, P. Sambasiva Rao, P. Subramanian, Cryst. Res. Technol., 43 (2008) 857.

[38] D.P. Pandian, C. Muthukrishnan, R. Murugesan, Cryst. Res. Technol., 35 (2000) 595.

[39] K. Chinnam Naidu, C. Shiyamala, S. Mithira, B. Natarajan, R. Venkatesan, P. Sambasiva Rao, Radiat. Eff. Defects Solids, 160 (2005) 225.

[40] C. Shiyamala, R. Venkatesan, P.S. Rao, Solid State Commun., 128 (2003) 137.

[41] A.B.P. Lever, "Inorganic Electronic Spectroscopy", 2nd Ed., Elsevier, Amsterdam, 1984.

[42] M.A. Hitchman, P.J. Cassidy, Inorg. Chem., 18 (1975) 1745.

[43] M.A. Hitchman, Trans. Met. Chem., 9 (1985) 1.

[44] K. Nakamoto, "Infrared Spectra of Inorganic and Coordination Compounds", Wiley, New York, 1963.

[45] B.D. Cullity, "Elements of X-ray Diffraction", Addison Wesley, Massachusetts, USA, 1978.

STRUCTURAL INVESTIGATION OF CU(II) ION DOPED IN HEXAAQUOZINC DIAQUOBIS(MELONATO)ZINCATE HOST BY EPR STUDY

8.1 Introduction:

Electron Paramagnetic Resonance (EPR) spectroscopy has been used extensively as a powerful tool to identify the characteristics of transition metal ions. This kind of studies gives valuable information about the site symmetry of the transition metal ions. As Cu(II) ion is a simplest probe to enter a host lattice easily, an idea about the ground state of the ion, the distortion, the position of the paramagnetic impurity and so on [1-5] can be obtained from a single crystal EPR study. EPR study of Cu(II) doped single crystal are highly suitable to investigate various types of Jahn-Teller distortions, such as static, dynamic and tunneling, which in turn will assist, to obtain the ground state in low symmetry environments [6-10]. If the crystal symmetry is octahedral, then the ground state of Cu(II) ion has six electrons in the low lying t_{2g} orbital, where as the doubly degenerate e_g orbital accommodates the other three electrons. The orbital degeneracy can be lifted either by a lowering in symmetry arising due to charge compensating vacancies, crystalline field, etc. or by Jahn-Teller distortion [11]. In that situation, the ground state will be either $d_{x^2-y^2}$ or d_{z^2}. In most of the cases, the symmetry is low enough to remove the degeneracy and the unpaired electron was found in $d_{x^2-y^2}$ ground state corresponding to axial elongation [12]. However, a few systems were known, which exhibit axial compression corresponding to d_{z^2} ground state [10, 12]. The diamagnetic host ions possess a closed outer electronic shell, thereby causing the local symmetry of the host lattice to be high. When the Cu(II) ions are introduced in such host lattices, substituting for the diamagnetic ions, local distortion will take place, because of the mismatch of Cu(II) ion size to that of the host ions and dynamic effects such as the Jahn-Teller effect [13].

8.2 Materials and Methods:

8.2.1 Preparation of single crystal of Cu(II) doped $[Zn(H_2O)_6][Zn(mal)_2(H_2O)_2]$:

Malonic acid, basic zinc(II) carbonate and zinc acetate were purchased from commercial sources and used as received. Solid zinc(II) basic carbonate was added to an aqueous solution of malonic acid under continuous stirring. The suspension was heated at 50 – 60 ºC until a clear solution was obtained. This solution was filtered and mixed with an aqueous solution of the zinc(II) acetate. The solution was concentrated to 25 cm^3 in a steam bath and then it was allowed to grow single crystals doped with five different concentrations

(0.5, 1.0, 1.5, 2.0 and 5.0 %) of copper sulfate at room temperature. Well shaped, light blue color single crystals suitable for EPR studies were obtained within fifteen days.

8.2.2 EPR Measurements:

The EPR studies are performed on a JEOL JES-TE100 ESR spectrometer operating at X-band frequencies, having a 100 kHz field modulation to obtain the first-derivative EPR spectrum at room temperature. 1,1-Diphenyl-2-picrylhydrazyl (DPPH) with a g-value of 2.0036 is used as a reference for g-factor calculations.

8.2.3 UV-Visible, FT-IR, Powder XRD Measurements:

UV – Vis absorption spectrum of the powder sample in the range of 200 – 1200 nm is recorded on a Varian Cary 5000 ultraviolet-visible (UV-Vis) near-infrared spectrophotometer. FT - IR spectra of doped and undoped materials in the frequency range of 4000-400 cm^{-1} are recorded on a Shimadzu FT-IR-8300/8700 spectrometer with the samples prepared as KBr pellets. The powder XRD studies are carried out for doped and undoped materials on a PANalytical X'pert PRO diffractometer with Cu Kα radiation of wavelength λ = 0.15406 nm, 2θ values between 5-75°, at room temperature.

8.3 Crystal structure:

$[Zn(H_2O)_6][Zn(mal)_2(H_2O)_2]$ is isostuctural with $[Zn(H_2O)_6][Cu(mal)_2(H_2O)_2]$ [14]. It belongs to triclinic crystal system with space group $P\bar{1}$, having unit cell parameters a = 0.5274 nm, b = 0.7504 nm, c = 1.0314 nm, α = 106.92, β = 99.15, γ = 95.81 and Z = 2. The coordination polyhedron of the copper atom in the anionic unit $[Cu(mal)_2(H_2O)]^{2-}$ is that of an elongated octahedral CuO_6. Four carboxylate oxygens from two bidentate malonate ligands build the equatorial plane, whereas two water molecules occupy the axial sites. The zinc(II) ion in the cationic units $[Zn(H_2O)]^{2+}$ is coordinated to six water molecules with a slightly distorted octahedral geometry.

8.4. Result and Discussion:

8.4.1 EPR studies:

The Cu(II) ion ($3d^9$, ^2D) can be treated as a $3d^1$ hole configuration with effective electron spin S = 1/2 , and nuclear spin I = 3/2 for both natural copper isotopes. Among the five concentration crystals (0.5, 1.0, 1.5, 2.0 and 5.0 %), the low concentrations 0.5, 1.0 and 1.5 % are gave very weak resonance lines, which are difficult to follow during crystal rotations. In case of crystals with 5.0 % dopant concentration, the lines are broad due to dipole-dipole interactions. Hence, in the present study, crystals with 2.0 % dopant

concentration have been used for single crystal EPR studies, due to well resolved hyperfine resonance lines. However, for IR, optical and powder XRD studies, sample with 5.0 % concentration is used. Good shape and size single crystals of Cu(II) doped HZBMZ are selected to record EPR spectrum for every 10 degree angle by rotating the crystal in three mutually orthogonal planes namely a*b, a*c* and bc* at room temperature. Axis *c** is perpendicular to the crystal axis *b* in the *bc* crystal plane and axis *a** is orthogonal to axes *b* and *c**. Initially, the crystal rotations are performed at RT to assess the type of JT effect, if any. It is generally known that if the EPR lines are invariant for single crystal rotations at RT, it may correspond to dynamic JT or Tunneling [15, 16]. In contrast, if the copper hyperfine lines are not well resolved, but show angular dependence it corresponds to static JT. Finally, if the system behaves as anisotropic and with well resolved hyperfine lines at RT, no JT is to be considered. A single crystal EPR spectra of Cu(II)/HZBMZ in a*c* plane at two different orientations are given in Fig. 8.1. For a Cu(II) system, S = 1/2 and I = 3/2 for ^{63}Cu and ^{65}Cu. Hence a four line spectrum is expected for a single site of Cu(II). It is clear from these spectra that the hyperfine lines are not well resolved, but show anisotropy. Hence this system may correspond to static JT. The EPR spectrum of Cu(II) ion doped HZBMZ single crystal at RT is shown in Fig. 8.2 when the applied magnetic field (B) is parallel to axis c*. Fig. 8.3 shows the single crystal EPR spectrum of Cu(II) doped in HZBMZ when B is parallel to axis a*. Crystal rotations are carried out in the three mutually orthogonal planes and isofrequency plots in *a*c**, *bc** and a*b planes are shown in Figs. 8.4-8.6 respectively. During crystal rotations, only one set of four lines are observed, even though the unit cell contains four molecules. A close look at the spectra indicates four lines. At few orientations spectra is not resolved. This indicates non-uniform averaging of the hyperfine lines at room temperature. In order to plot isofrequency diagrams, whenever the lines are not completely resolved, we have assumed that the line width is approximately equal to the sum of four hyperfine lines. Even though, this may give an error, they are really useful to get the spin Hamiltonian parameters at RT to understand the nature of the distortion.

8.4.1.1 Calculation of spin-Hamiltonian parameters:

The hyperfine lines of Cu(II) in HZBMZ are fitted to the following spin Hamiltonian with orthorhombic symmetry.

$$H = g_{xx}\beta B_x S_x + g_{yy}\beta B_y S_y + g_{zz}\beta B_z S_z + A_{xx} S_x I_x + A_{yy} S_y I_y + A_{zz} S_z I_z \qquad (8.1)$$

Here the symbols have their usual meaning. The quadrupole and nuclear Zeeman interactions are ignored. By making use of program EPR-NMR [17], the spin Hamiltonian parameters g

and *A* are calculated and are given in Table 8.1 along with their direction cosines respectively. The direction cosines of the principal values of g and A matrices match well with each other, further confirmed by having the maxima and minima at the same angle in the isofrequency plots. Generally these values are compared with the direction cosines of Zn-O bond directions of the host lattice, to get information about the location of the dopant. From the crystal data of the host lattice, the direction cosines of the Zn-O bond directions have been calculated and given in Table 8.2. A few set of spin-Hamiltonian parameters, taken from literature are given in Table 8.3, for comparison. The principal g and *A* matrix direction cosines match with the direction cosines of Zn–O bond directions, confirming that the Cu(II) ion has entered the lattice substitutionally. Using the *g* and *A* values obtained in the program EPR-NMR, the iso-frequency plots are simulated for *a*c**, *bc** and *a*b* planes and are also given in Figs. 8.4, 8.5 and 8.6 respectively. In these figures, solid lines correspond to theoretical variation and the solid circles correspond to the experimental data. A good agreement is observed in both the planes, confirming the accuracy of our calculated spin-Hamiltonian parameters.

The observed rhombicity of the g tensor (and also *A* tensor) can be explained in terms of the highly distorted coordination geometry around the Cu(II) and it suggests that the ground state has considerable admixture of the exited state [21]. Symmetry allowed mixing of the d_z^2 wave function predominantly in the $d_{x^2-y^2}$ ground state results in the effect that $g_{zz} > g_{xx} > g_{yy}$. The mixing coefficients determine the non-axiality of the g tensor [22] and the g values of the present system show a significant non-axiality.

8.4.1.2 Location of the impurity:

The location of the impurity can be detected by comparing the direction cosines of the principal values of *g* and *A* tensors with any of the metal-ligand bond directions (Zn–O). The direction cosines of *g*, and *A* are tabulated in Table 8.1 and that of metal- ligand bond direction cosine of HZBMZ crystal lattice are given in Table 8.2. It is evident from the table that one of the direction cosines of the principal g value is found to match fairly well with that of the metal – oxygen (Zn – O3w) bond direction. The deviation between these directions is around 6º. This suggests that the Cu(II) ion has entered the lattice substitutionally.

8.4.1.3 Polycrystalline spectrum:

In order to confirm the single crystal analysis, powder spectrum of the sample is recorded at room temperature and is given in Fig. 8.7. It clearly indicates the axially symmetric nature of the impurity. Due to large line width in powder spectrum, the

perpendicular component does not show further splitting, a common observation in most of the Cu(II) complexes. The *g* and *A* values have been calculated from this spectrum and are given in Table 8.3, along with the values for Cu(II) systems in other host lattices. Using these parameters and Bruker Simfonia program, the powder spectrum has been simulated and included in Fig. 8.7 itself. The agreement is very good and the values have matched well with the single crystal analysis. As the perpendicular hyperfine lines are not resolved and A_{zz} value deviates from single crystal data at room temperature in the powder spectrum, the sample is cooled to 77 K. The 77 K EPR spectrum of the powder sample does not show any change in *g* and *A* values and in resolution.

A close look at the hyperfine values indicates that one of the principal values (A_{zz}) is appreciably smaller than a generally observed value of $A_{\parallel}$ for a copper ion. A few systems, having a smaller A_{zz} hyperfine value, have been selected from the literature and are given in Table 8.3, for comparison. This low value of A_{zz} has been explained by considering the admixture of $d_{x^2-y^2}$ (ground state) with d_{z^2} (excited state) orbital and metal – ligand covalent character [23].

8.4.1.4 Admixture coefficients:

From g values, the coefficients of the d-orbital of the Kramers' doublet are determined. The $d_{x^2-y^2}$ orbital gets admixed with d_{xy}, d_{yz} and d_{xz}. The d_{z^2} gets admixed with d_{yz} and d_{xz}. The Kramers' doublet wave function for the ground state, given in the Chapter 7, which represents that if $a = 1$, the system has d_{z^2} ground state and lowest A_{zz} value and if $b = 1$, the system is in $d_{x^2-y^2}$ ground state and maximum hyperfine value. The constants *a*, *b*, *c*, *d* and *e* indicate the mixing of d-orbital brought about by metal spin – orbit coupling. In terms of admixture coefficients [16], the expression for the *g* and *A* values also are given in Chapter 7.

P is the gyromagnetic ratio of copper and its free ion value is 360×10^{-4} cm^{-1} and κ is the Fermi contact term, which is a measure of bonding effects on the Cu(II) in crystal lattice. Assuming that $d = -e$, the coefficients *a*, *b*, *c* and *d* have been calculated and given in Table 8.4. Using a similar procedure, the coefficients have been calculated for Cu(II)/AMMZ also and are included in Table 8.4, along with some other values. As expected, an increase in the coefficient of *a* is noticed whenever a decrease in hyperfine is observed.

8.4.1.5 Molecular orbital coefficients:

From the spin Hamiltonian parameters, the dipolar term (*P*) and Fermi contact term (κ) [24] are calculated using the equations (7.10-7.13) given in Chapter 7. The Fermi contact term κ is a measure of the polarization produced by the uneven distribution of d-electron

density on the inner core s-electron and it has been suggested [25] that 3d transition metal ions, κ = 0.3. The values of P and κ obtained are 0.032 cm^{-1} and 0.36 (by assuming axial symmetry taking the average value of g_{yy} and g_{zz} for $g_{\perp}$ and A_{yy} and A_{zz} for $A_{\perp}$).

From the equations (7.10-7.13) given in Chapter 7, P and κ have been calculated and are given in Table 8.5, along with some known values. The ratio of $P_{complex}$ to P_{free} ion is around 88 %, indicating the delocalization of the d-electron. The percentage of unpaired spin density on copper ion is 12 % and the remaining density is being distributed onto the ligands. The molecular orbital coefficient α^2, which gives a measure of covalent nature of σ-bonding is given as,

$$\alpha^2 = (A_{\parallel}/0.036) + (g_{\parallel} - 2.0023) + 3/7\,(g_{\perp} - 2.0023) + 0.04 \qquad (8.2)$$

α' can be evaluated from the normalization condition on the ground state orbital as

$$\alpha' = (1 - \alpha^2)^{1/2} + \alpha S \qquad (8.3)$$

where S is the overlap integral between $d_{x^2-y^2}$ orbital and normalized ligand orbital. The value of S is given as 0.076 for a copper complex with water ligands. The complex is found to be partially covalent in nature. These values are also given in Table 8.5. Value of β_1^2 which is a direct measure of the covalence of the in-plane π-bonding is calculated using the formula

$$g_{\parallel} = 2.0023 - 8\rho[\alpha\beta_1 - 1/2\,\alpha'(1 - \beta_1^2)^{1/2}T(n)] \qquad (8.4)$$

where $\rho = \lambda_0\,\alpha\beta_1/\Delta E$, T(n) is a function involving metal – ligand distance, hybridization constant (n) and effective nuclear charges for the ligand 2s, 2p orbitals and the metal 3d orbital. Assuming λ_0 = -828 cm^{-1} and T(n) = 0.220, the calculated values of the covalence parameters are

$$\alpha^2 = 0.809; \quad \alpha' = 0.505; \quad \alpha = 0.899; \quad \beta_1^2 = 0.221; \quad \beta_1 = 0.470;$$

The parameter α^2 describes the covalence of the σ bond between the metal and its ligands. It has a value of unity, if the bond is totally ionic and 0.5 if it is completely covalent. The present value of α^2 = 0.809 indicates moderate covalence for the in-plane σ bonding and β_1^2 = 0.221 indicates greater covalence for the in-plane π-bonding. Here it may be mentioned that β_1^2 is more sensitive to variations in covalence than α^2 and is therefore a better indicator of covalent character [31]. Yet, another parameter R, the ratio difference between second and third value to first and second values of the increasingly arranged g value is also calculated, which gives an idea about the ground state nature of the paramagnetic impurity on the host lattice.

$$R = (g_2 - g_3)/ (g_1 - g_2) \quad (8.5)$$

If *R* is greater than unity, the ground state is predominantly $^2A_1$ (d_z^2) and if it is less than unity it is $^2A_1$ ($d_{x^2-y^2}$). In the present study, *R* is equal to 0.53 suggesting the ground state to be $^2A_1$ ($d_{x^2-y^2}$) type. This data compares well with the other rhombic octahedral complexes, reported earlier.

8.4.2 Optical absorption studies:

In an octahedral crystal field the ^2D ground state of the Cu(II) ion with d^9 configuration splits into a triplet $^2T_{2g}$ and a doublet ^2E_g, the latter being lower. All the broad spin absorption bands are related to the transition between the levels derived from 2D → ^2E_g + $^2T_{2g}$. The ground state ^2E_g is often found to split under Jahn-Teller effect, which causes distortion in the octahedral symmetry. In a tetragonally distorted octahedral symmetry (C_{4v}), ^2E_g split into $^2B_{1g}$ (corresponds to $d_{x^2-y^2}$ orbital) and $^2A_{1g}$ (corresponds to d_z^2 orbital) while the $^2T_{2g}$ splits into $^2B_{2g}$ (corresponds to d_{xy} orbital) and ^2E_g (corresponds to d_{yz} and d_{xz} orbital levels). The energy levels of different terms in tetragonal field are given in the literature [32]. The powder optical absorption spectrum of the Cu(II) in HZBMZ recorded at room temperature is shown in Fig. 8.8. It consists of two bands at 40,000 and 12,106 cm^{-1}. The strong band at 40,000 cm^{-1} is assigned to charge transfer band, which usually occurs in the range of 35,000 – 50,000 cm^{-1}. The bands in the range 5000 – 15000 cm^{-1} are characteristic of d-d transitions in Cu(II) systems. The broad band at 12,106 cm^{-1} is characteristic of the Cu(II) ion in tetragonal distorted octahedral symmetry. Accordingly, this broad band is assigned to $^2B_{1g} \rightarrow {}^2B_{2g}$. 10Dq = 12,106 cm^{-1}.

8.4.3 FT – IR Spectral studies:

FT-IR spectra of pure and Cu(II) doped HZBMZ recorded at room temperature is given in Fig. 8.9. It shows the bands in the regions of 3000 – 3600; 2700 – 3200; 1050 – 2300 and 600 – 1100 cm^{-1}. The bands at 3000 – 3600 cm^{-1} are assigned to –OH, bands at 2700 – 3200 cm^{-1} are assigned to -OH_2, bands at 1050 – 2300 cm^{-1} are assigned to C=O and bands at 600 – 1100cm^{-1} are assigned to Zn–OH_2 [33]. Observed FT-IR bands and their tentative assignment for Cu(II) doped HZBMZ are shown in Table 8.6. Hence, this spectrum is helpful in suggesting that no structural changes took place in the host lattice when a small amount of paramagnetic Cu(II) was incorporated into the lattice.

8.4.4 Powder XRD studies:

Powder XRD for Cu(II) doped HZBMZ recorded at room temperature is shown in Fig. 8.10. According to powder XRD measurements [30], Mn(II) doped HZBMZ powder sample has identical lattice parameters as HZBMZ powder sample, as expected from the low

impurity concentration. The lattice parameters are tabulated in Table 8.7 with the single crystal XRD parameter of HZBMC [14]. It is clear from the table that the parameters of HZBMZ and Mn(II) doped HZBMZ matched with reported values of copper complex [14], confirming that the zinc complex is isomorphic with copper complex and the low dopant concentration of Mn(II) in HZBMZ does not alter the symmetry of host lattice.

8.5 Conclusion:

The EPR investigation of Cu(II) doped HZBMZ single crystal studied at 300K indicates that only one type of impurity in the crystal and that it enters the lattice substitutionally. The angular variation of the EPR spectra reveals that Cu(II) ion have been incorporated at substitutional site. An important observation is that the parallel component of copper hyperfine value ($A_{\parallel}$) has been reduced considerably and this has been explained by considering an admixture of excited d_z^2 state with $d_{x^2-y^2}$ ground state. In addition, the RT powder EPR spectrum suggests a typical $d_{x^2-y^2}$ ground state for Cu(II) ion. A reduced $A_{\parallel}$ value and observed in-plane anisotropy indicate a reduction in the site symmetry. Not well resolved but anisotropic hyperfine lines of the spectra confirming that this system containing static JT. The powder EPR spectrum recorded at liquid nitrogen temperature does not show any changes compared with room temperature spectrum. The Fermi-contact parameter κ and dipolar interaction parameter P have also been calculated and the co-valency of the metal-ligand bond is deduced as 88 %. From the observed spin Hamiltonian parameters, the admixture coefficients of the ground state have been calculated. The optical spectrum confirms the octahedral symmetry and EPR results reveals that the copper (II) is of tetragonally elongated symmetry. Zn–O, Zn–OH_2, -OH and O–C=O bonds are confirmed by FT-IR. Powder XRD confirms the formation of the lattice HZBMZ.

References:

[1] R. Tapramaz, B. Karabulut, F. Koksal, J. Phys. Chem. Solids, 61 (2000) 1367.

[2] S. Dhanuskodi, S. manikandan, Ferroelectrics, 234 (1999) 183.

[3] B.L. Silver, D. Getz, J. Chem. Phys., 61 (1974) 638.

[4] M.J. Riley and M.A. Hitchman, A.W. Mohammed, J. Chem. Phys., 87 (1987) 3766.

[5] C.P. Keijizers, T. Jension, E. deBoer, G. Van Kalkeren, J. Magn. Reson., 52 (1983) 211.

[6] P. Sambasiva Rao, T.M. Rajendiran, R. Venkatesan, N. Mathu, A.V. Chandrasekhar, B.J. Reddy, Y.P. Reddy, R.V.S.S.N. Ravikumar, Spectrochem. Acta, A57 (2001) 2781.

[7] P. Sambasiva Rao, S. Subramanian, J. Magn. Res., 22 (1976) 191.

[8] P.S. Rao, A.K. Viswanath, S. Subramanian, Spectrochem. Acta, A48 (1992) 1745.

[9] N. Madhu, A.V. Chandrasekhar, B.J. Reddy, Y.P. Reddy, R.V.S.S.N. Ravikumar, P. Sambasiva Rao, Indian J. Chem. A, 38 (1999) 590.

[10] R. Murugesan, S. Subramanian, Mol. Phys., 52 (1984) 129.

[11] H.A. Jahn, E. Teller, Proc. R. Soc. Lond., A161 (1937) 220.

[12] R. Murugesan, S. Subramanian, J. Magn. Res., 16 (1974) 82.

[13] T.K. Kundu, P.T. Manoharan, Chem. Phys. Lett., 241 (1995) 627.

[14] Y.R. Martin, J. Sanchiz, C.R. Perez, F. Lloret, M. Julve, Cryst. Eng. Comm., 4 (2002) 631.

[15] C.P. Keijzers, T. Jension, E. de Boer, G. Van Kalkeren, J. Magn. Reson., 52 (1983) 211.

[16] D. Srinivas, M.B.V.L.N. Swamy, S. Subramanian, Mol. Phys., 52 (1986) 55.

[17] EPR-NMR Program devoleped by F. Clarck, R. S. Dickson, B.D. Fulton, J. Isoya, A. Lent, D.G. McGavin, M.J. Mombourquette, R.H.D. Nuttall, P.S. Rao, H. Rinnerberg, W.C. Tennant, J.A. Well, University of Saskatchewan, Saskatoon, Canada, 1996.

[18] K.K. Mothilal, C. Karunakaran, P. Sambasiva Rao, R. Murugesan, Spectrochim. Acta, A59 (2003) 3337.

[19] A.M.F. Benial, V. Ramakrishnan, R. Murugesan, J.Magn. Reson., 22 (1976) 191.

[20] S.Mithira, B. Natarajan, S. Deepa, R.V.S.S.N. Ravikumar, P. Sambasiva Rao, J. Mol. Struct., 839 (2007) 2.

[21] I.S. Ahuja, S. Tripathi, Spectrochim. Acta, A47 (1991) 637.

[22] S.K. Hoffmsnn, J. Goslar, W. Hilczer, R. Kaszynski, M.A. Augustynaik-Jablokow, Solid State Commun., 117 (2001) 333.

[23] D. Attansio, J.Magn. Reson., 26 (1977) 81.

[24] K.E. Falk, F. Ivanova, B. Roos, T. Vanngavel, Inorg. Chem., 9 (1970) 556.

[25] J.H. Van Vleck, Phys. Rev., 41 (1932) 28.

[26] C. Shiyamala, R. Venkatesan, P.S. Rao, Solid State Commun., 128 (2003) 137.

[27] D. Attansio, G. Dessy, V. Fares, J. Chem. Soc., Dalton Trans., (1979) 28.

[28] J.D. Swalen, Johnson, H.M. Gladney, J. Chem. Phys., 52 (1970) 4078.

[29] D.P. Pandian, C. Muthukrishnan, R. Murugesan, Cryst. Res. Technol., 35 (2000) 595.

[30] K. Chinnamnaidu, C. Shiyamala, S. Mithira, B. Natarajan, R.Venkatesan, P. Sambasiva Rao, Radiat. Eff. Defects Solids, 160 (2005) 225.

[31] D. Kivelson, R. Neiman, J. Chem. Phys., 35 (1961) 149.

[32] A.B.P. Lever, "Inorganic Electronic Spectroscopy", 2nd Ed., Elsevier, Amsterdam, 1984.

[33] K. Nakamoto, "Infrared Spectra of Inorganic and Coordination Compounds", Wiley, New York, 1963.

[34] B.D. Cullity, "Elements of X-ray Diffraction", Addison Wesley, Massachusetts, USA, 1978.

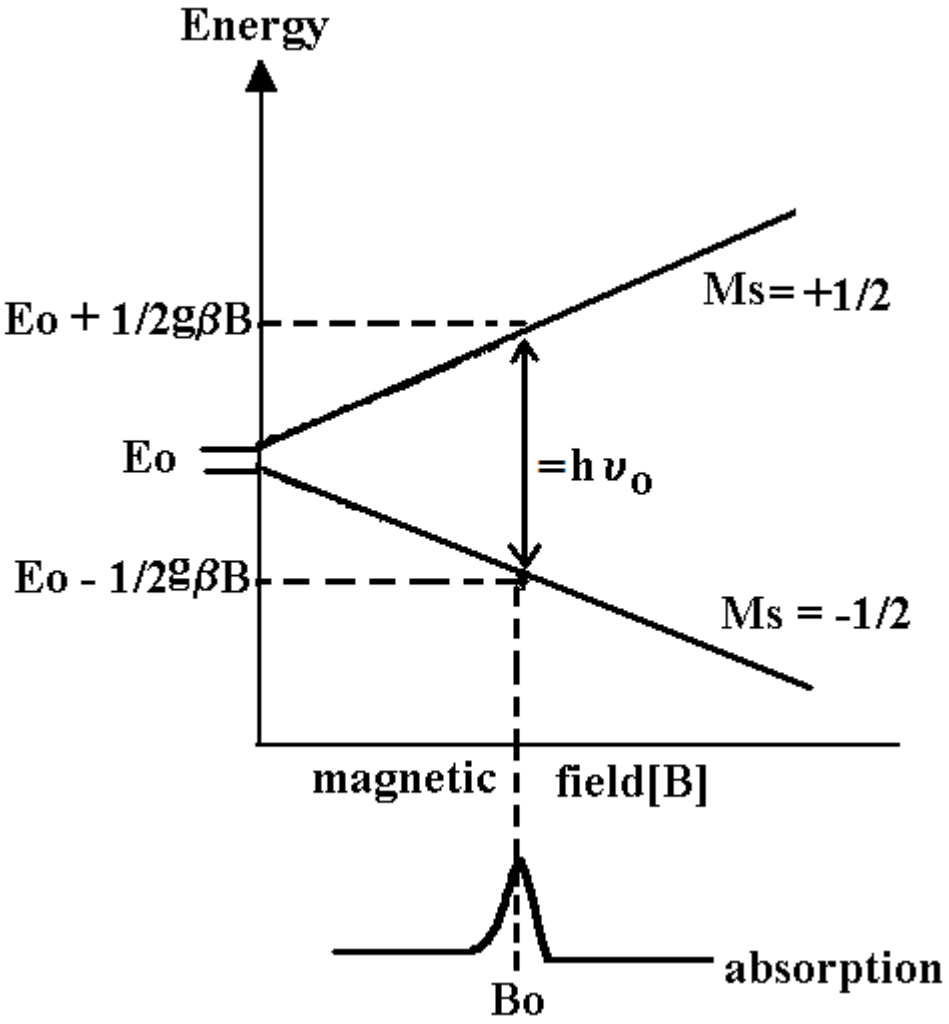

Fig. 1.1 Representation of the resonance condition in the frequency mode.

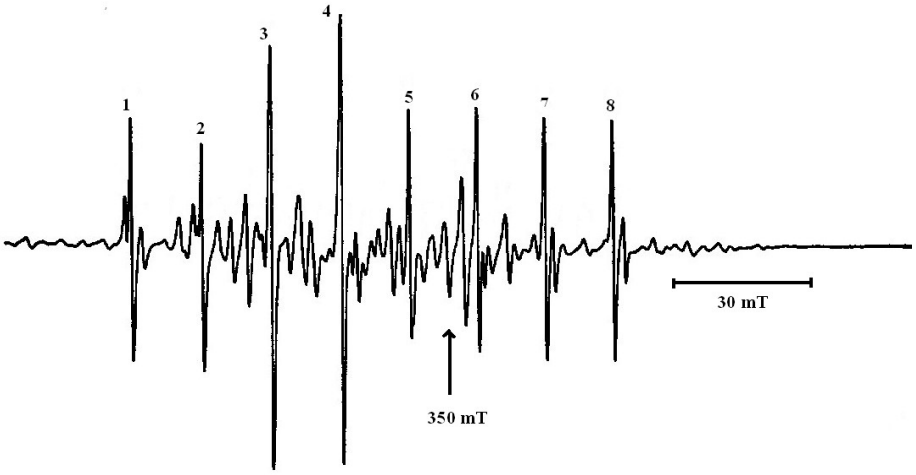

Fig. 3.1 Single crystal EPR spectrum of VO(II)/ALMZ when the magnetic field (B) is parallel to axis c*. Frequency = 9.08396 GHz. The strong resonance lines are marked by the number (1-8). Because of the low intensity, the lower intensity peaks are not analyzed.

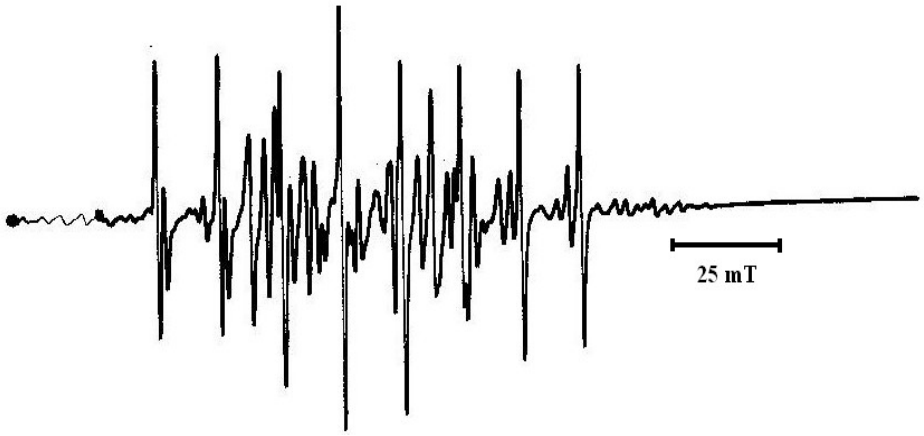

Fig. 3.2 Single crystal EPR spectrum of VO(II)/ALMZ when the B is 40^{o} away from axis c*. Frequency = 9.08606 GHz.

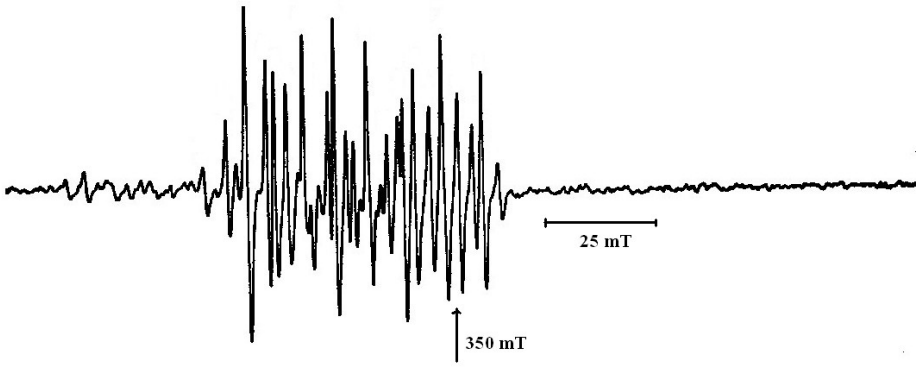

Fig. 3.3 Single crystal EPR spectrum of VO(II)/ALMZ when the B is parallel to axis a*. Frequency = 9.08381 GHz.

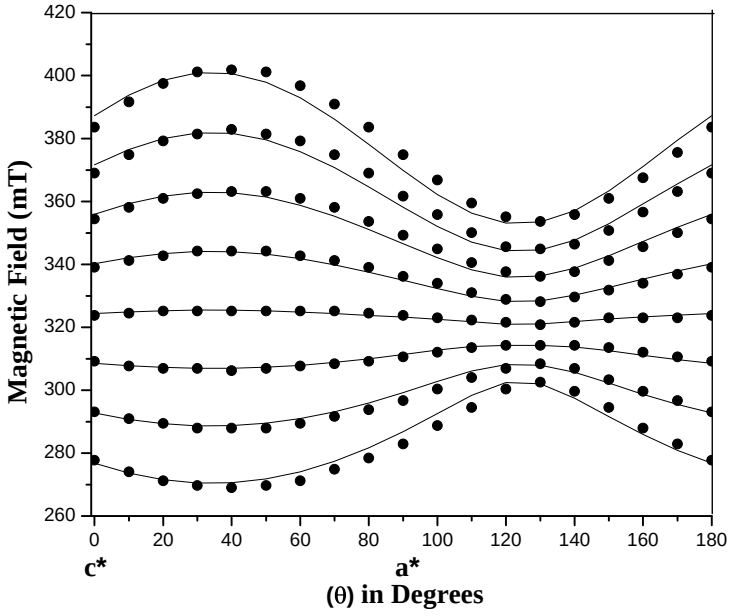

Fig. 3.4 Isofrequency plot of VO(II)/ALMZ in a*c* plane at room temperature. Solid circles indicate experimental values; solid lines correspond to theoretical values. Frequency = 9.08606 GHz.

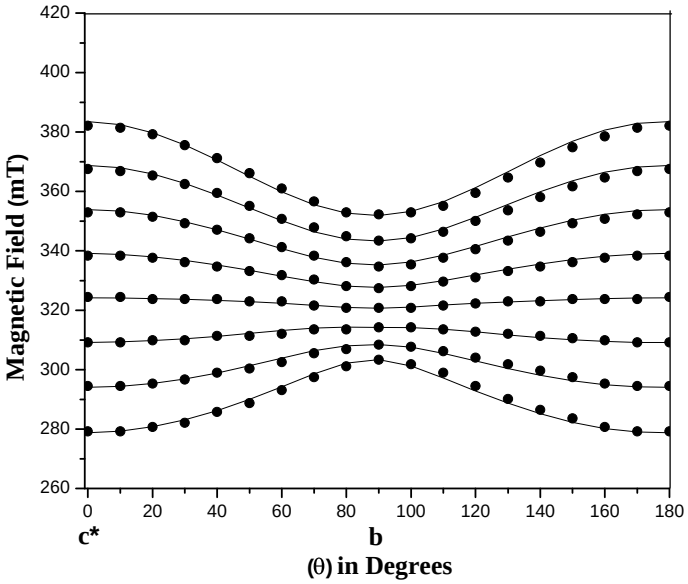

Fig. 3.5 Isofrequency plot of VO(II)/ALMZ in bc* plane at room temperature. Solid circles indicate experimental values; solid lines correspond to theoretical values. Frequency = 9.08396 GHz.

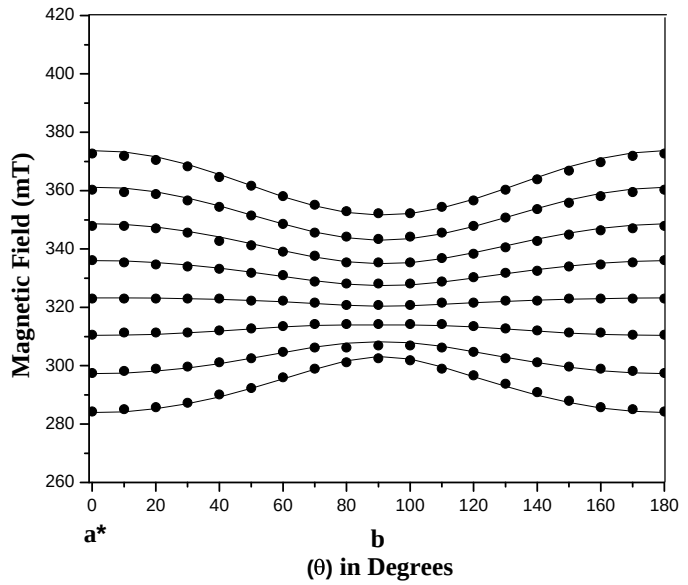

Fig. 3.6 Isofrequency plot of VO(II)/ALMZ in a*b plane at room temperature. Solid circles indicate experimental values; solid lines correspond to theoretical values. Frequency = 9.08381 GHz.

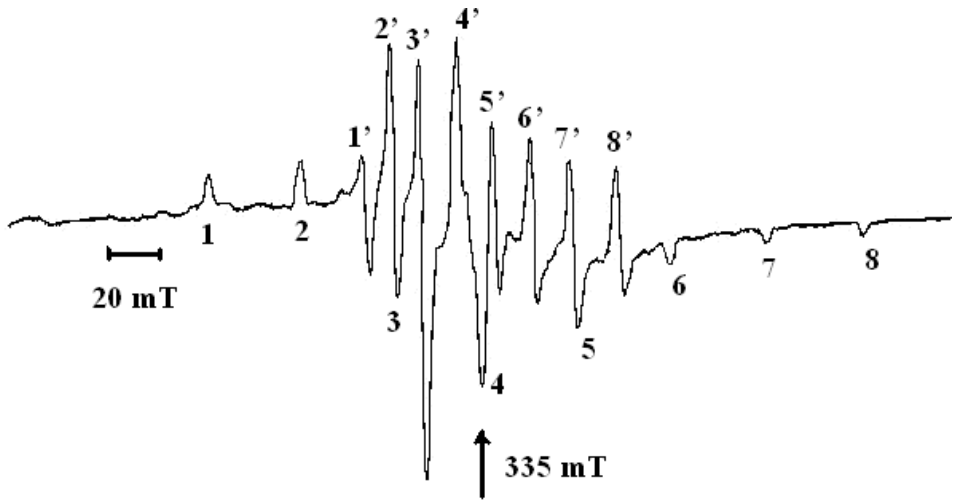

Fig. 3.7 Powder EPR spectrum of VO(II)/ALMZ at room temperature. The parallel components are marked by 1 to 8 and the perpendicular components are indicated by 1' to 8'. Top figure corresponds to experimental one, whereas bottom one is the simulated using parameters given in the text. Frequency = 9.38682 GHz.

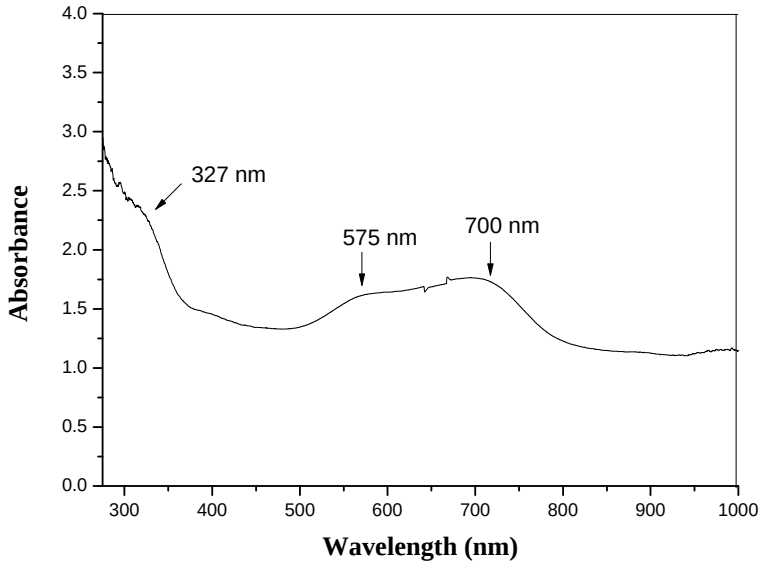

Fig. 3.8 Optical absorption spectrum of VO(II)/ALMZ at room temperature.

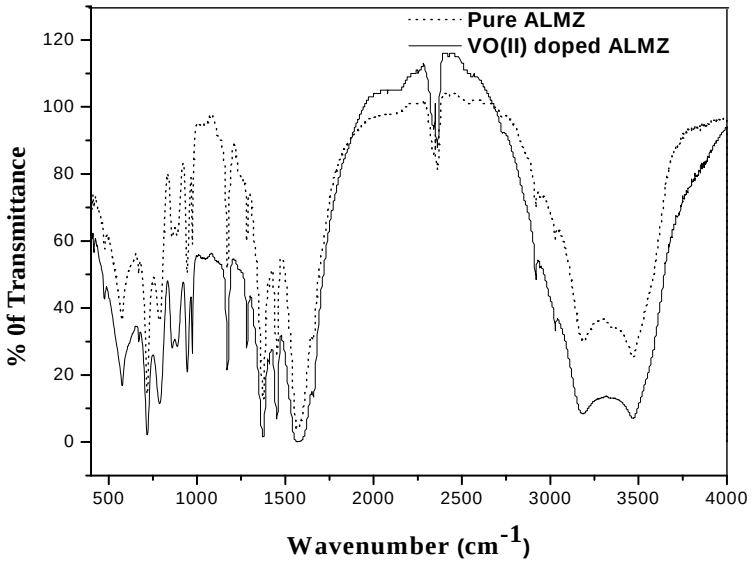

Fig. 3.9 FT-IR Spectrum of VO(II)/ALMZ at room temperature. Dotted and solid lines correspond to pure ALMZ and VO(II) doped ALMZ respectively.

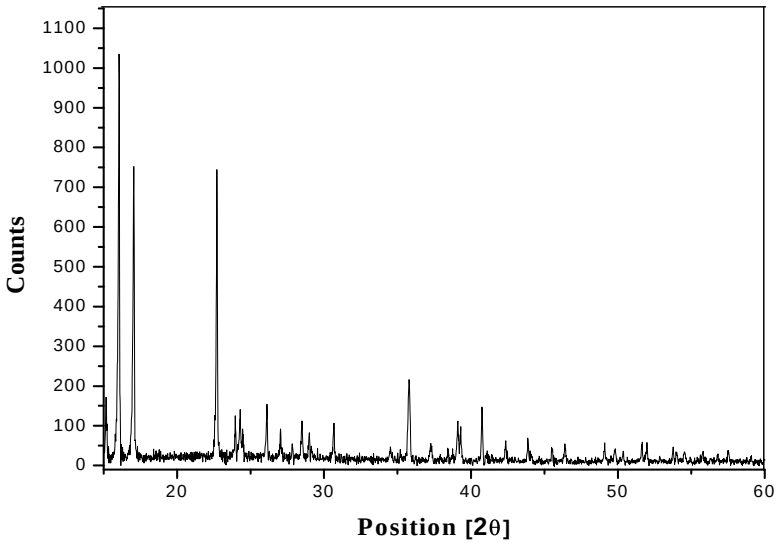

Fig. 3.10 Powder XRD pattern of VO(II)/ALMZ at room temperature.

Table 3.1 Spin Hamiltonian parameters obtained from single crystal rotations for VO(II)/ALMZ using program EPR-NMR [21].

			Principal Values	Direction cosines a*	b	c*
g matrix						
1.957	-0.001	-0.020	1.976	0.2036	-0.9679	-0.1473
	1.976	-0.000	1.973	-0.7461	-0.2508	0.6168
		1.949	1.933	-0.6339	-0.0157	-0.7732
A matrix (mT)						
11.39	0.07	5.39	7.01	-0.2298	-0.9505	0.2093
	6.79	0.20	6.77	-0.7402	0.3103	0.5966
		13.61	18.01	0.6319	0.0178	0.7748
Powder spectrum:						
$g_{\parallel} = 1.931$		$g_{\perp} = 1.985$	$A_{\parallel} = 19.94$ mT		$A_{\perp} = 7.84$ mT	

Table 3.2 Direction cosines of Zn-O bonds and Li-O bonds for ALMZ, obtained from crystallographic data [20].

Zn-O, Li-O bonds in ALBZ	Direction cosines a*	b	c*
Zn-O(1)	0.5639	0.4699	0.6791
Zn-O(11)	-0.2305	-0.5117	-0.8277
Zn-O(1w)	-0.8725	0.3130	0.3751
Zn-O(2)	0.0009	-0.8618	0.5072
Zn- O(12)	-0.2578	0.2959	-0.9198
Li(1)-O(2w)	0.6719	0.2344	0.7026
Li(1)-O(12)	-0.5568	-0.3946	-0.7309
Li(1)-O(1w)	-0.8715	-0.4609	0.1671
Li(1)-O(3)	-0.5056	0.4565	-0.7321
Li(2)-O(13c)	-0.3893	-0.1499	-0.9088
Li(2)-O(3w)	0.7796	0.5394	0.3183

Table 3.3 Comparison of the principal values of spin-Hamiltonian parameters of the VO(II)/ALMZ with other lattices.

Lattice	Spectroscopic splitting factor (g)			Hyperfine constant A (mT)			Ref.
	g_{zz}	g_{xx}	g_{yy}	A_{zz}	A_{xx}	A_{yy}	
PMZD[a]	1.936	1.978	1.972	18.24	7.12	6.73	[22]
DABMZ[b]	1.937	1.980	1.972	18.14	8.36	6.09	[23]
GeO_2	1.929	1.976	1.976	17.55	6.82	6.82	[24]
$K_2TiO(C_2O_4)_2.2H_2O$	1.940	1.972	1.972	16.30	6.00	6.00	[25]
ALMZ	1.933	1.976	1.973	18.01	7.01	6.77	Present Work

[a] Dipotassium diaquabis(malonato-κ^2O,O') zincate dehydrate.

[b]Diaquabis[malonato(1-) κ^2O,O'] zinc(II).

Table 3.4 Orbital admixture coefficients and bonding parameters of vanadyl ion in various systems.

Host lattice	C_1	C_2	C_3	κ	$P\times10^{-4}$ cm^{-1}	Ref.
MPSH[c]	0.700	0.713	0.070	0.85	133.1	[29]
MPPH[d]	0.701	0.712	0.006	0.83	130.7	[30]
MAPH[e]	0.701	0.711	0.040	0.91	112.0	[1]
CPPH[f]	0.701	0.711	0.001	0.77	141.9	[2]
ZSPH[g]	0.701	0.711	0.001	0.84	133.8	[31]
ALMZ	0.701	0.711	0.040	0.81	130	Present Work

[c]Magnesium Potassium Sulphate Hexahydrate.

[d]Magnesium Potassium Phosphate Hexahydrate.

[e]Magnesium Ammonium Phosphate Hexahydrate.

[f]Cadmium Ammonium Phosphate Hexahydrate.

[g]Zinc Sodium Phosphate Hexahydrate.

Table 3.5 Molecular orbital coefficients for VO(II) ion in various lattices.

Systems	β_1^2	β_2^2	γ^2	Ref.
LAM[h]				
Site I	0.26	1	0.62	[10]
Site II	0.68	1	0.95	
PMZD[i]	0.78	-	0.74	[22]
DABMZ[j]	0.76	-	0.58	[23]
MPPH	0.84	-	0.89	[30]
ALMZ	0.86	0.84	0.91	Present work

[h] L-asparagine monohydrate.

[I] dipotassium diaquobis(malonato-κ^2O,O′) zincate dihydrate.

[j] diaquabis[malonato(1-)-κ^2O,O′] zinc(II)

Table 3.6 Observed FT-IR bands and their tentative assignments for pure ALMZ and VO(II)/ALMZ.

Assignments	FT-IR bands (cm^{-1})	
	Pure ALMZ	VO(II) doped ALMZ
Zn – O	401	419
Zn – O + O – C = O	789	787
- OH	3468, 3182	3470
....OH_2	3029	3029
Zn – OH_2	718, 789	665, 723
	885, 945	947
-CH_2-	2921	2923
-C = O	1175, 1285	1180, 1256
	1570, 2152	1728

Table 3.7 Calculated lattice parameters of ALMZ and VO(II)/ALMZ from powder XRD, along with single crystal XRD of ALMC [20].

Lattice parameters (nm) of ALMC from single crystal XRD	Lattice parameters (nm) calculated from powder XRD	
	ALMZ	VO(II) doped ALMZ
a = 0.6851	a = 0.6382	a = 0.6382
b = 0.8852	b = 0.8424	b = 0.8424
c = 1.0529	c = 1.0293	c = 1.0293

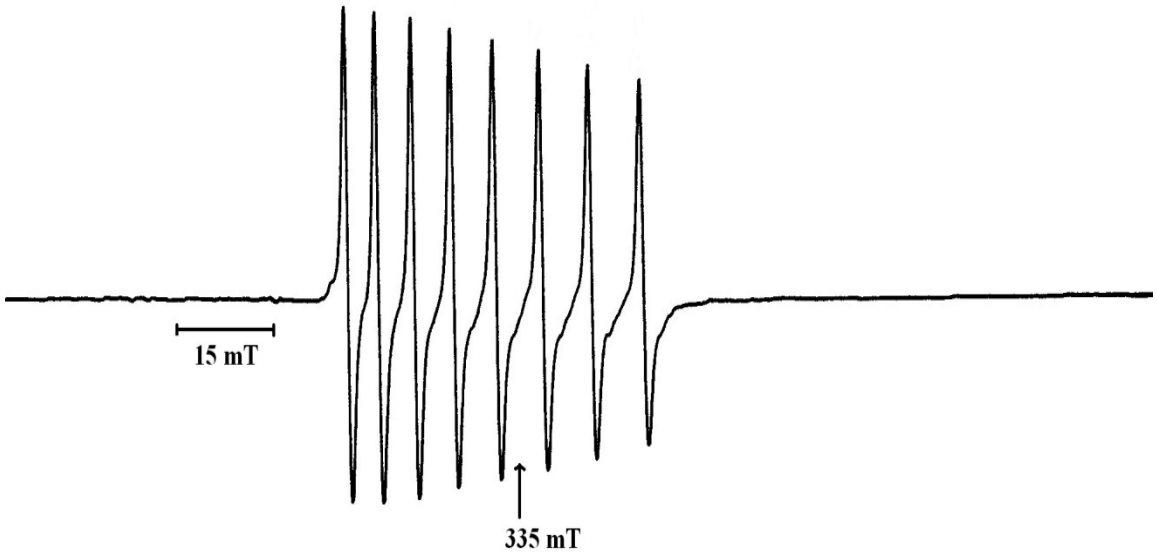

Fig. 4.1 Single crystal EPR spectrum of VO(II)/PBMN when the applied magnetic field (B) is 50º away from the crystallographic axis a in ab plane. Frequency = 9.05989 GHz.

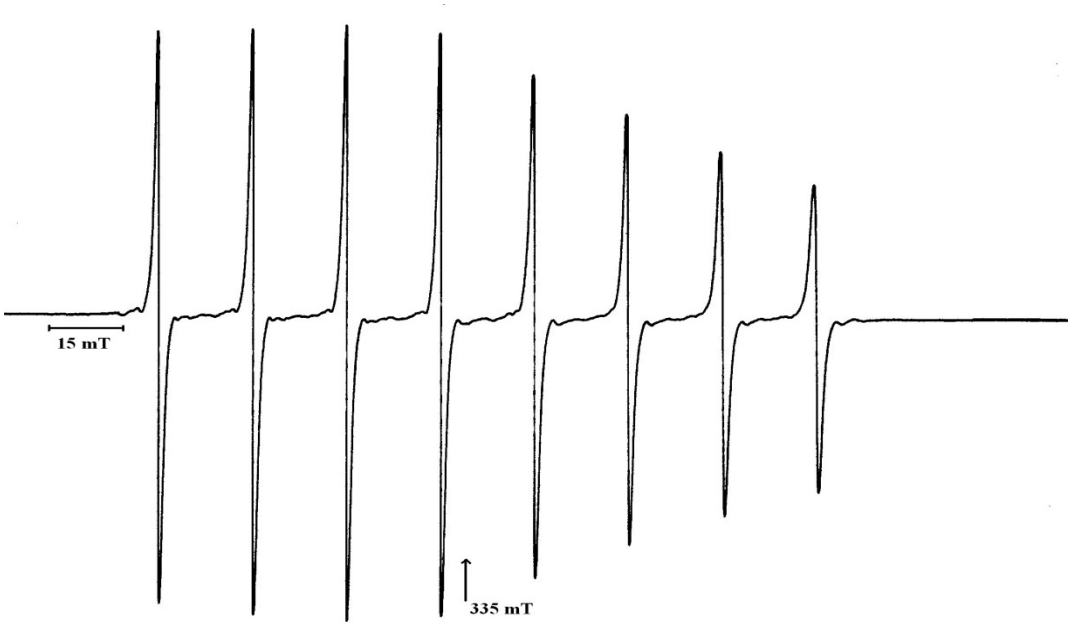

Fig. 4.2 Single crystal EPR spectrum of VO(II)/PBMN recorded at room temperature when B is 140º away from the axis c in ac plane. Frequency = 9.06020 GHz.

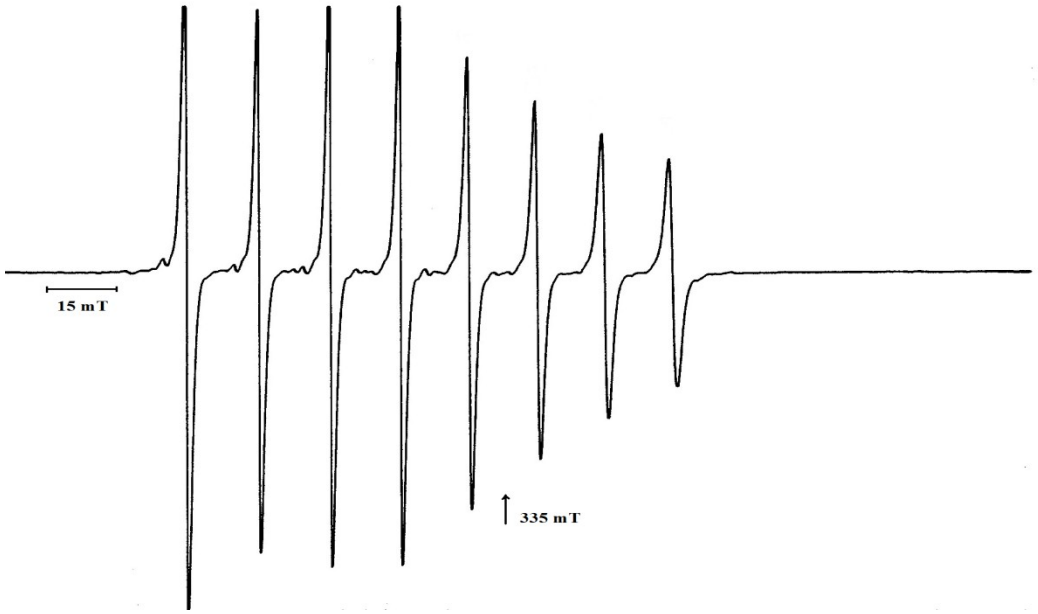

Fig. 4.3 Single crystal EPR spectrum of VO(II)/PBMN recorded at room temperature when B is parallel to crystallographic axis c. Frequency = 9.05926 GHz.

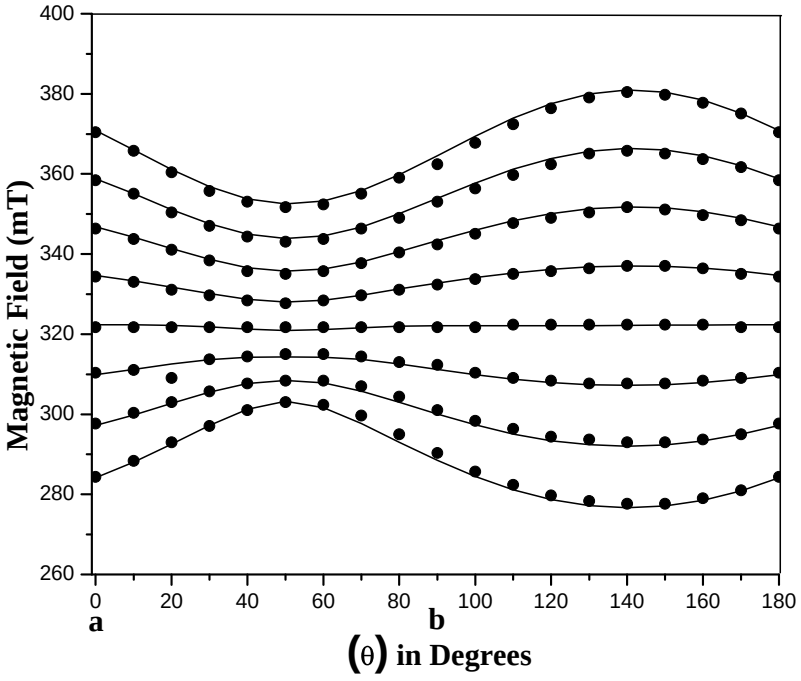

Fig. 4.4 Angular variation of hyperfine lines for axis c rotation of the VO(II)/PBMN single crystal at room temperature. The solid circles and lines correspond to experimental and theoretical values respectively. Frequency = 9.05989 GHz.

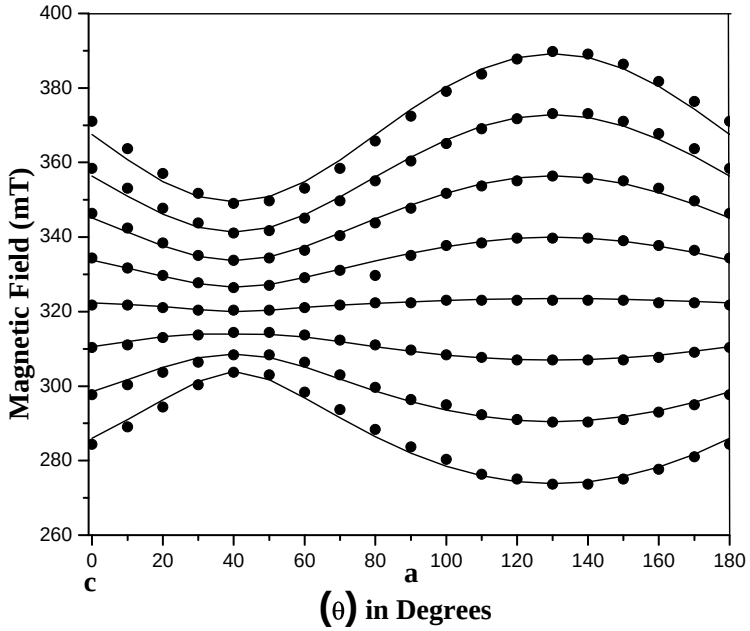

Fig. 4.5 Angular variation of hyperfine lines for axis b rotation of the VO(II)/PBMN single crystal at room temperature. Frequency = 9.06020 GHz.

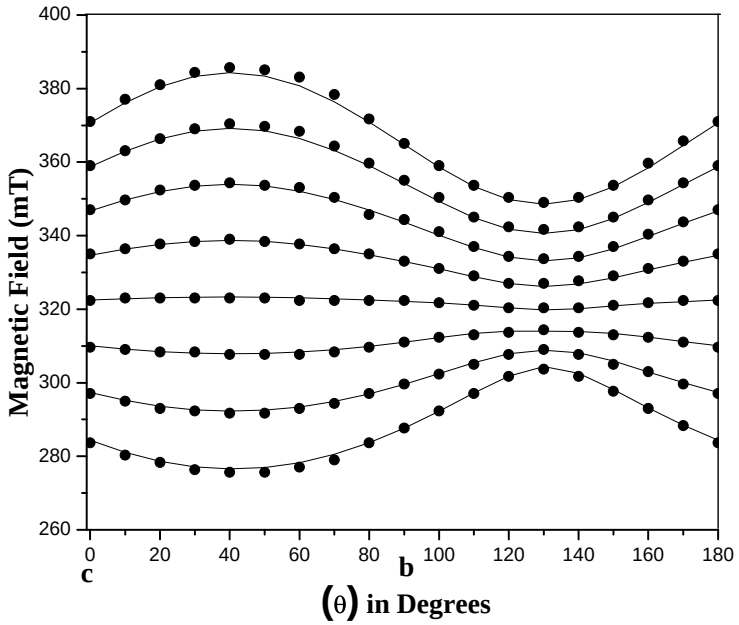

Fig. 4.6 Angular variation of hyperfine lines for axis a rotation of the VO(II)/PBMN single crystal at room temperature. Frequency = 9.05926 GHz.

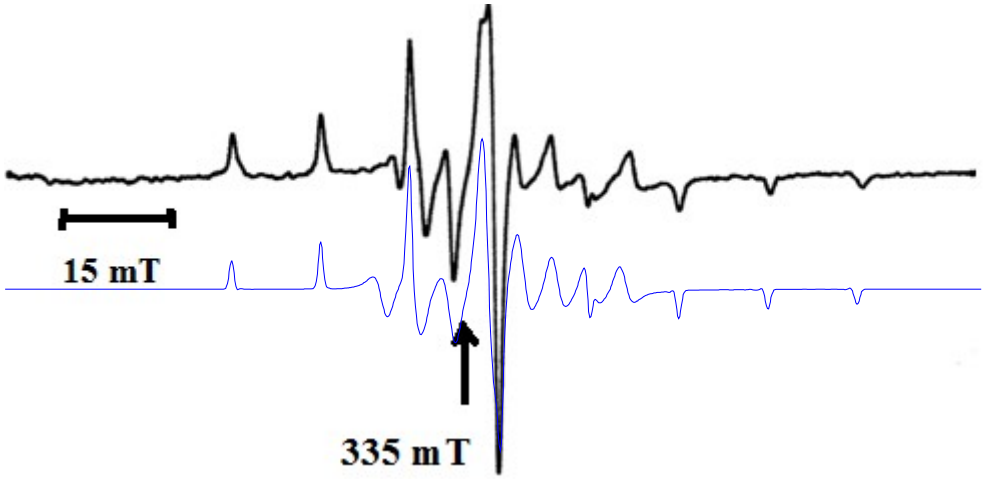

Fig. 4.7 Powder EPR spectrum of VO(II)/PBMN at room temperature. Top figure corresponds to experimental one, whereas bottom one is the simulated using powder values. Frequency = 9.35653 GHz.

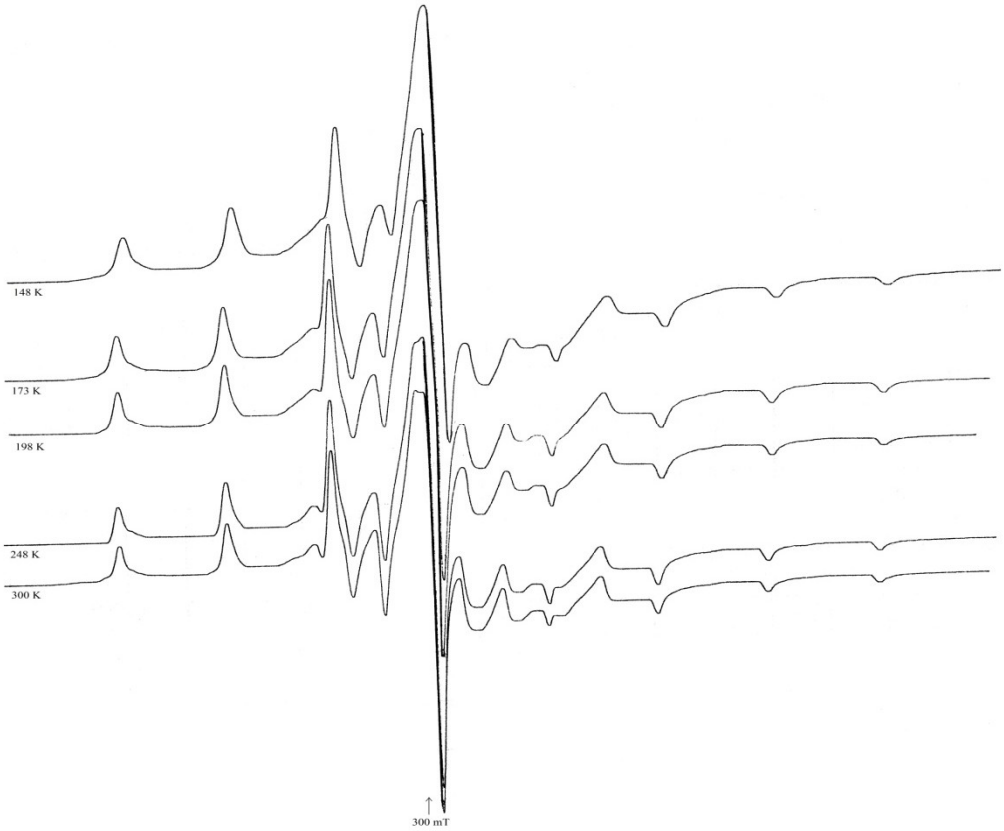

Fig. 4.8 Variable temperature powder EPR spectra of the VO(II)/PBMN. These spectra have been used to calculate relaxation times. Frequency = 9.11963 GHz.

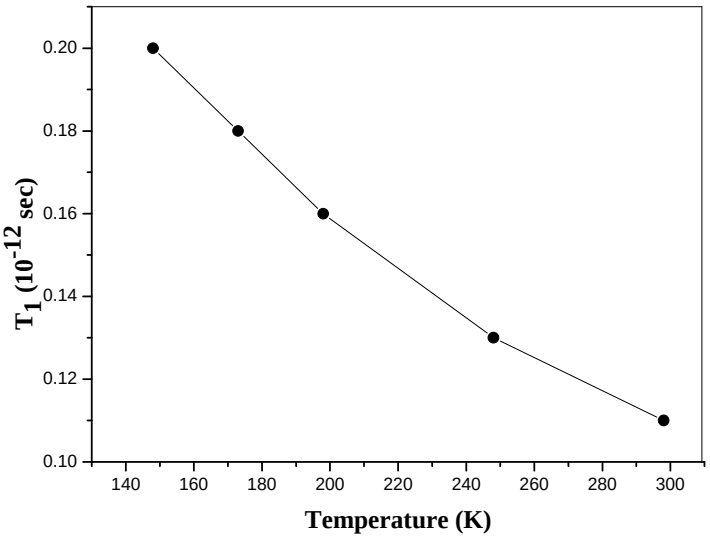

Fig. 4.9 Plot of host spin-lattice relaxation time (T_1), derived using line-width of the VO(II)/PBMN, as a function of temperature.

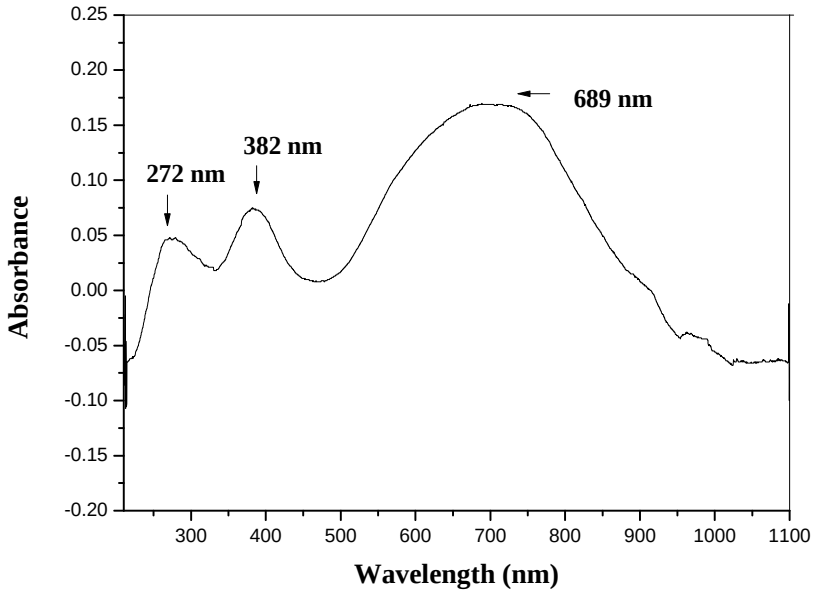

Fig. 4.10 Optical absorption spectrum of VO(II)/PBMN recorded at room temperature.

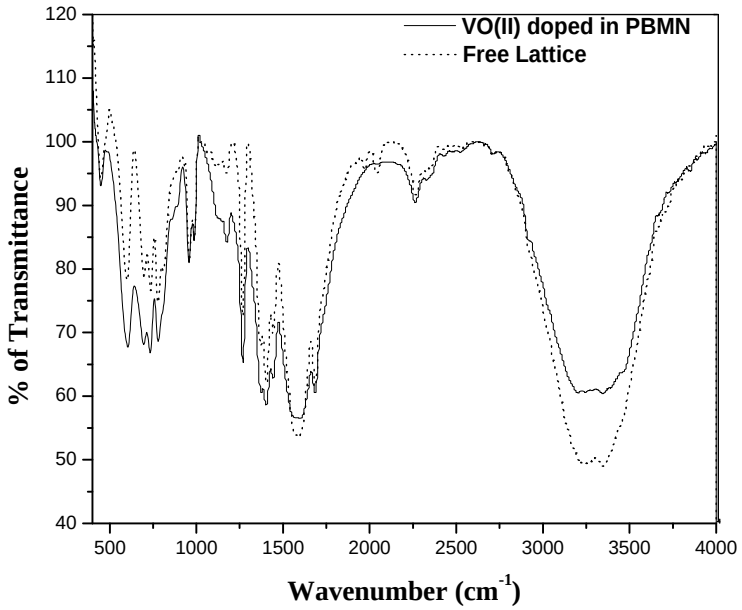

Fig. 4.11 FT-IR spectrum of VO(II)/PBMN recorded at room temperature.

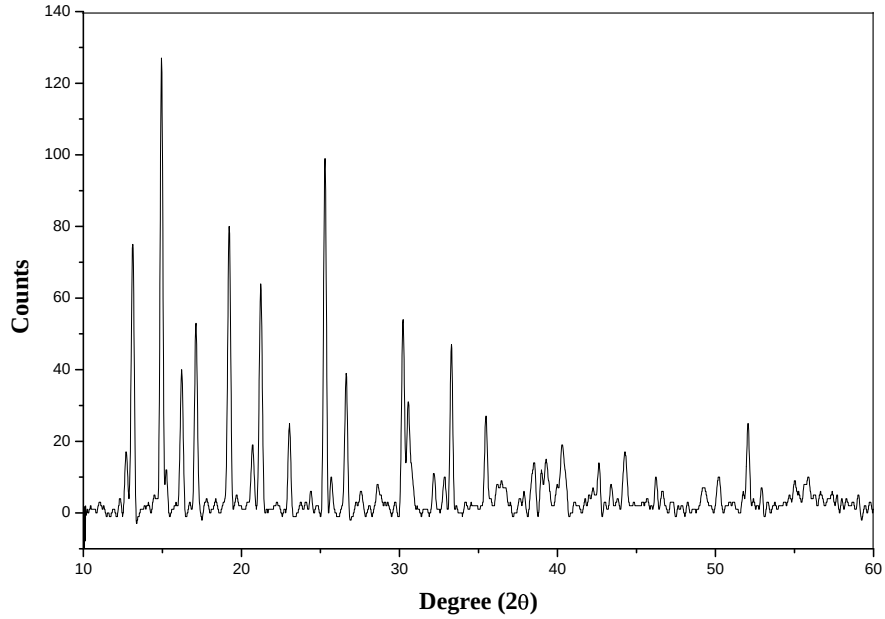

Fig. 4.12 Powder XRD pattern of VO(II)/PBMN recorded at room temperature.

Table 4.1 The Spin Hamiltonian Parameters obtained from the single crystal rotations for VO(II) doped in PBMN using program EPR-NMR [22].

			Principal values	Direction cosines		
				a	b	c
g matrix						
1.959	0.006	0.016	1.979	-0.4249	0.5354	-0.7298
	1.964	-0.014	1.968	-0.7041	-0.7022	-0.1052
		1.959	1.936	-0.5689	0.4692	0.6755
A matrix (mT)						
10.87	-3.18	-4.45	6.92	0.3459	-0.5429	0.7651
	9.43	3.85	6.02	-0.7198	-0.6767	-0.1547
		10.77	18.12	-0.6017	0.4973	0.6249
Powder spectrum						
$g_{\parallel}$ = 1.995	$g_{\perp}$ = 1.973	$A_{\parallel}$ = 18.31 mT	$A_{\perp}$ = 6.99 mT			

Table 4.2 The direction cosines of Ni-O bonds and K-O bonds for PBMN, obtained from the crystallographic data.

Ni-O, K-O bonds in PBMN	Direction cosines		
	a	b	c
Ni-O (1)	0.3684	0.7375	0.6076
Ni-O (2)	0.4611	-0.7192	0.5232
Ni-O (3)	0.3881	0.5304	0.7537
K(1)-O(1)	0.2492	-0.8895	0.4111
K(1)-O(4)	0.2486	-0.8789	0.4072
K(1)-O(1w)	0.0000	1.0000	0.0000
K(1)-O(2w)	-0.1869	-0.9621	-0.1986
K(2)-O(2)	0.4345	1.1675	0.4930
K(2)-O(4)	0.4736	0.4166	0.7759
K(2)-O(2w)	-0.6303	-0.3930	-0.6695

Table 4.3 Spin Hamiltonian parameters of VO(II) in PBMN and other related host lattices

Host lattices	Spectroscopic splitting factor (g)			Hyperfine constant A (mT)			
	g_{xx}	g_{yy}	g_{zz}	A_{xx}	A_{yy}	A_{zz}	Ref.
$H_2Co(C_4H_2O_4)_2 . 6H_2O$							
(site I)	1.975	2.061	1.935	7.1	7.9	18.8	[5]
(site II)	1.985	2.005	1.932	6.7	7.7	18.8	
HCS[a]							
(site I)	1.995	1.985	1.941	7.5	7.7	18.9	[23]
(site II)	1.986	1.979	1.941	7.3	7.7	18.6	
Cosacpy[b]							
(site I)	2.001	1.989	1.938	7.3	5.2	18.7	[24]
(site II)	2.001	1.987	1.923	7.17	7.35	19.91	
PBMN	1.979	1.968	1.936	6.92	6.02	18.12	Present work

[a] Hexaimidazol cobalt sulphate

[b] Tetraaquabis (pyridine) Co(II) saccharinate tetrahydrate

Table 4.4 Orbital admixture coefficients and bonding parameters for a few vanadyl ions.

Host lattice	C_1	C_2	C_3	κ	$P\times10^{-4}$ cm^{-1}	Ref.
$MgK_2SO_4.6H_2O$	0.700	0.713	0.040	0.85	133.1	[20]
HCS	0.702	0.711	0.040	0.87	130.0	[23]
MAPH[c]	0.702	0.711	0.040	0.91	112.0	[26]
CAPH[d]	0.702	0.711	0.040	0.88	125.7	[27]
PBMN	0.702	0.712	0.040	0.84	110.0	Present work

[c] Magnesium ammonium phosphate hexahydrate

[d] Cadmium ammonium phosphate hexahydrate

Table 4.5 Molecular orbital coefficients of VO(II) doped in PBMN.

Host lattice	β_1^2	β_2^2	e_π^2	Ref.
$KZnClSO_4.3H_2O$	0.91	1	0.68	[15]
POM	0.86	1	0.86	[19]
LAM				
Site I	0.26	1	0.62	[32]
Site II	0.68	1	0.95	
Sodium citrate				
Site I	0.91	1	0.68	
Site II	0.88	1	0.71	[33]
PBMN	0.94	0.93	0.89	Present work

Table 4.6 Observed FTIR bands and their tentative assignments for pure PBMN and VO(II) doped PBMN. (br-broad, sh-sharp, w-weak)

Band Positions (cm^{-1})		Assignments
Pure PBMN	VO(II) doped PBMN	
3350 (br)	3350 (br)	O –H stretching
3250 (br)	3250 (br)	
2270 (w)	2270 (w)	C – H stretching
2040 (w)	2040 (w)	
1970 (w)	1970 (w)	
1690 (sh)	1690 (sh)	C =O stretching
1590 (sh)	1590 (sh)	C - C stretching
1440 (sh)	1440 (sh)	O – H bending
1400 (sh)	1400 (sh)	
1370 (sh)	1370 (sh)	C – H bending
1180 (sh)	1180 (sh)	O – H out of plane deformation
1110 (sh)	1110 (sh)	
987 (sh)	987 (sh)	
779 (sh)	779 (sh)	C –H out of plane bend
737 (sh)	737 (sh)	
698 (sh)	698 (sh)	
600 (sh)	600 (sh)	O – H deformation
449 (sh)	449 (sh)	

Table 4.7 The calculated lattice parameters of PBMN and VO(II) doped PBMN from powder XRD, along with single crystal XRD of PBMC [21].

Lattice parameters (nm) of PBMC from single crystal XRD	Lattice parameters (nm) calculated from powder XRD	
	PBMN	VO(II) doped PBMN
a = 0.7398	a = 0.7482	a = 0.7482
b = 1.8830	b = 1.8924	b = 1.8924
c = 0.9320	c = 0.9823	c = 0.9823

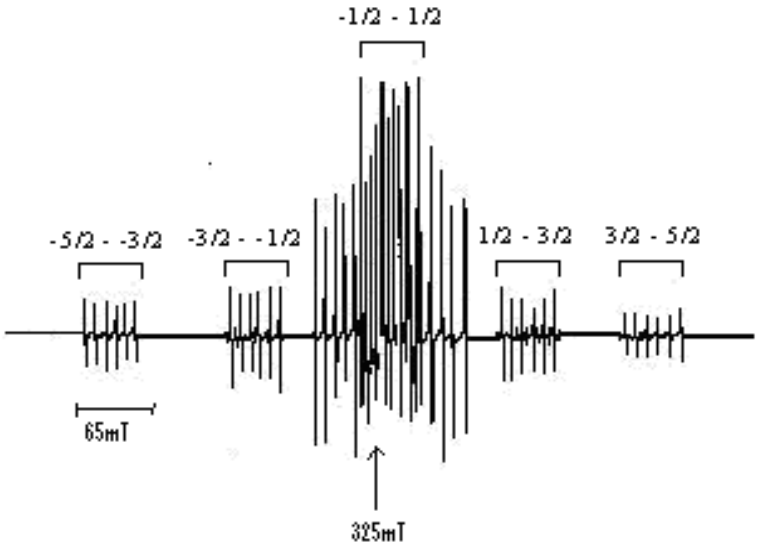

Fig. 5.1 Single crystal EPR spectrum of Mn(II)/PBMZ recorded at room temperature, when the applied magnetic field (B) is parallel to axis c. Frequency = 9.41409 GHz. Labeling of five transitions is indicated.

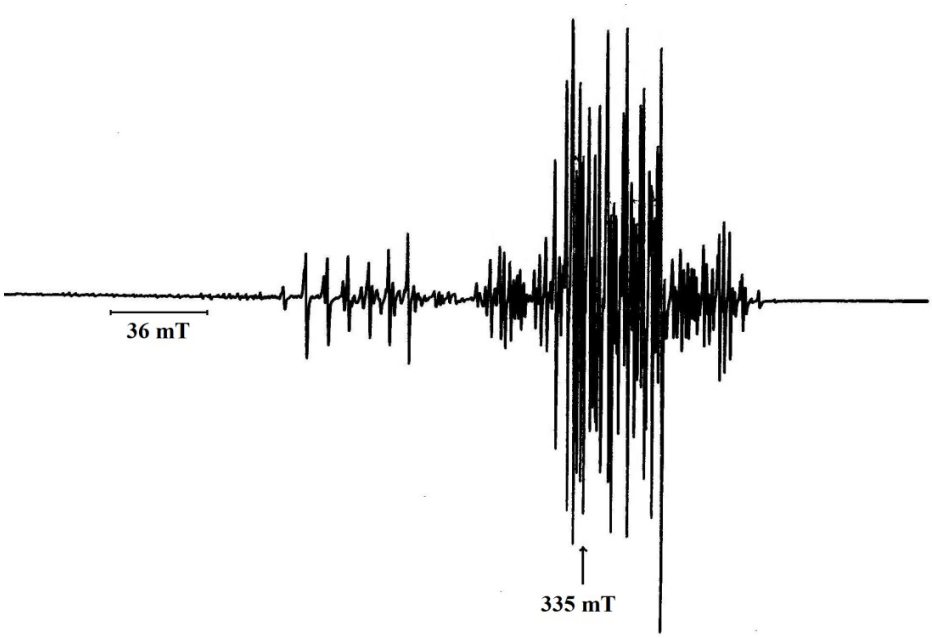

Fig. 5.2 Single crystal EPR spectrum of Mn(II)/PBMZ recorded at room temperature, when the B is 60º away from axis c, while rotating the crystal in ac plane. Frequency = 9.41821 GHz.

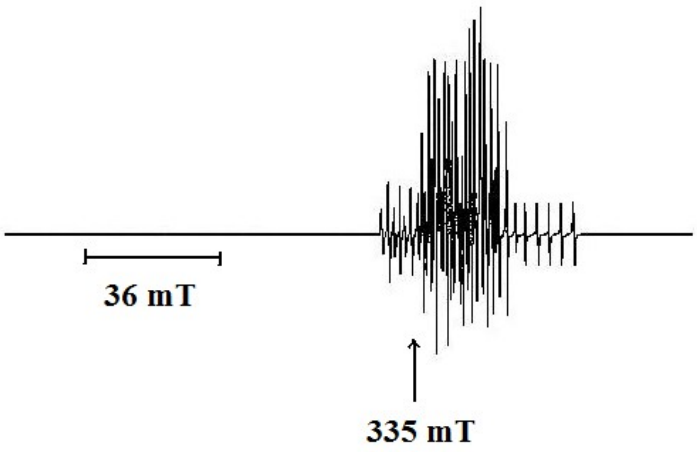

Fig. 5.3 Single crystal EPR spectrum of Mn(II)/PBMZ recorded at room temperature, when the B is parallel to axis b. Frequency = 9.41990 GHz.

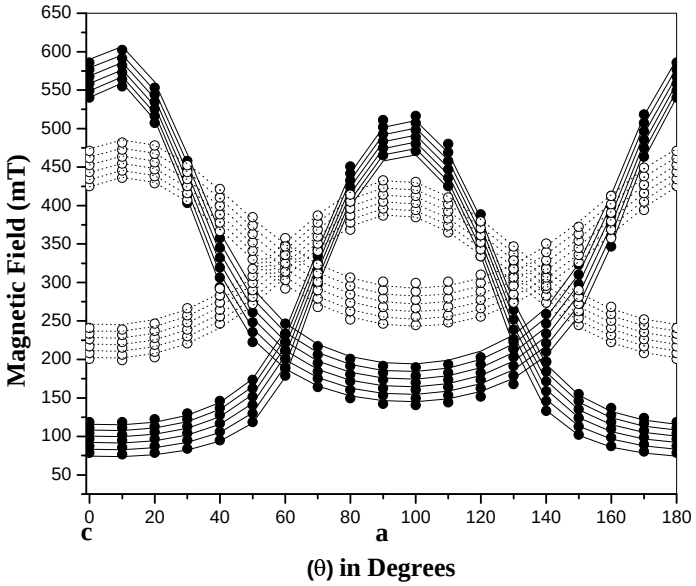

Fig. 5.4 Isofrequency plot of Mn(II)/PBMZ in ac plane. |±5/2> ↔ |±3/2> transitions are only shown in Figs. 5.4, 5.5 and 5.6 because |±3/2> ↔ |±1/2> and |+1/2> ↔ |-1/2> transitions could not be resolve due to overlap. Solid and open circles indicate experimental values, whereas solid and dotted lines correspond to theoretical values of Site 1 and Site 2 respectively. Frequency = 9.41821 GHz.

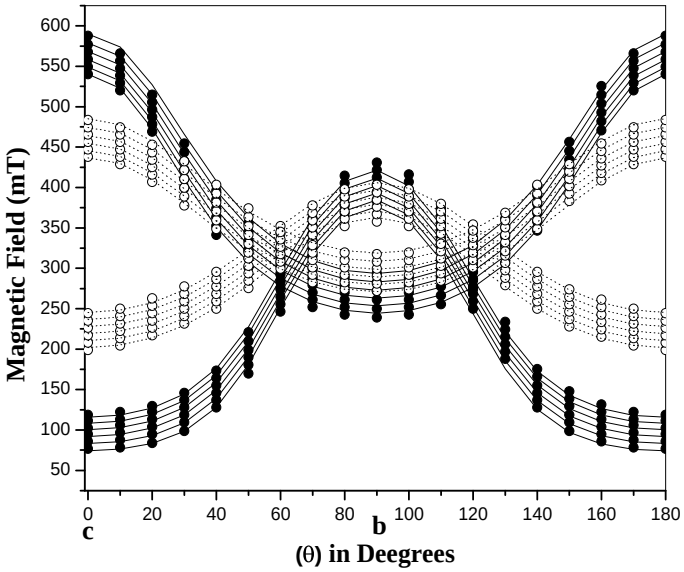

Fig. 5.5 Isofrequency plot of Mn(II) resonance in the bc plane of crystal lattice PBMZ. Frequency = 9.41409 GHz.

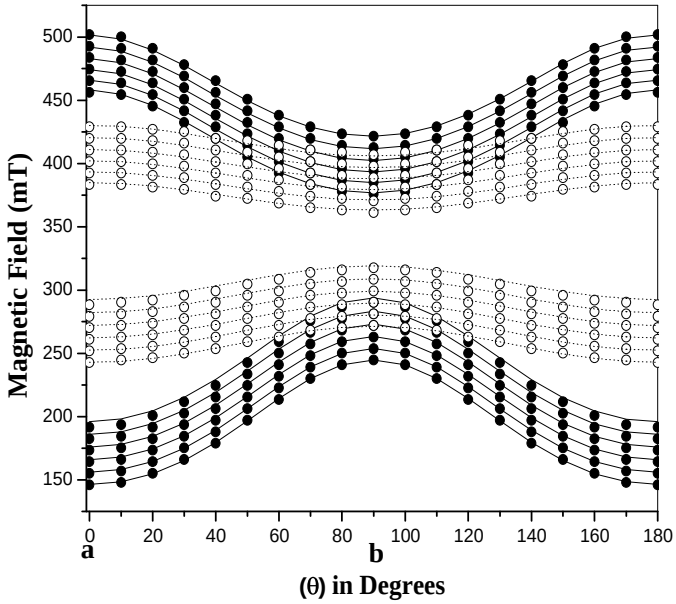

Fig. 5.6 Isofrequency plot of Mn(II) resonances in the ab plane of crystal lattice PBMZ. Frequency = 9.41990 GHz.

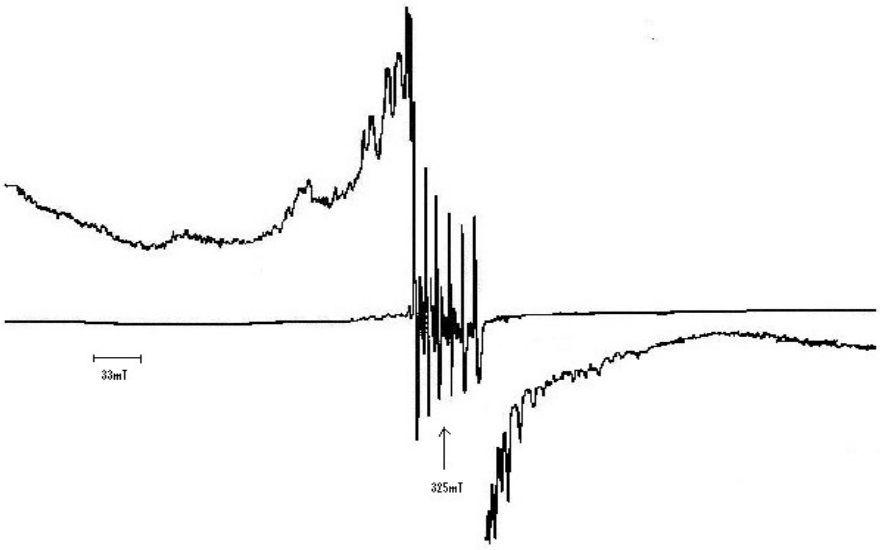

Fig. 5.7 Polycrystalline EPR spectrum of Mn(II)/PBMZ recorded at room temperature. The lower and higher field resonances have been recorded at higher gains to exactly locate the positions. Frequency = 9.38600 GHz.

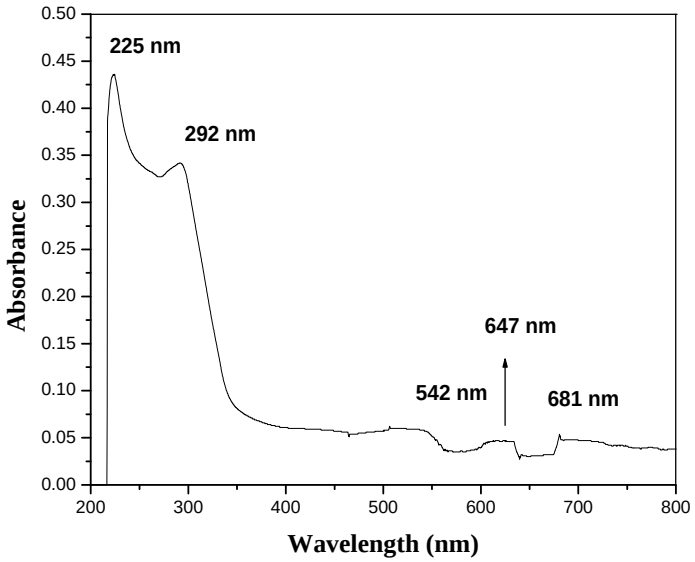

Fig. 5.8 Optical absorption spectrum of Mn(II) doped PBMZ at room temperature.

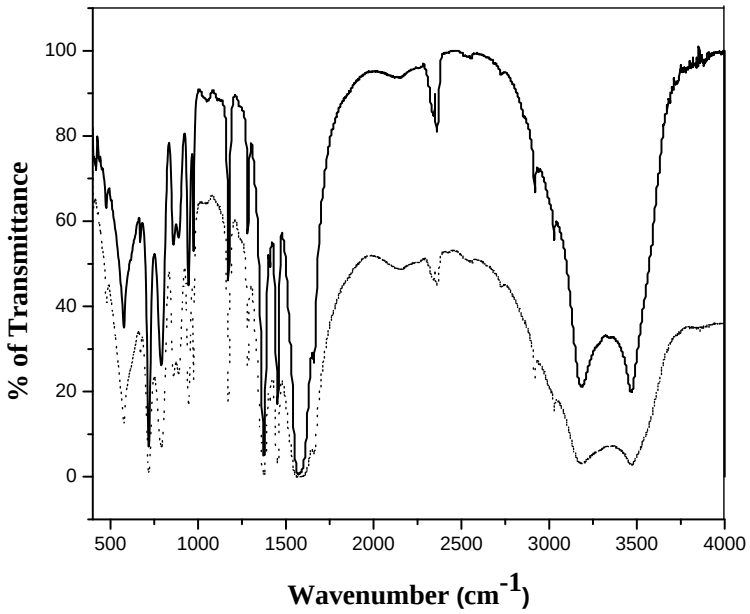

Fig. 5.9 Powder FT-IR spectra of PBMZ (dotted line) and Mn(II) doped PBMZ (solid line) at room temperature.

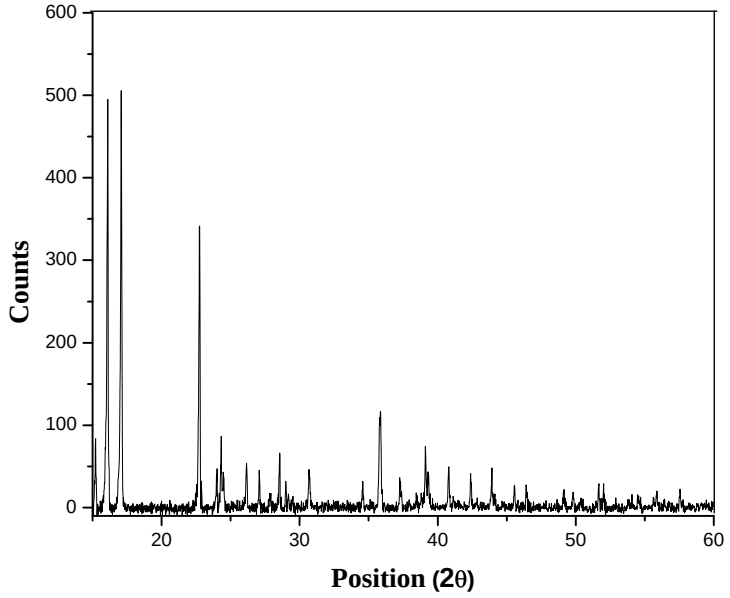

Fig. 5.10 Powder XRD pattern of Mn(II) doped PBMZ.

Table 5.1 The spin Hamiltonian parameters obtained from the single crystal rotations for Mn(II) doped in PBMZ using program EPR-NMR [19].

			Principal values	Direction cosines		
				a	b	c
Site-1						
g matrix						
2.092	0.000	-0.025	2.099	-0.8293	0.4907	0.2672
	2.092	0.014	2.092	-0.5069	-0.8619	0.0097
		1.996	1.988	0.2352	-0.1273	0.9637
A matrix (mT)						
9.62	0.00	-0.26	9.77	-0.3717	-0.9034	0.2136
	9.76	-0.06	9.71	-0.8527	0.4232	0.3063
		9.07	8.96	-0.3672	-0.0682	-0.9276
D matrix (mT)						
28.00	0.00	-8.69	-29.09	0.9922	0.0011	-0.1249
	11.90	-0.15	-11.90	0.0015	-0.9999	0.0027
		-39.90	40.99	-0.1249	-0.0028	-0.9921
Site-2						
g matrix						
2.001	0.000	-0.055	2.040	-0.8140	0.0308	0.5800
	1.995	0.003	1.995	0.0425	0.9990	0.0065
		1.963	1.924	-0.5792	0.0299	0.8145
A matrix (mT)						
9.39	0.02	-0.22	9.51	-0.8788	0.1079	0.4648
	8.96	0.16	9.09	-0.3912	-0.7209	-0.5720
		9.05	8.80	0.2734	-0.6845	0.6758
D matrix (mT)						
11.87	-0.00	1.42	-11.94	-0.9989	0.0008	-0.0453
	7.51	-0.01	-7.51	0.0009	0.9999	-0.0004
		-19.38	19.45	0.0454	-0.0004	-0.9989

Table 5.2 The direction cosines of Zn-O bonds and K-O bonds for PBMZ, obtained from the crystallographic data.

Zn-O, K-O bonds in	Direction cosines		
PBMZ	a	b	c
Zn-O (1)	0.3684	0.7375	0.6076
Zn-O (2)	0.4611	-0.7192	0.5232
Zn-O (3)	0.3881	0.5304	0.7537
K(1)-O(1)	0.2492	-0.8895	0.4111
K(1)-O(4)	0.2486	-0.8789	0.4072
K(1)-O(1w)	0.0000	1.0000	0.0000
K(1)-O(2w)	-0.1869	-0.9621	-0.1986
K(2)-O(2)	0.4345	1.1675	0.4930
K(2)-O(4)	0.4736	0.4166	0.7759
K(2)-O(2w)	-0.6303	-0.3930	-0.6695

Table 5.3 Spin Hamiltonian parameters for Mn(II) in some related host lattices (D, E and A are in mT)

System	g	A	D	E	Ref.
MHMH[a]	1.997	8.8			
	2.013	8.8	31.20	3.47	[26]
	2.013	8.8			
ZAPH[b]	1.966	9.1	-12.28		
	1.972	9.1	-2.09	6.1	[27]
	1.976	11.1	14.37		
CAPH[c]					
Site 1	1.946	8.3	-15.9		
	1.986	8.5	5.6	2.3	[28]
	2.007	9.7	10.3		
Site 2	1.888	8.5	-12.6		
	1.944	8.6	-7.5	-2.6	
	2.014	9.6	20.1		
PBMZ					
Site 1	2.099	9.77	-29.09		
	2.092	9.71	-11.90	8.6	
	1.988	8.96	40.99		
					Present
Site 2	2.040	9.51	-11.94		work
	1.995	9.09	-7.51	2.2	
	1.923	8.80	19.45		
Powder data	2.021	9.10	52.84		
			22.73		

[a] magnesium bis(hydrogen maleate) hexahydrate

[b] zinc ammonium phosphate hexahydrate

[c] cadmium ammonium phosphate hexahydrate

Table 5.4 The observed band positions for Mn(II) doped PBMZ.

Observed Band positions		Transitions
Wave length (nm)	Wave number (cm^{-1})	
225	44 533	$^6A_{1g}(S) \rightarrow {}^4T_{2g}(D)$
292	34 217	$^6A_{1g}(S) \rightarrow {}^4E_g(D)$
542	18 456	$^6A_{1g}(S) \rightarrow {}^4A_{1g}, {}^4E_g(G)$
647	15 460	$^6A_{1g}(S) \rightarrow {}^4T_{2g}(G)$
681	14 689	$^6A_{1g}(S) \rightarrow {}^4T_{1g}(G)$

Table 5.5 Observed FTIR bands and their tentative assignment for PBMZ and Mn(II) doped PBMZ.

	FTIR bands PBMZ (cm^{-1})	
Assignments	PBMZ	Mn(II) doped PBMZ
Zn – O	719	720
Zn – O + O – C – O	791	793
Zn – O – H	860, 945	862, 945
- C – H	1170, 1280	1170, 1280
	1370	1371
(C = O) + (C – H)	1450	1450
H – O – H	1570, 2340	1570, 2340
- CH_2 -	2920	2921
--OH_2	3030, 3190	3030, 3190
- OH	3470	3472

Table 5.6 The calculated lattice parameters of PBMZ and Mn(II) doped PBMZ from powder XRD, along with single crystal XRD of PBMC [18].

Lattice parameters (nm) of PBMC from single crystal	Lattice parameters (nm) calculated from powder XRD	
XRD	PBMZ	Mn(II) doped PBMZ
a = 0.73985	a = 0.80706	a = 0.80706
b = 1.8830	b = 1.86824	b = 1.86824
c = 0.9320	c = 0.62529	c = 0.62529

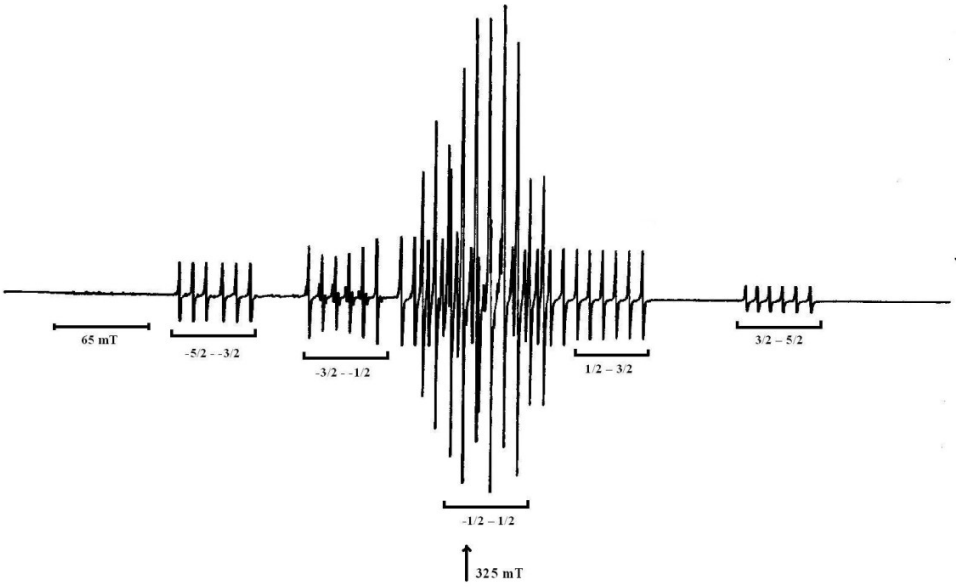

Fig. 6.1 Single crystal EPR spectrum of Mn(II) doped HZBMZ at room temperature when the magnetic field (B) is parallel to axis *c**. Frequency = 9. 34716 GHz. Labeling of five transitions is indicated.

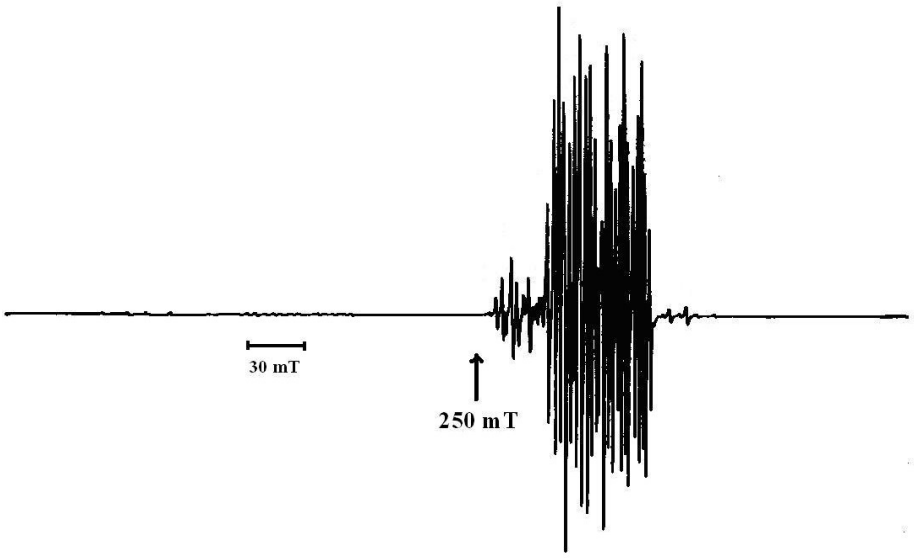

Fig. 6.2 Single crystal EPR spectrum of Mn(II) doped HZBMZ at room temperature when B is to parallel axis *a**. Frequency = 9. 32995 GHz.

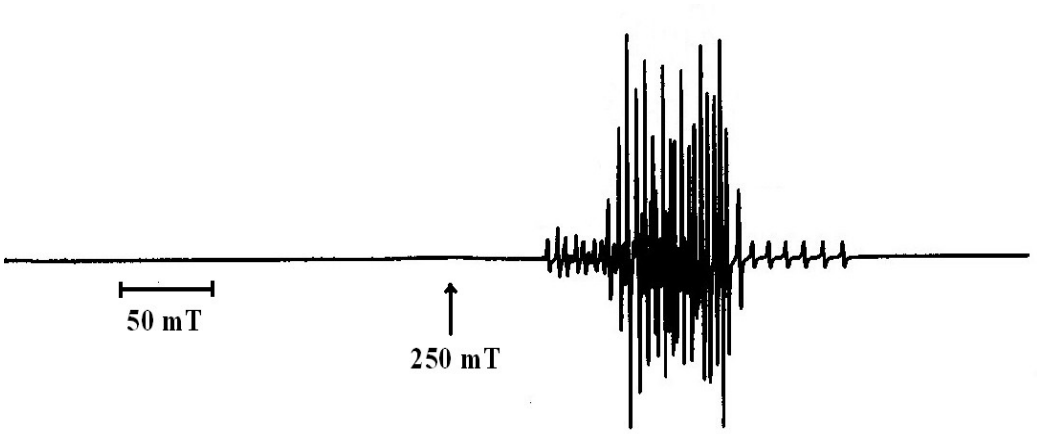

Fig. 6.3 Single crystal EPR spectrum of Mn(II) doped HZBMZ at room temperature when B is parallel to axis *c**. Frequency = 9. 34079 GHz.

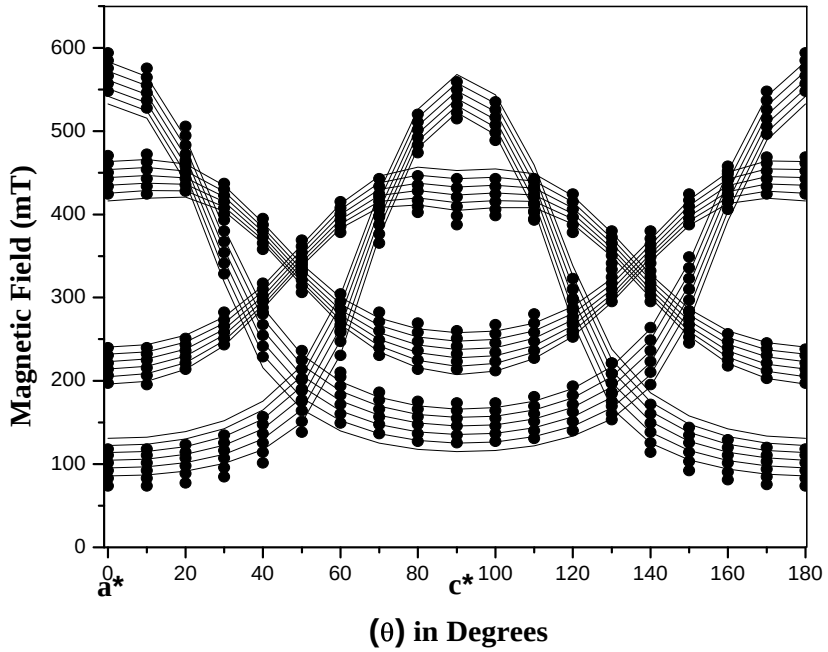

Fig. 6.4 Isofrequency plot of Mn(II) doped HZBMZ for *a***c** plane. Here only |±5/2>↔|±3/2> and |±3/2>↔|±1/2> transitions are shown because |+1/2>↔|-1/2> transition is difficult to follow. Solid circles indicate experimental values; solid lines correspond to theoretical values. Frequency = 9.34716 GHz.

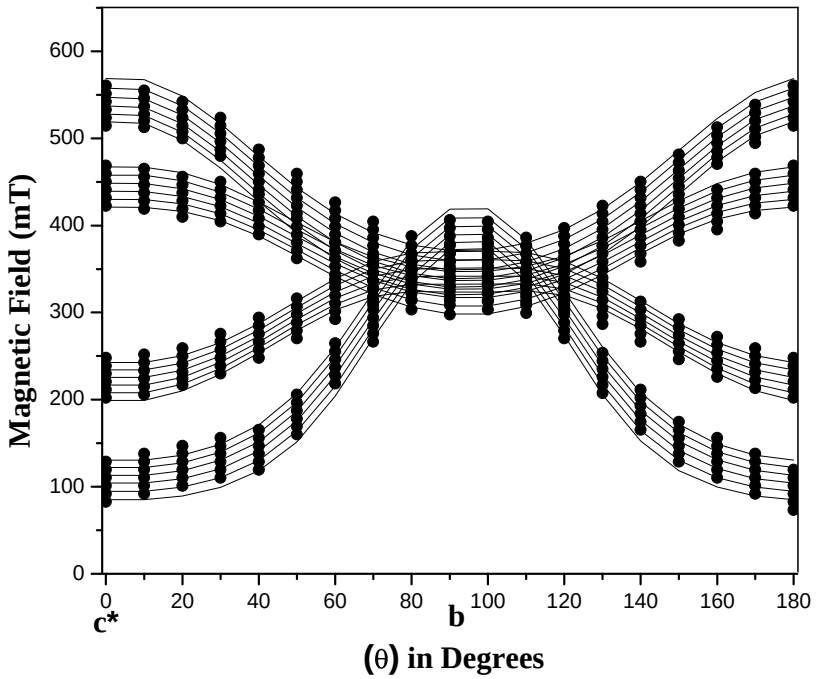

Fig. 6.5 Isofrequancy plot of Mn(II) resonances in the *bc** plane of crystal lattice HZBMZ. Solid circles indicate experimental values, whereas solid lines correspond to theoretical values. Frequency = 9.34079 GHz.

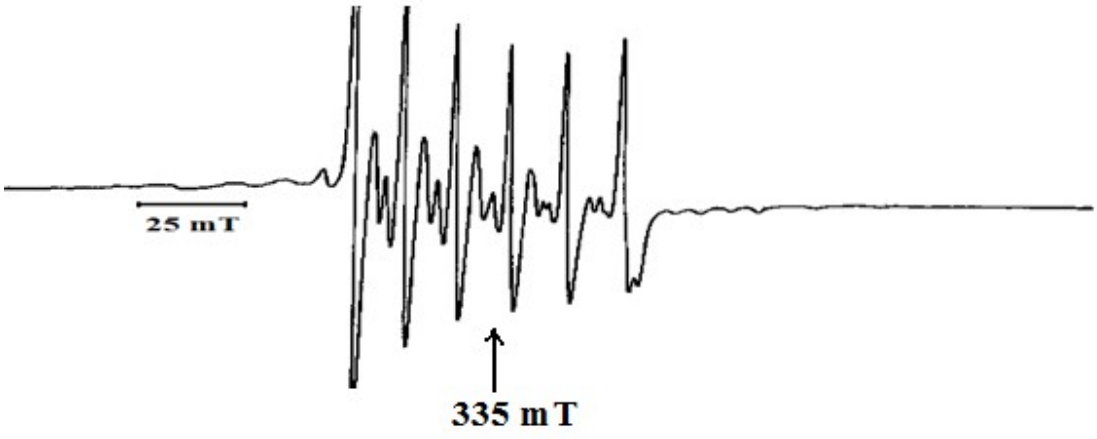

Fig. 6.6 Powder EPR spectrum of Mn(II) doped HZBMZ at room temperature. Frequency = 9.35505 GHz.

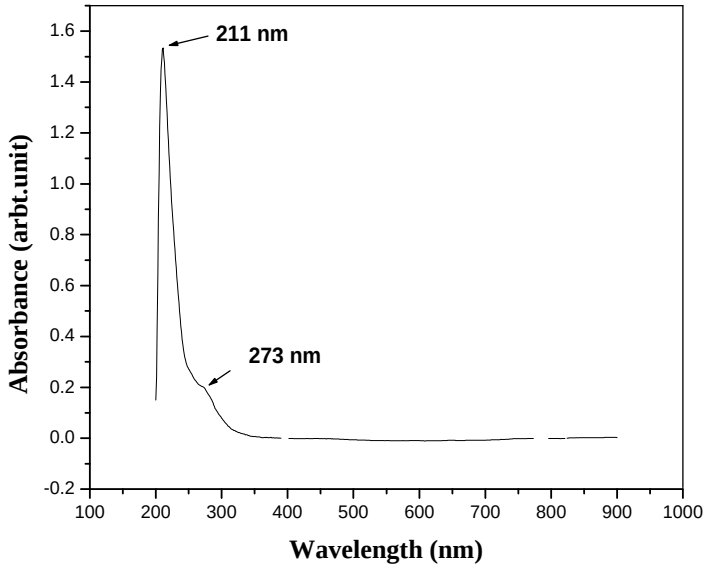

Fig. 6.7 Optical absorption spectrum of Mn(II) ion doped in HZBMZ at room temperature.

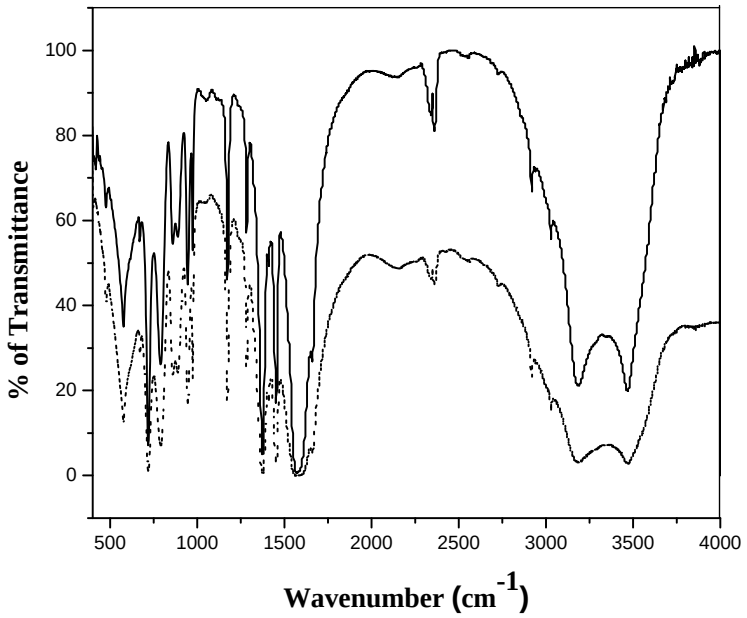

Fig. 6.8 FT – IR spectra of pure (dotted line) and Mn(II) ion doped HZBMZ (solid line) at room temperature.

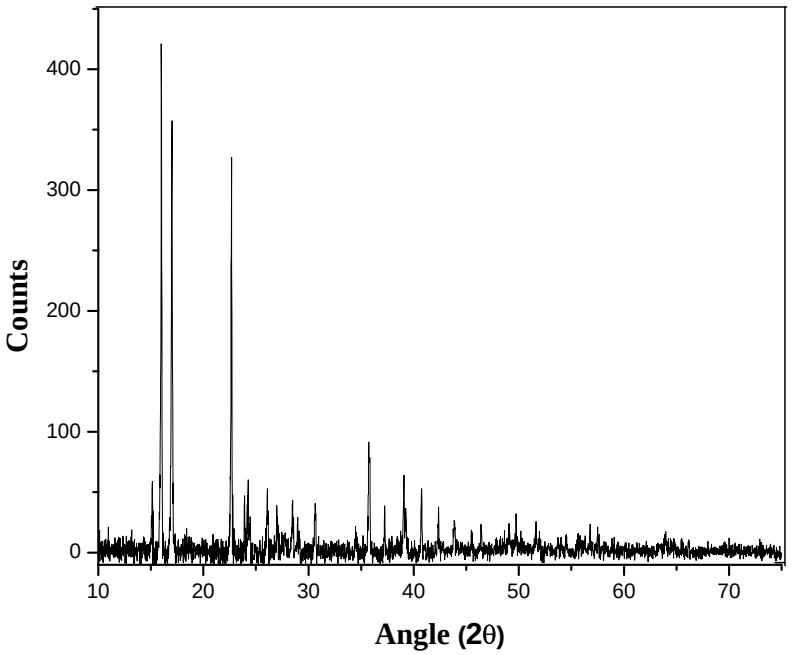

Fig. 6.9 Powder XRD pattern of Mn(II) doped HZBMZ at room temperature.

Table 6.5 The calculated lattice parameters of HZBMZ and Mn(II) doped HZBMZ from powder XRD, along with single crystal XRD of HZBMC [27].

Lattice parameters (nm) of HZBMC From single crystal XRD	Lattice parameters (nm) calculated from powder XRD	
	HZBMZ	Mn doped HZBMZ
a = 0.5274	a = 0.5382	a = 0.5382
b = 0.7504	b = 0.7424	b = 0.7424
c = 1.0314	c = 1.1293	c = 1.1293

Table 6.1 The spin Hamiltonian parameters obtained from the single crystal rotations for Mn(II) doped in HZBMZ using the program EPR-NMR [29].

			Principal Values	Direction cosines		
				a*	b	c*
g matrix						
2.012	0.007	0.008	1.972	0.6028	0.1049	0.7909
	1.973	0.006	2.000	-0.7972	0.1197	0.5917
		2.016	2.023	-0.0326	-0.9872	0.1558
A matrix (mT)						
9.50	0.62	0.10	8.95	0.2366	0.0239	0.9713
	8.95	0.02	9.48	-0.9716	0.0109	0.2363
		9.90	9.93	-0.0049	-0.9996	0.0258
D matrix (mT)						
37.68	-2.72	-2.16	-34.49	0.9995	0.0028	-0.0302
	-3.73	-3.79	-3.25	0.0065	-0.9925	0.1224
		-33.95	37.74	-0.0297	-0.1225	-0.9920

Table 6.2 The direction cosines of Zn-O bonds for HZBMC, obtained from the crystallographic data [27].

Zn – O bonds in HZBMC	Direction cosines		
	a*	b	c*
Zn – O (1w)	0.7389	-0.1537	-0.6559
Zn – O (2w)	-0.3862	0.6280	-0.6756
Zn – O (3w)	0.5328	0.7394	0.4117
Zn – O (1)	0.6448	-0.7395	-0.1934
Zn – O (3)	-0.4591	-0.1025	-0.8825
Zn – O (4w)	0.0000	0.8275	-0.5614

Table 6.3 Spin Hamiltonian parameters for Mn(II) in some related host lattices (D and A are in units of mT).

System	g	A	D	Ref.
MHMH[a]	1.997	8.8	31.20	[31]
	2.013	8.8		
	2.013	8.8		
MMHH[b]	1.995	9.6	33.44	[5]
	2.013	10.6	32.17	
ZAPH[c]	2.002	9.2	53.52	[32]
	2.001	9.2	-35.41	
	2.001	9.3	-18.11	
HZBMZ	1.972	8.95	-34.49	Present
	2.000	9.48	-3.25	Work
	2.023	9.93	37.74	
Powder Values:				
	1.994	9.07	46.23	

[a] magnesium bis(hydrogen maleate) hexahydrate.

[b] magnesium maleate hexahydrate.

[c] zinc ammonium phosphate hexahydrate.

Table 6.4 Observed FTIR band positions and their tentative assignments for HZBMZ and Mn(II) ion doped HZBMZ.

Band positions (cm^{-1})		Assignments
HZBMZ	Mn doped HZBMZ	
719	719	Zn – O
791	793	Zn – O + O – C – O
860,945	862,945	Zn – O – H
1170, 1280	1170, 1280	- C – H
1370, 1386	1370, 1386	
1428, 1408	1428, 1408	- O – H (bending)
1654	1654	(C = O) + (C – H)
1570, 2340	1570, 2340	H – O – H
2920	2920	- CH_2 –
3030, 3190	3030, 3190	--OH_2
3470	3470	- OH

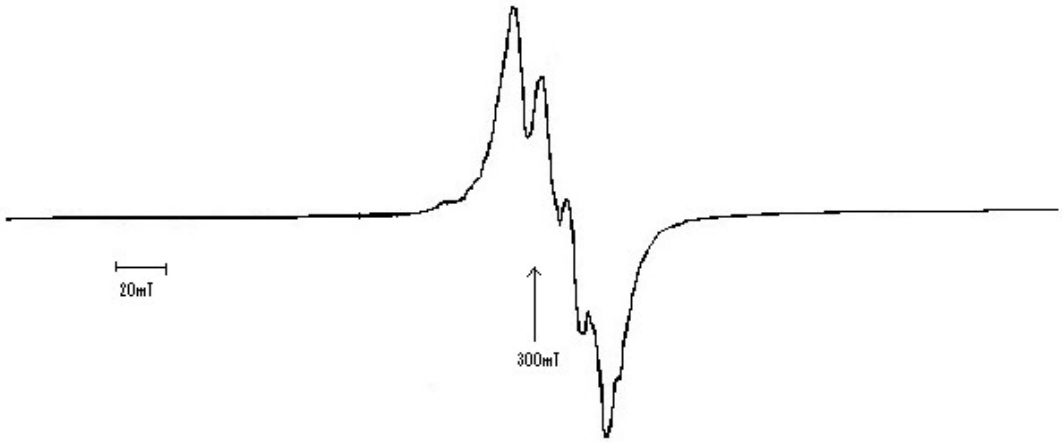

Fig. 7.1 Single crystal EPR spectrum of Cu(II) doped AMMZ recorded at 300 K when the applied magnetic field (B) is parallel to crystallographic axis *a*. Frequency = 9.08527 GHz

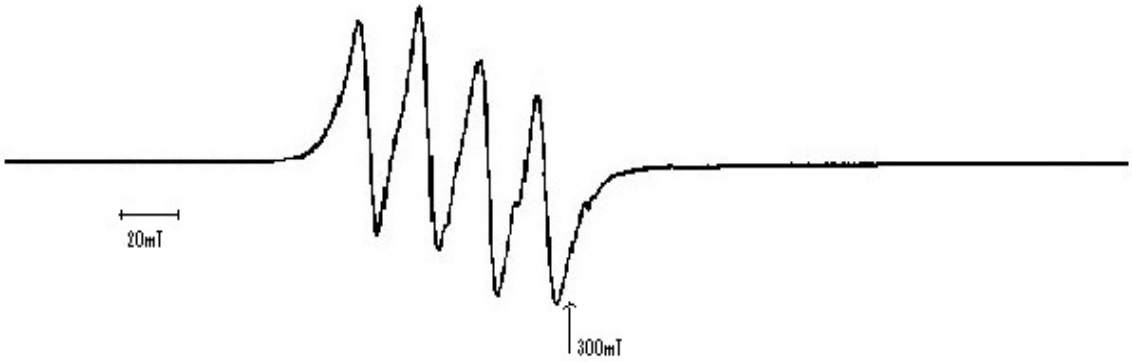

Fig. 7.2 Single crystal EPR spectrum of Cu(II) doped AMMZ recorded at 300 K when B is parallel to crystallographic axis *c*. Frequency (ν) = 9.08425 GHz.

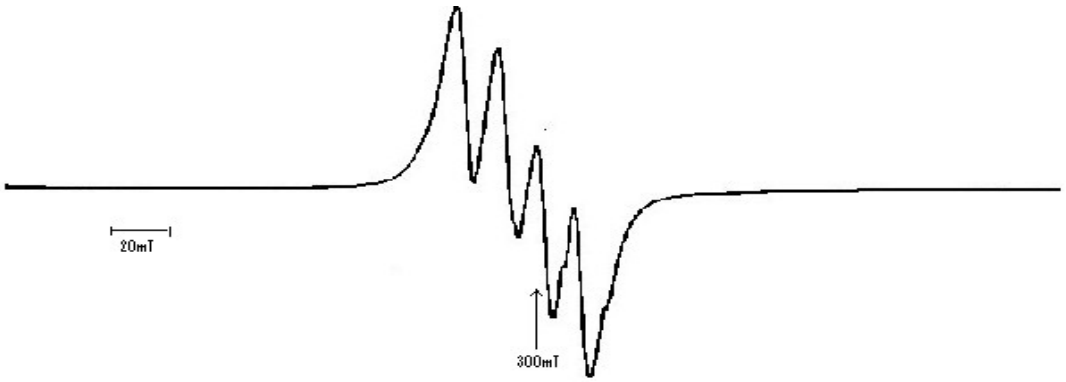

Fig. 7.3 Single crystal EPR spectrum of Cu(II) doped AMMZ recorded at 300 K with B parallel to axis *b*. Frequency =9.08200 GHz.

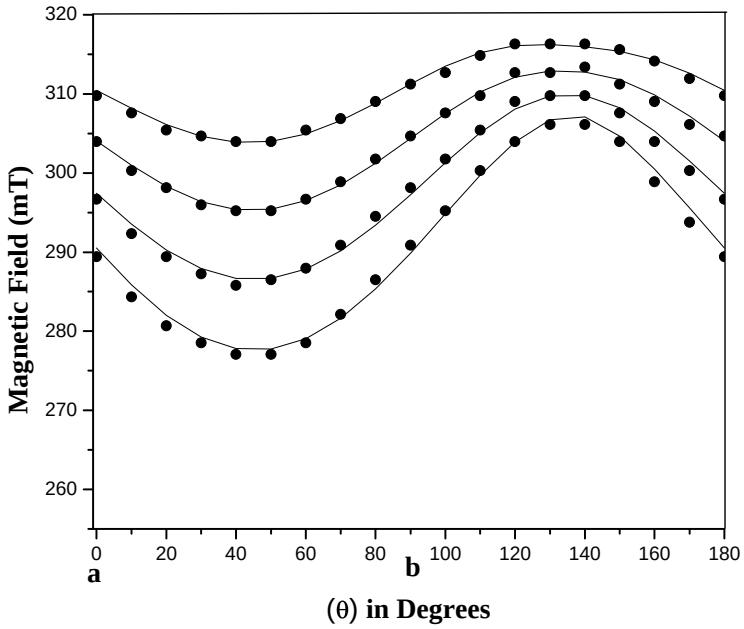

Fig. 7.4 Angular variation plot of Cu(II) doped AMMZ in the *ab*-plane. Frequency = 9.08527 GHz

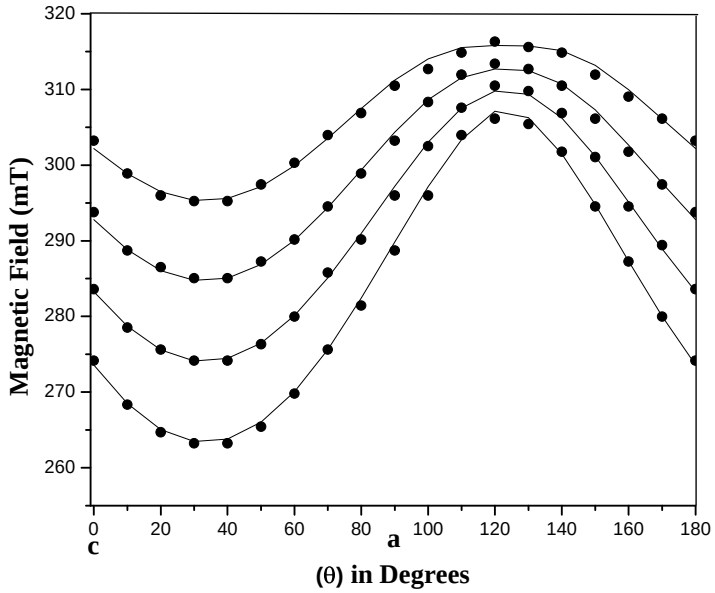

Fig. 7.5 Angular variation plot of Cu(II) doped AMMZ in the *ac*-plane. Frequency =9.08425 GHz

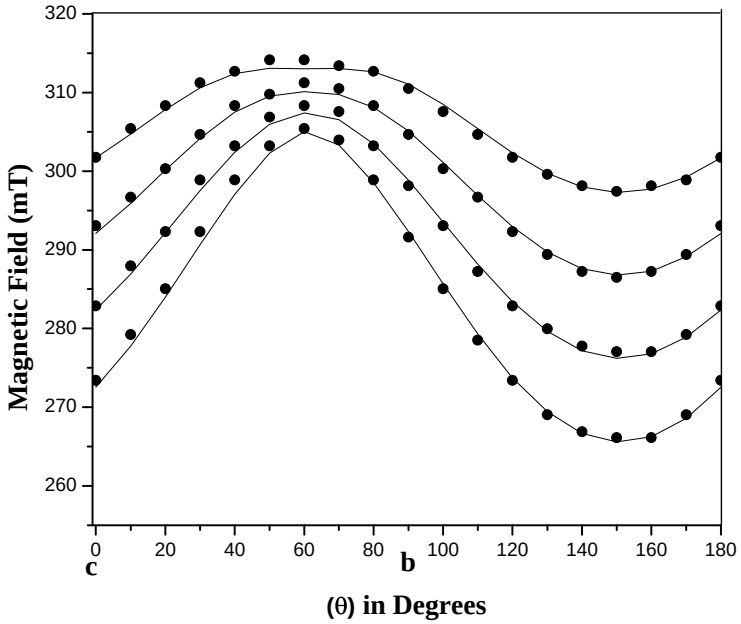

Fig. 7.6 Angular variation plot of Cu(II) doped AMMZ in the *bc*-plane. Frequency =9.08200 GHz

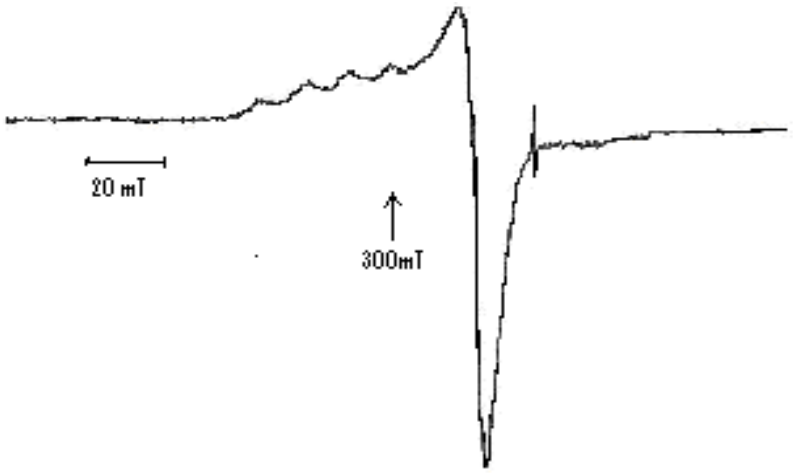

Fig. 7.7 Powder EPR spectrum of Cu(II)/AMMZ at RT. Top figure corresponds to experimental one, whereas bottom one is the simulated using parameters given in the text. Frequency = 9.38642 GHz.

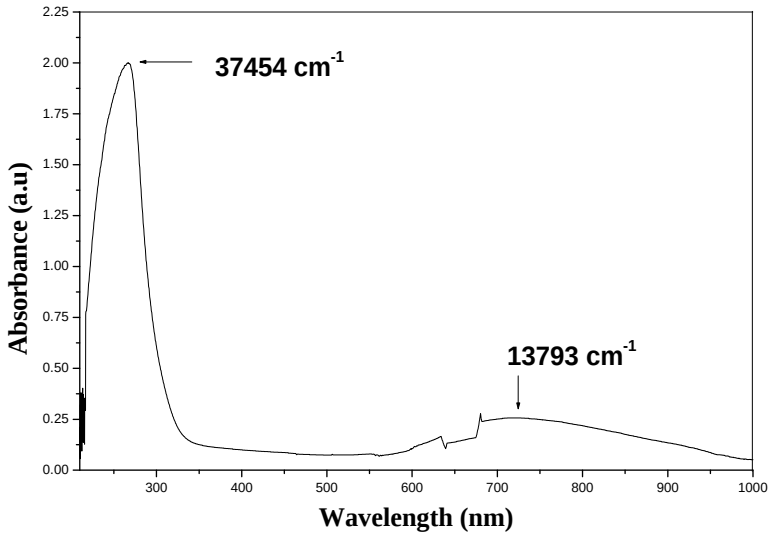

Fig. 7.8 Optical absorption spectrum of Cu(II) doped AMMZ at room temperature.

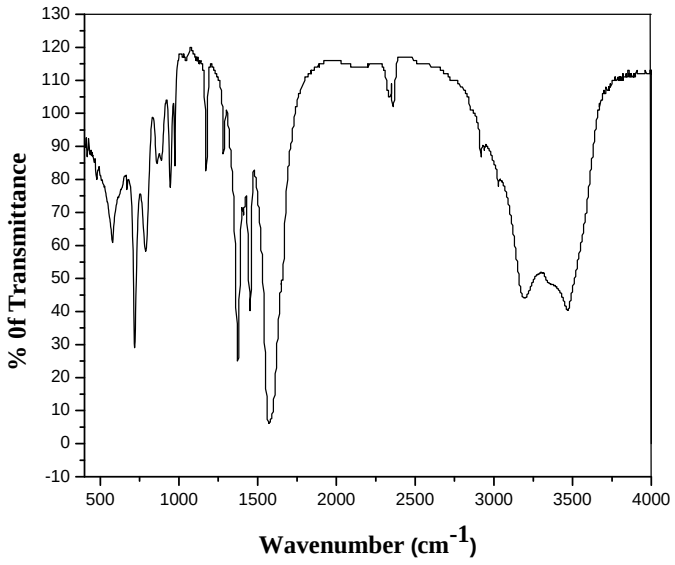

Fig. 7.9 FT-IR Spectra of Cu(II) doped AMMZ at room temperature.

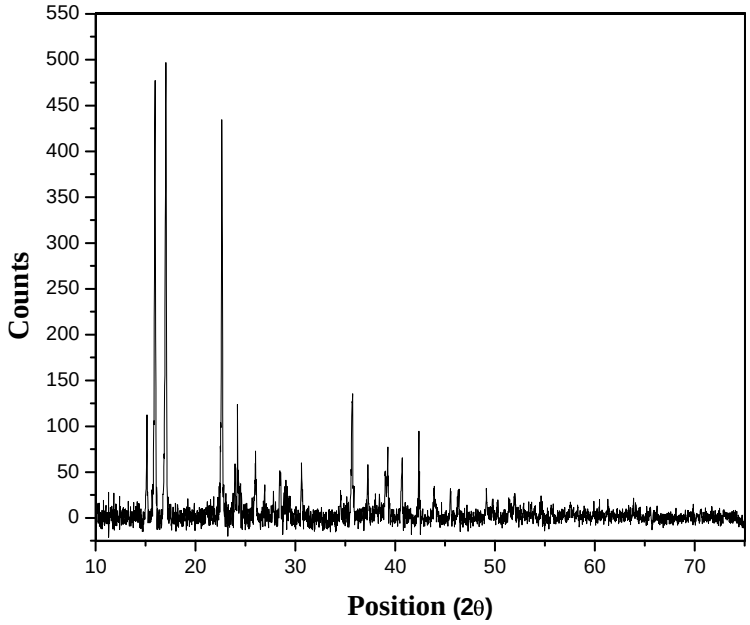

Fig. 7.10 Powder XRD pattern of Cu(II) doped AMMZ.

Table 7.1 Principal values and direction cosines of g and A matrices for Cu(II) doped AMMZ obtained at room temperature.

				Direction cosines		
			Principal values	a	b	c
g matrix						
2.153	-0.072	0.109	2.075	0.5022	-0.4564	0.7345
	2.154	-0.089	2.100	0.1637	-0.7838	-0.5990
		2.248	2.379	0.8491	0.4210	-0.3189
A matrix (mT)						
4.62	-0.82	5.24	2.69	0.4868	-0.4522	0.7473
	2.73	-5.94	3.04	0.3923	-0.6511	-0.6496
		6.43	13.45	-0.7804	-0.6095	0.1396

Table 7.2 Direction cosines of Zn – O in the crystal lattice of AMMZ. The numbers in parenthesis indicates ligands in which oxygen make a bond with Zn(II).

Zn – O bonds in	Direction cosines		
AMMZ	a	b	c
Zn – O (1)	-0.4026	0.5841	0.7048
Zn – O (1a)	-0.4026	0.5841	-0.7048
Zn – O (2)	0.5259	0.6770	0.5147
Zn – O (2a)	0.5259	0.6770	-0.5147
Zn – O (1w)	-0.7586	-0.6516	0.0000

Table 7.3 Spin-Hamiltonian parameters for Cu(II) in different host lattices. (*A* is in mT)

Host lattices	g_{zz}	g_{yy}	g_{xx}	A_{zz}	A_{yy}	A_{xx}	Ref.
Zn $(hfa)_2(Py)_2$	2.344	2.072	2.089	15.10	3.50	4.50	[26]
$[Co(tbz)_2(NO_3)(H_2O)]NO_3$	2.305	2.063	2.135	14.70	2.31	3.35	[33]
$Cd(PyDO)^a{}_6(BF_4)_2$	2.345	2.070	2.068	14.98	3.77	5.07	[34]
DAMZ[b]	2.443	2.087	2.077	14.74	2.88	1.83	[35]
CoAPH[c]	2.404	2.155	2.063	11.58	3.49	2.07	[36]
GLS[d]	2.311	2.057	2.084	15.95	3.26	8.96	[37]
AMMZ	2.379	2.100	2.075	13.45	3.04	2.69	Pesent
Powder	2.383	2.095	2.095	11.43	3.16	3.16	work

[a] 2-Pyridone;

[b] diaquamalonatozinc;

[c] cobalt ammonium phosphate hexahydrate;

[d] glycinelithium sulphate.

Table 7.4 Admixture coefficients of Cu(II) in various crystal lattices.

Lattices	a	b	c	d	e	Ref.
Cu/ZPPH[e]	0.330	0.941	0.051	0.032	-0.032	[13]
Cu/CoAPH	0.250	0.966	0.052	0.021	-0.021	[36]
Cu/CSSH[f]	0.281	0.957	0.057	0.032	-0.032	[40]
Cu/AMMZ	0.291	0.951	0.054	0.031	-0.031	Present Work

[e] zinc potassium phosphate hexahydrate;

[f] cadmium sodium sulphate hexahydrate.

Table 7.5 Molecular orbital coefficients for some Cu(II) systems.

Systems	κ	$P \times 10^{-4}(cm^{-1})$	α^2	Ref.
Cu(II)/Zn $(hfa)_2(Py)_2$	0.366	268.3	0.889	[26]
Cu(II)/ZnF_2	0.260	493.2	0.722	[29]
Cu(II)/DAMZ	0.284	240.8	0.790	[35]
Cu(II)/SCB[g]	0.380	360	0.850	[38]
Cu(II)/ZSSH[h]	0.295	245.4	0.709	[39]
Cu(II)/AMMZ	0.352	303	0.778	Present work

[g] Sorcosine cadmium bromide;

[h] zinc sodium sulphate hexahydrate.

Table 7.6 Observed FT-IR bands and their tentative assignments for Cu(II) doped AMMZ.

Assignment	FT-IR band(s) (cm^{-1})
Zn – O	579
Zn – O + O – C = O	789
– OH	3469
...OH_2	3191
Zn – OH_2	719, 789, 949
– CH_2 –	2358
– C = O	1174, 1373, 1450, 1569

Table 7.7 The calculated lattice parameters of Cu(II) doped AMMZ from powder XRD, along with single crystal XRD of AMMC [2].

Lattice parameters (nm) of AMMC from single crystal	Lattice parameters (nm) of Cu(II) doped AMMZ calculated from powder XRD
a = 0.6203	a = 0.6583
b = 0.6796	b = 0.7500
c = 0.6998	c = 0.6206

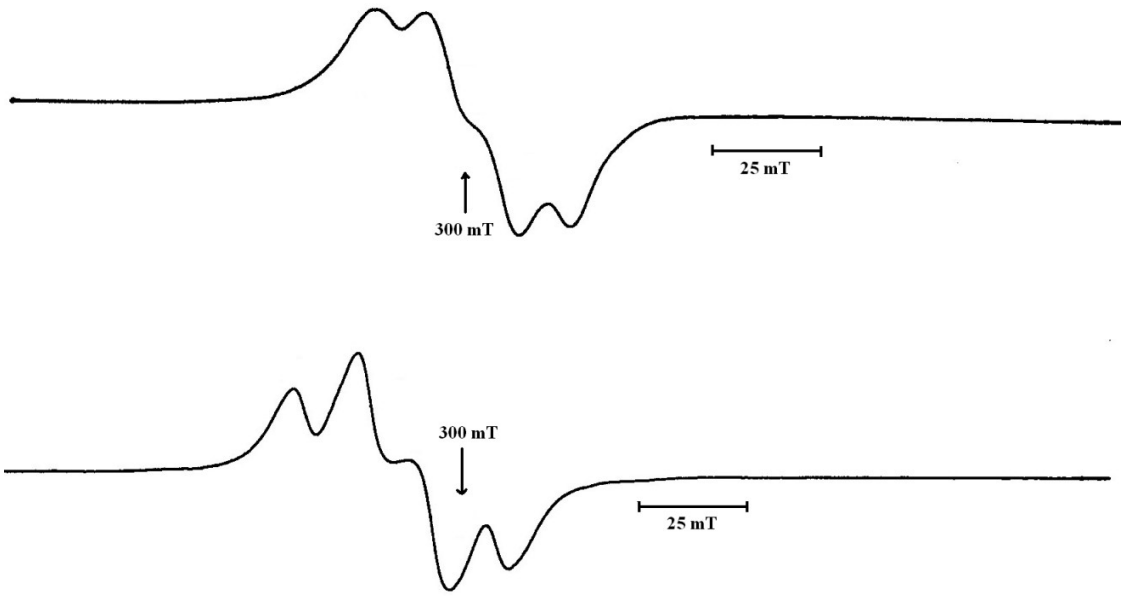

Fig. 8.1 Single crystal EPR spectra of Cu(II) doped HZBMZ at two orientations in *a***c** plane recorded at 300 K. Frequency =9.06084 GHz.

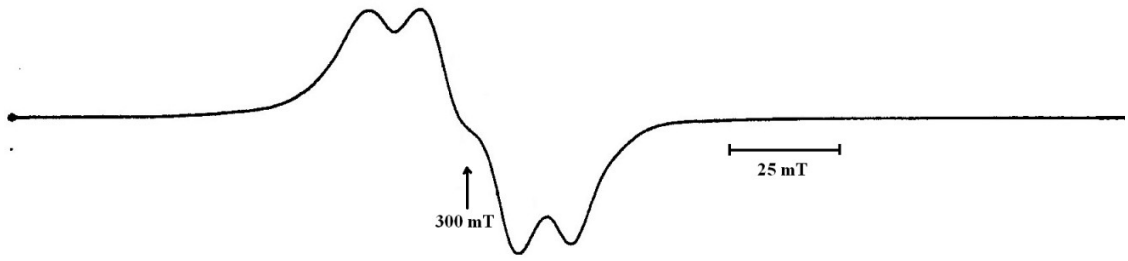

Fig. 8.2 Single crystal EPR spectrum of Cu(II) doped HZBMZ recorded at 300 K when the magnetic field (B) is parallel to axis *c**. Frequency =9.06057 GHz.

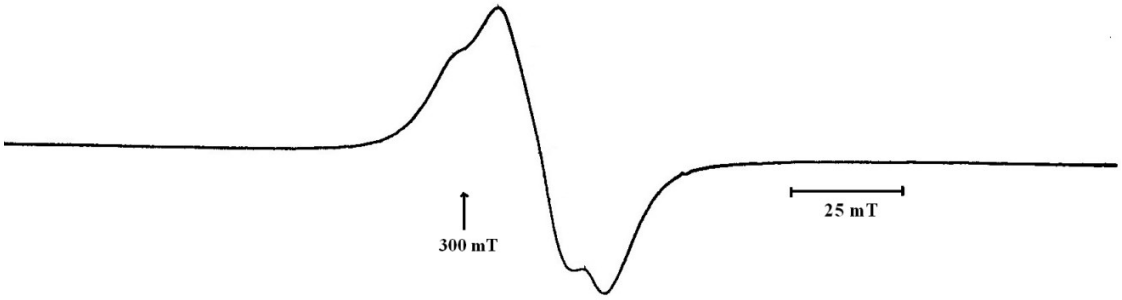

Fig. 8.3 Single crystal EPR spectrum of Cu(II) doped HZBMZ recorded at 300 K when B is parallel to axis *a**. Frequency =9.05661 GHz.

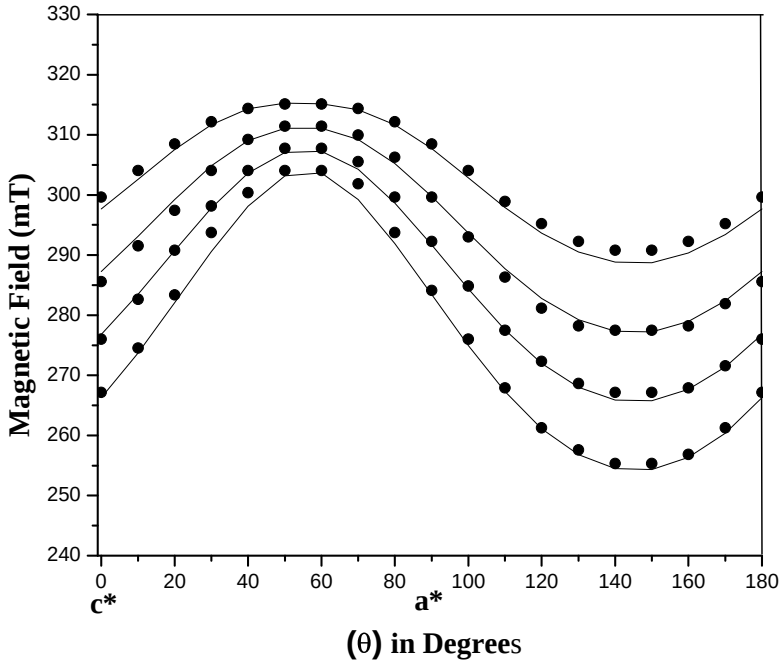

Fig. 8.4 Angular variation plot of Cu(II) doped HZBMZ in the *a***c** plane. Solid lines correspond to theoretical variation and the solid circles correspond to the experimental data. Frequency = 9.06084 GHz.

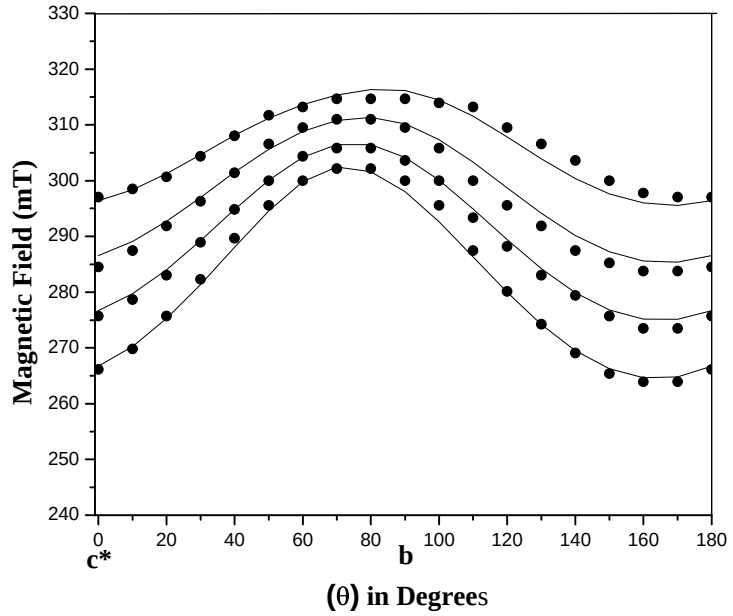

Fig. 8.5 Angular variation plot of Cu(II) doped HZBMZ in the *bc** plane. Frequency = 9.06057 GHz.

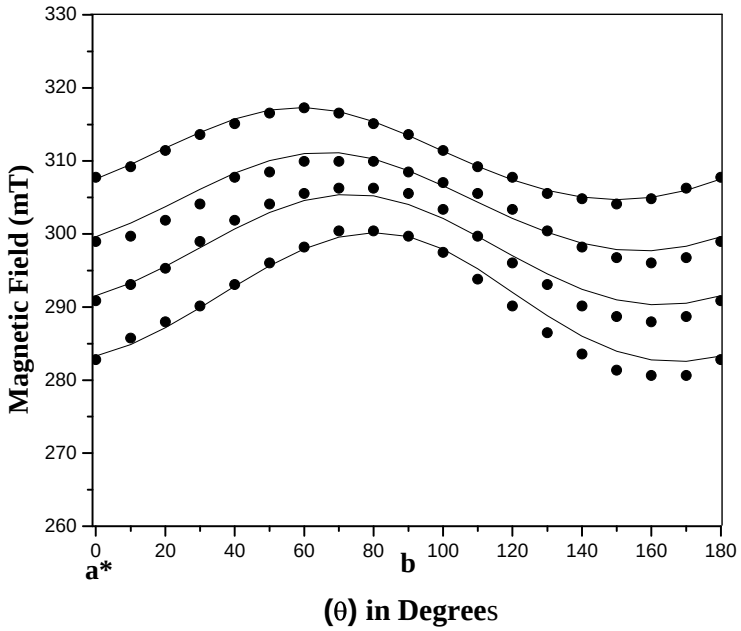

Fig. 8.6 Angular variation plot of Cu(II)-doped HZBMZ in the *a*b* plane. Frequency = 9.05661 GHz.

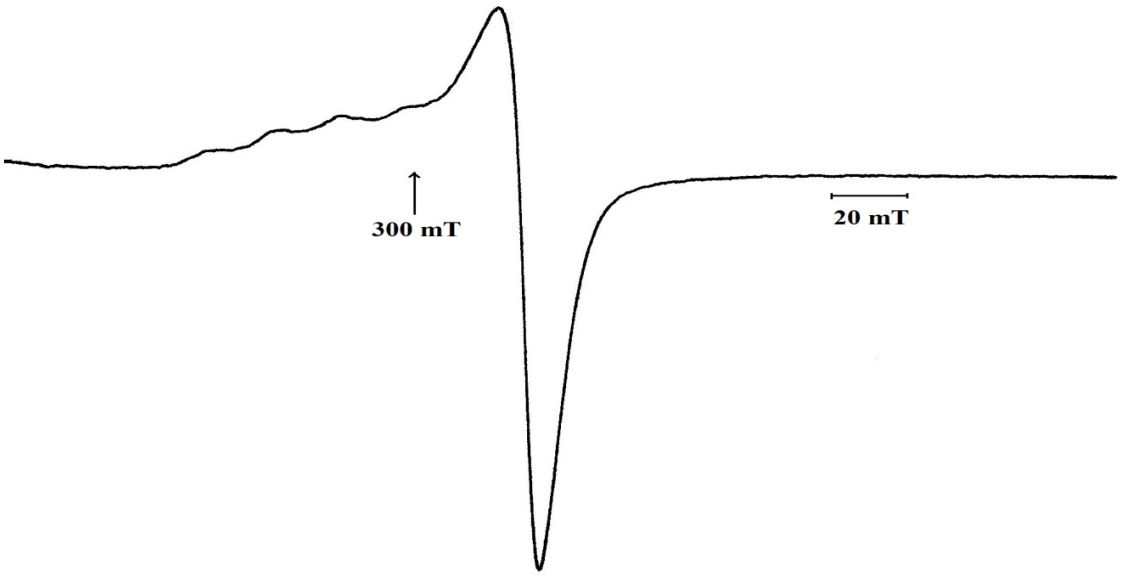

Fig. 8.7 Powder EPR spectrum of Cu(II)/HZBMZ at RT. Top figure corresponds to experimental one, whereas bottom one is the simulated using parameters given in the text. Frequency = 9.35235 GHz.

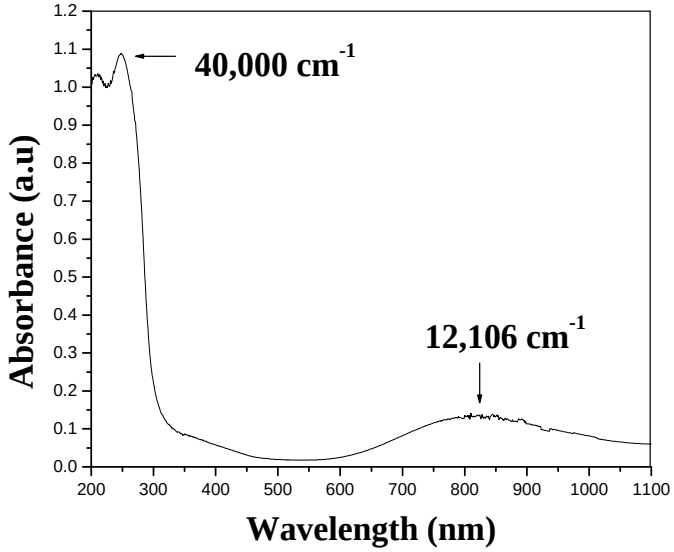

Fig. 8.8 Optical absorption spectrum of powder sample of Cu(II)/HZBMZ recorded at room temperature.

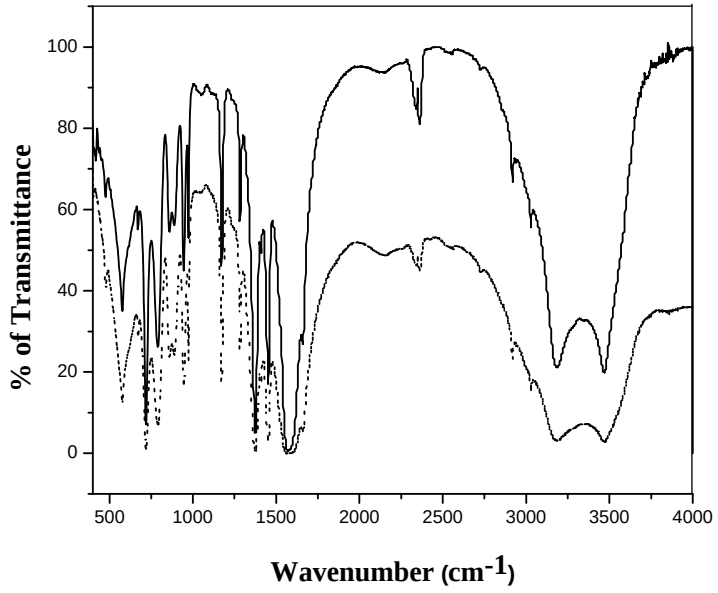

Fig. 8.9 FT – IR spectra of pure (dotted line) and Cu(II) ion doped HZBMZ (solid line) at room temperature.

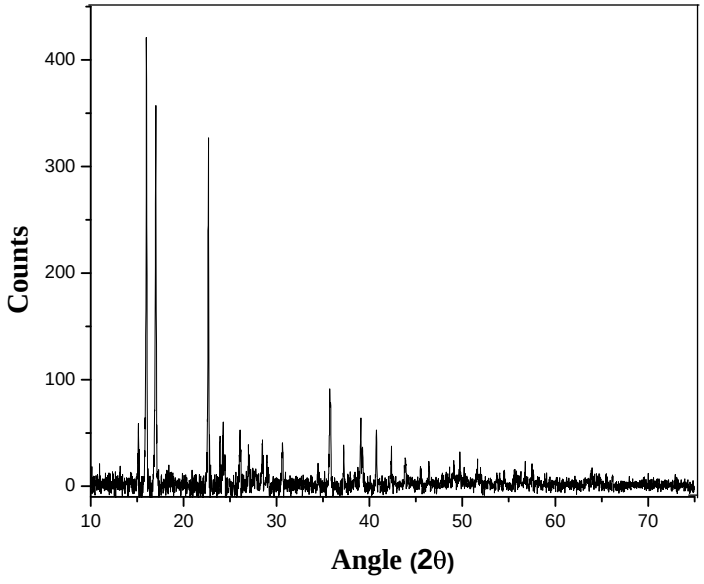

Fig. 8.10 Powder XRD pattern of Cu(II) doped HZBMZ.

Table 8.1 Principal values and direction cosines of g and A matrices for Cu(II) doped HZBMZ obtained at room temperature.

				Direction cosines		
			Principal values	a*	b	c*
g matrix						
2.183	-0.034	-0.139	2.034	-0.5455	-0.1068	0.8313
	2.108	-0.059	2.159	0.5939	-0.7491	0.2935
		2.289	2.388	0.5913	0.6538	0.4721
A matrix (mT)						
6.85	0.83	-4.56	3.39	-0.5501	-0.1069	0.8282
	4.61	-1.18	4.89	-0.4736	0.8568	- 0.2039
		10.54	13.72	-0.6878	-0.5044	-0.5219

Table 8.2 The direction cosines of Zn-O bonds for HZBMZ, obtained from the crystallographic data.

Zn – O bonds in HZBMZ	Direction cosines		
	a*	b	c*
Zn – O (1w)	0.7389	-0.1537	-0.6559
Zn – O (2w)	-0.3862	0.6280	-0.6756
Zn – O (3w)	0.5328	0.7394	0.4117
Zn – O (1)	0.6448	-0.7395	-0.1934
Zn – O (3)	-0.4591	-0.1025	-0.8825
Zn – O (4w)	0.0000	0.8275	-0.5614

Table 8.3 Spin-Hamiltonian parameters for Cu (II) in different host lattices. (*A* is in mT).

Host lattices	g_{zz}	g_{yy}	g_{xx}	A_{zz}	A_{yy}	A_{xx}	Ref.
Zn $(hfa)_2(Py)_2$	2.344	2.072	2.089	15.10	3.50	4.50	[23]
$[Co(tbz)_2(NO_3)(H_2O)]NO_3$	2.305	2.063	2.135	14.70	2.31	3.35	[18]
$(PyDO)_6(BF_4)_2$	2.345	2.070	2.068	14.98	3.77	5.07	[19]
DAMZ[a]	2.443	2.087	2.077	14.74	2.88	1.83	[20]
DADT[b]							
Site I	2.337	2.060	2.093	13.0	1.8	4.6	[1]
Site II	2.330	2.043	2.092	13.1	2.0	3.6	
HZBMZ	2.388	2.159	2.034	13.72	4.89	3.39	Present
Powder	2.383	2.095	2.095	11.43	3.16	3.16	work

[a] diaquamalonatozinc.

[b] Diammonium D-tartrate.

Table 8.4 Admixture coefficients of Cu(II) in various crystal lattices.

Lattices	a	b	c	d	e	Ref.
Cu/ZPPH[c]	0.330	0.941	0.051	0.032	-0.032	[6]
Cu/CSSH[d]	0.281	0.957	0.057	0.032	-0.032	[26]
Cu/ZAPN[e]	0.142	0.988	0.050	0.022	-0.017	[27]
Cu/SCB[f]	0.128	0.989	0.057	0.016	0.033	[25]
Cu/HZBMZ	0.291	0.951	0.054	0.031	-0.031	Present Work

[c] zinc potassium phosphate hexahydrate.

[d] cadmium sodium sulphate hexahydrate.

[e] $Zn(AP)_2(NO_3)_2$.

[f] sarcosine cadmium bromide.

Table 8.5 Molecular orbital coefficients for some Cu(II) systems.

Systems	κ	$P \times 10^{-4}(cm^{-1})$	α^2	Ref.
Cu (II)/Zn (hfa) $_2(Py)_2$	0.366	268.3	0.889	[23]
Cu (II)/ZnF_2	0.260	493.2	0.722	[28]
Cu (II)/DAMZ	0.284	240.8	0.790	[20]
Cu (II)/SCB	0.380	360.0	0.850	[29]
Cu (II)/ZSSH[g]	0.295	245.4	0.709	[30]
Cu (II)/HZBMZ	0.360	320.0	0.809	Present work

[g] zinc sodium sulphate hexahydrate

Table 8.6 Observed FT-IR bands and their tentative assignments for Cu(II) doped in HZBMZ.

Assignment	FT-IR band(s) (cm^{-1})
Zn – O	579
Zn – O + O – C = O	789
– OH	3469
...OH_2	3191
Zn – OH_2	719, 789, 949
– CH_2 –	2358
– C = O	1174, 1373, 1450, 1569

Table 8.7 The calculated lattice parameters of HZBMZ and Cu(II) doped HZBMZ from powder XRD, along with single crystal XRD of HZBMC [14].

Lattice parameters (nm) of HZBMC From single crystal XRD	Lattice parameters (nm) calculated from powder XRD	
	HZBMZ	Cu doped HZBMZ
a = 0.5274	a = 0.5382	a = 0.5382
b = 0.7504	b = 0.7424	b = 0.7424
c = 1.0314	c = 1.1293	c = 1.1293

SUMMARY

Single crystal EPR studies of some first row transition metal ions doped in a few dia and paramagnetic host lattices have been reported in the present thesis. In addition to single crystal EPR studies, optical, FT-IR and XRD studies are also carried out. The main aim of the thesis is to predict the location of the paramagnetic impurity, when incorporated in octahedral symmetry, having same type of ligand but different metal ions. For this, four lattices have been selected, out of which one of them is a paramagnetic host. A comparison of other metal complexes with those of zinc complexes suggests that the reduced size of the Zn(II) coordination sphere plays a vital role in deciding the formation of the complexes. Hence, four host lattices Hexaaquazincdiaquabis(malonato)zincate (HZBMZ), Aquomethylmelonatozinc(II) (AMMZ), Alkaline salt of the bis(malonate) metal(II) anions $\{[A(H_2O)_n]_2\ [M(mal)_2(H_2O)_m]\}$, A = Li, K and M = Zn {aqualithiumaquabismalonatozincate (ALMZ), triaquadipotassiumbis(malonato)zincate (PBMZ)} and Ni {triaquapotassiumbis(malonato)nickelate (PBMN)} respectively, are preferred.

A total of three paramagnetic impurities viz., VO(II), Mn(II) and Cu(II) are selected for this study. The VO(II) ion is doped in both diamagnetic and paramagnetic host lattices ALMZ and PBMN respectively. The Mn(II) ion doped in diamagnetic host lattices PBMZ and HZBMZ. The Cu(II) ion doped in the following diamagnetic host lattices AMMZ and HZBMZ.

Single crystal EPR investigation of VO(II) ion in both ALMZ and PBMN lattices shows only one type of impurity in the crystal and also indicates that the impurity has entered the lattice in an interstitial position in both lattices, due to the ligand environment. In PBMN host lattice, the central metal ion Ni(II) is also paramagnetic ion. Surprisingly, Ni(II) behaves as a diamagnetic ion at room temperature and its paramagnetic nature is identified at low temperature measurements. The spin – lattice relaxation times are calculated from the line width measurements. Admixture coefficients, bonding and optical parameters have also been calculated.

Single crystal EPR study of Mn(II) ion doped in PBMZ and HZBMZ host lattices are performed at room temperature. Mn(II) ion in PBMZ shows more than 30 lines pattern EPR spectra indicating the presence of two sites, one with large D value and the other with smaller D value. Both the Mn(II) sites entered the lattice interstitially. Covalency of the bonding and optical parameters have also been calculated. Mn(II) ion in HZBMZ shows two types of impurity ions in the host lattice, with intensity ratio of 6:1. However, the latter could not be followed due to its low intensity during crystal rotations. The Mn(II) ion entered the lattice substitutionally. The evaluated spin Hamiltonian parameters reveal an elongated octahedral symmetry. The relatively large D and E values suggest the distortion in both the lattices due to steric effect of the malonic acid in both lattices.

Single crystal EPR analysis of Cu(II) ion doped in AMMZ and HZBMZ diamagnetic host lattices indicates that the number of impurity sites in the crystal is found to be independent of concentration of the dopant and shows only one type of impurity in the crystal. The Cu(II) ion incorporated interstitially in AMMZ and substitutionally in HZBMZ host lattices. The low value of A_{zz} has been explained by considering admixture of $d_{x^2-y^2}$ ground state with d_{z^2} excited state.

Optical absorption studies of VO(II), Mn(II) and Cu(II) ions in various corresponding host lattices confirm the lattice distortion in the crystal. The crystal field parameters are calculated by relating the optical data with EPR data. The tentative assignment of FT-IR bands for VO(II), Mn(II) and Cu(II) ions doped in respective host lattices and undoped host lattices shows identical band positions, confirming no structural changes after doping due to low concentration of the dopant. Powder XRD patterns of VO(II), Mn(II) and Cu(II) doped and respective host lattices give the identical lattice parameters which confirm that the low concentration of dopant ions does not change the structure of the host lattice.

Additional work is also promising with these dia and paramagnetic hosts, with the incorporation of paramagnetic ions like Fe(III), Cr(III), Gd(III) etc., and the work is in progress.

Research Papers in refereed Journals:

1. **S. Boobalan** and P. Sambasiva Rao, Identification of Structure and Position of Cu(II) ion in aquomethylmelonatozinc(II) host by EPR Spectroscopy, Appl. Magn. Reson. 38 (2010) 25.

2. **S. Boobalan** and P. Sambasiva Rao, Structural Elucidation of Transition Metal Complex by Single Crystal EPR Study, Journal of Organometallic Chemistry, 695 (2010) 963.

3. **S. Boobalan** and P. Sambasiva Rao, Effect of paramagnetic doping on an inorganic polymer Triaquadipotassiumbis(malonato)zincate: Spectroscopic investigation – Submitted.

4. **S. Boobalan** and P. Sambasiva Rao, Structural Elucidation of Cu(II) ion doped in Hexaaquozincdiaquobis(malonato)zincate host by EPR Spectroscopy – Submitted.

5. **S. Boobalan** and P. Sambasiva Rao, Spectroscopic investigations of an inorganic polymeric material Aqualithiumaquabismalonatozincate doped with VO(II) – Submitted.

6. **S. Boobalan** and P. Sambasiva Rao, Spin – Lattice Relaxation Measurements and Structural Investigation of VO(II) ion doped in a Paramagnetic host by EPR Study – Submitted.

National Conferences:

1. **S. Boobalan**, B. Natarajan, S. Mithira and P. Sambasiva Rao, EPR, IR, UV-Visible spectral and XRD studies on Trisquapotassiumbis(malonato)zincate doped with Mn(II), "Recent Advances in Metalloorganic Chemistry (RAMC-2008)", Salem, October 16-17, 2008. Page No: 13.

2. **S. Boobalan** and P. Sambasiva Rao, EPR, FT-IR, UV-VIS spectroscopy and powder XRD investigation of VO(II) ion doped Aqualithiumaquabismalonatozincate single crystal, "Advances in Physical and Theoretical Chemistry (APTChem-2009)", Calicut, March, 19-20, 2009. Page No. 85.

3. **S. Boobalan** and P. Sambasiva Rao, Structural Elucidation of Cu(II) ion doped in Hexaaquazincdiaquabismalonatozincate host by EPR Specroscopy, "National Conference on Recent Advances in Chemistry (NCRAC-2009)", Tiruchi, September, 18, 2009. Page No. 2.

4. M. Rajeswari, **S. Boobalan**, K.Parthiban and P. Sambasiva Rao, Single Crystal EPR and Optical studies of VO(II) doped in Tetraaqua(1,10-phenanthroline-κ^2-N,N')magnesium(II)dinitrate "National Seminar on Modern Trends in Chemistry (MTC-2009)", Madurai, September, 24-25, 2009. Page No. 29.

5. P. Saranya, **S. Boobalan,** K. Parthiban and P. Sambasiva Rao, Single Crystal EPR and Optical Studies of VO(II) doped in Aqua(malonato)cadmium(II)hydrate, Proceedings of the National Conference on Recent Advances in Materials and Methods of Chemistry (RAMMC 2010), February, 2nd, 2010. Page No: 81-90. ISBN: 978-81-907519-2-6.

6. Participated in the national level conference on the resent trends in the field of Nanoscience and Technology, NANOMEET-2010, held at Anna University Chennai on the 25^{th}-26^{th} March, 2010.

International Conférence/Symposium:

1. **S. Boobalan,** B. Natarajan, S. Mithira and P. Sambasiva Rao, Identification of Interstitial Substitution of Two Mn(II) Sites in Triaquapotassiumbis(malonato) Zincate by Single Crystal EPR Study, 6^{th} Asia Pacific EPR/ESR Symposium (APES 2008), Cairns, Australia, July, 13-18, 2008. Page No: 71. ISBN: 978-0-9805389-0-8.

2. **S. Boobalan** and P. Sambasiva Rao, Structural Elucidation of Transition Metal Complex by Single Crystal EPR Study, "12th International symposium on Inorganic Ring system (IRIS – 12)", Goa, August 16 – 21, 2009. P_{10}, Page No: 90.

3. **S. Boobalan** and P. Sambasiva Rao, Spin-Lattice Relaxation measurements and structural investigation of VO(II) ion doped in a paramagnetic host by EPR study, "Symposium on Modern Trends in Inorganic Chemistry, MTIC-XIII", Bangalore, December 07 – 10, 2009. P67, Page No: 181.

4. K. Parthiban, S. Mithira, **S. Boobalan** and P. Sambasiva Rao, Single crystal EPR and Optical studies of vanadyl impurity doped in Tetraaqua(1,10–phenanthroline)zinc(II)sulphatedihydrate, "International conference on coordination & organometallic chemistry (ICCOC – 2009)", Coimbatore, March 19^{th} & 20^{th} , 2009.

5. Participated in International Conference on Green Energy Technologies, GET-2010, held at Pondicherry University, Pondicherry on the March 23-25, 2010.

National level Workshop:

1. Participated in the National level workshop on "Theory and Practice of X-ray diffraction techniques (TPXRDT - 2009)", held on July, 13-17, 2009 at Department of Physics, Alagappa University, Karaikudi.

2. Participated in the National level workshop on "Recent Trends in Crystal Growth", held on March, 30^{th}, 2010 at Crystal Growth Centre, Anna University, Chennai.